K-mouflage effects on clusters of galaxies

Philippe Brax, Luca Alberto Rizzo, and Patrick Valageas
Institut de Physique Théorique,
Université Paris-Saclay CEA, CNRS,
F-91191 Gif-sur-Yvette, Cédex, France

(Dated: March 4, 2022)

We investigate the effects of a K-mouflage modification of gravity on the dynamics of clusters of galaxies. We extend the description of K-mouflage to situations where the scalar field responsible for the modification of gravity is coupled to a perfect fluid with pressure. We describe the coupled system at both the background cosmology and cosmological perturbations levels, focusing on cases where the pressure emanates from small-scale nonlinear physics. We derive these properties in both the Einstein and Jordan frames, as these two frames already differ by a few percents at the background level for K-mouflage scenarios, and next compute cluster properties in the Jordan frame that is better suited to these observations. Galaxy clusters are not screened by the K-mouflage mechanism and therefore feel the modification of gravity in a maximal way. This implies that the halo mass function deviates from Λ-CDM by a factor of order one for masses $M \gtrsim 10^{14}\ h^{-1}M_\odot$. We then consider the hydrostatic equilibrium of gases embedded in galaxy clusters and the consequences of K-mouflage on the X-ray cluster luminosity, the gas temperature, and the Sunyaev-Zel'dovich effect. We find that the cluster temperature function, and more generally number counts, are largely affected by K-mouflage, mainly due to the increased cluster abundance in these models. Other scaling relations such as the mass-temperature and the temperature-luminosity relations are only modified at the percent level due to the constraints on K-mouflage from local Solar System tests.

PACS numbers: 98.80.-k

I. INTRODUCTION

K-mouflage [1, 2] is one of the four types of screening mechanisms, together with the chameleon [3, 4], the Damour-Polyakov [5] and the Vainshtein [6] ones, which are compatible with second-order equations of motion for single scalar field models [7]. The properties of K-mouflage have already been thoroughly studied both at the background cosmology [7] and perturbation levels [8, 9], see also [10] for a more general analysis within an "imperfect-fluid" formalism. The small-scale dynamics have been studied in [11], and models that satisfy both cosmological and Solar System constraints have been devised in [12].

In this paper, we extend these studies by including fluids with pressure as befitting the description of gases in galaxy clusters. We do so for both the background and perturbations. We also present the dynamics of the system in both the Einstein frame (used in previous works) and the Jordan frame, and discuss the relations between both frames. Because the properties of gases, such as the X-ray luminosity or the Sunyaev-Zel'dovich effect [13], or the wavelength of atomic emission or absorption lines, are tied to the frame in which atomic physics is described without any modification due to the scalar field, we work in the Jordan frame to describe clusters of galaxies. We use the fact that galaxy clusters are not screened by the K-mouflage mechanism and that their number would be increased as compared with Λ-CDM in this scenario. As a result, clusters appear as a useful testing ground for K-mouflage and its effects on the growth of structure.

We take into account the modification of the hydrostatic equilibrium in K-mouflage models, together with the change of the matter density profiles, which we find to become slightly more compact. This allows us to investigate the X-ray luminosity as a function of the gas temperature. The deviation from Λ-CDM is at the percent level and is set by the tests of gravity in the Solar System, which strongly constrain the coupling constant that defines these models. In a similar fashion, the temperature-mass relation is affected at the same level. As particular examples, we focus on a simple "cubic" K-mouflage model (that agrees with cosmological constraints) and on an "arctan" model which satisfies cosmological constraints as well as all Solar System tests, including the advance of the perihelion of the Moon [12]. The latter gives slightly amplified results as compared to the former, but both remain at the percent level. The only observable which deviates significantly from Λ-CDM is the cluster temperature function (or more generally, number counts) due to the increased abundance of clusters for masses $M \gtrsim 10^{14}\ h^{-1}M_\odot$.

The paper is arranged as follows. In section II, we define the K-mouflage models and detail some of their properties for a fluid with pressure coupled to K-mouflage at the background and perturbation levels, working in the Einstein frame. In section III, we reformulate the dynamics in terms of the Jordan-frame quantities. In section IV, we present our numerical results for the background and the growth of structure for two K-mouflage models: the cubic and arctan models. In section V, we turn to galaxy clusters and their properties focusing on the physics of the gas embedded in the clusters. In section VI, we discuss in details the similarity and differences between the

K-mouflage scenarios and other modified-gravity theories. We conclude in section VII.

A derivation of the equations of motion in the Einstein frame is given in appendix A, while details on the Einstein-Jordan connection can be found in the appendix B. We discuss unitarity constraints in appendix C.

II. DEFINITION OF K-MOUFLAGE MODELS

A. Jordan-frame and Einstein-frame metrics

We consider scalar-field models where the action has the form [1, 2]

$$S = \int \mathrm{d}^4x\,\sqrt{-\tilde{g}}\left[\frac{\tilde{M}_{\rm Pl}^2}{2}\tilde{R}+\tilde{\mathcal{L}}_\varphi(\varphi)\right] + \int \mathrm{d}^4x\,\sqrt{-g}\,\mathcal{L}_{\rm m}(\psi_{\rm m}^{(i)},g_{\mu\nu}), \quad (1)$$

which involves two metrics, the Jordan-frame metric $g_{\mu\nu}$, with determinant g, and the Einstein-frame metric $\tilde{g}_{\mu\nu}$, with determinant $\tilde{g}$. The matter Lagrangian density, $\mathcal{L}_{\rm m}$, where $\psi_{\rm m}^{(i)}$ are various matter fields, is given in the Jordan frame, where it takes the usual form without explicit coupling to the scalar field (although one could add explicit couplings to build more complex models). The gravitational sector is described by the usual Einstein-Hilbert action, but in terms of the Einstein-frame metric $\tilde{g}_{\mu\nu}$ and the associated reduced Planck mass $\tilde{M}_{\rm Pl}=1/\sqrt{8\pi\tilde{\mathcal{G}}}$. The Lagrangian density $\tilde{\mathcal{L}}_\varphi(\varphi)$ of the scalar field is also given in the Einstein frame.

Throughout this paper, we denote Einstein-frame quantities with a tilde, to distinguish them from their Jordan-frame counterparts (when they are not identical). We choose this notation, which is the opposite to the one used in our previous papers [7, 8, 11, 12] where we mostly worked in the Einstein frame, as here we mostly work in the Jordan frame.

If the two metrics were identical, this model would be a simple quintessence scenario [14, 15], with an additional scalar field to the usual matter and radiation components but with standard electrodynamics and gravity (General Relativity). In this paper, we consider modified-gravity models where the two metrics are related by the conformal transformation [16]

$$g_{\mu\nu}=A^2(\varphi)\,\tilde{g}_{\mu\nu}. \quad (2)$$

This gives rise to an explicit coupling between matter and the scalar field. In the Einstein frame we recover General Relativity (e.g., the Friedmann equations) but the equations of motion of matter are non-standard (e.g., the continuity equation shows a source term and matter density is not conserved). In the Jordan frame the equations of motion of matter take the usual form (e.g., matter density is conserved) but gravity is modified (e.g., the Friedmann equations are modified). In this paper we compute the properties of astrophysical objects such as clusters of galaxies, including their temperature and X-ray luminosity, and it is more convenient to work in the Jordan frame. Then, radiative processes, such as Bremsstrahlung, are given by the standard results and do not vary with time or space. Moreover, matter density is conserved. This simplifies the analysis, as the only difference from a Λ-CDM scenario will be a change of gravity laws, which can be explicitly derived from the action (1).

The conformal transformation (2) actually means that the line elements are transformed as $\mathrm{d}s^2=A^2\mathrm{d}\tilde{s}^2$. Using conformal time τ and comoving coordinates $\mathbf{x}$, this local change of distance can be absorbed in the scale factor for the background universe, as

$$\mathrm{d}s^2=a^2(-\mathrm{d}\tau^2+\mathrm{d}\mathbf{x}^2),\quad \mathrm{d}\tilde{s}^2=\tilde{a}^2(-\mathrm{d}\tau^2+\mathrm{d}\mathbf{x}^2), \quad (3)$$

with

$$a=\bar{A}\tilde{a},\quad \tau=\tilde{\tau},\quad \mathbf{x}=\tilde{\mathbf{x}}. \quad (4)$$

[Throughout this paper, we denote with an overbar mean background quantities, such as $\bar{A}=A(\bar{\varphi})$.] However, physical time t and distances $\mathbf{r}$, with $\mathrm{d}s^2=-\mathrm{d}t^2+\mathrm{d}\mathbf{r}^2$, are changed as

$$\mathrm{d}t=\bar{A}\,\mathrm{d}\tilde{t},\quad \mathbf{r}=a\mathbf{x}=\bar{A}\,\tilde{\mathbf{r}}. \quad (5)$$

In particular, the cosmic times t and $\tilde{t}$ are not the same in both frames

B. K-mouflage kinetic function

In this paper, we consider K-mouflage models [1, 2, 7], which correspond to cases where the scalar-field Lagrangian has a non-standard kinetic term,

$$\tilde{\mathcal{L}}_\varphi(\varphi)=\mathcal{M}^4\,K(\tilde{\chi})\quad\text{with}\quad \tilde{\chi}=-\frac{1}{2\mathcal{M}^4}\tilde{\nabla}^\mu\varphi\tilde{\nabla}_\mu\varphi. \quad (6)$$

Throughout this paper, $\tilde{\nabla}_\mu$ (∇_μ) is the covariant derivative associated with the metric $\tilde{g}_{\mu\nu}$ ($g_{\mu\nu}$) (hence $\chi=A^{-2}\tilde{\chi}$, but we work with $\tilde{\chi}$ in the following). Here, $\mathcal{M}^4$ is an energy scale that is of the order of the current dark-energy density, (i.e., set by the cosmological constant), to recover the late-time accelerated expansion of the Universe. Thus, the canonical cosmological behavior, with a cosmological constant $\tilde{\rho}_\Lambda=\mathcal{M}^4$, is recovered at late time in the weak-$\tilde{\chi}$ limit if we have

$$\tilde{\chi}\to 0:\quad K(\tilde{\chi})\simeq -1+\tilde{\chi}+..., \quad (7)$$

where the dots stand for higher-order terms, the zeroth-order factor -1 corresponding to the late-time cosmological constant $\mathcal{M}^4$. The normalization of the first two terms in Eq.(7) defines the normalizations of the constant $\mathcal{M}^4$ and of the field φ, hence it does not entail any loss of

generality (within this class of models). We only consider models that satisfy this low-$\tilde{\chi}$ expansion in this article, and where $\bar{\tilde{\chi}} \to \infty$ for $\tilde{t} \to 0$ and $\bar{\tilde{\chi}} \to 0$ for $\tilde{t} \to \infty$.

Well-behaved K-mouflage scenarios have $K' > 0$, where we denote $K' = \mathrm{d}K/\mathrm{d}\tilde{\chi}$, and $W_\pm(y) = yK'(\pm y^2/2)$ must be monotonically increasing functions up to $+\infty$ over $y \geq 0$. This ensures that the cosmological dynamics are well defined up to arbitrarily high redshift, where the matter density becomes increasingly large, and that small-scale static solutions exist for any matter density profile [11]. Moreover, there are no ghosts around the cosmological background nor small-scale instabilities [7].

We must point out that the kinetic functions $K(\tilde{\chi})$ that we use for numerical computations and illustrative purposes in this paper are defined by fully nonlinear expressions, namely Eqs.(71) and (74) below, and as such go beyond the low-$\tilde{\chi}$ expansion (7). As explained above, the latter expansion is very general and holds for well-behaved models, where $K' > 0$ for all $\tilde{\chi}$ and $W_\pm(y) = yK'(\pm y^2/2)$ are monotonically increasing functions of y. The expansion (7) would only be violated if K' diverges at low $\tilde{\chi}$, e.g. $K(\tilde{\chi}) = -1 + \tilde{\chi}^{3/4} + ...$, but we do not consider such singular cases here.

Then, it happens that at at low redshifts, in the dark-energy era, $\tilde{\chi}$ [with its normalization defined by the first two coefficients in the expansion (7)] is small on cosmological scales, which implies $K' \simeq 1$. This holds both for the homogeneous background and for the cosmological large-scale structures. This property is related to the fact that at low redshifts, in the dark-energy era, we require the cosmological evolution to remain close to the Λ-CDM behavior. From the expressions (17), we can see that this implies $\bar{\tilde{\chi}}\bar{K}' \ll \bar{K}$ (to recover a dark-energy equation of state $\bar{p}_{\rm de} \simeq -\bar{\rho}_{\rm de}$) whence $\bar{\tilde{\chi}} \ll 1$. In fact, at low z we have the scaling $\bar{\tilde{\chi}} \sim \beta^2$, where β is the coupling strength defined in Eq.(9) below, so that $\bar{\tilde{\chi}} \sim 0.01$ as we take $\beta = 0.1$. We shall check this behavior in Fig. 4 below.

We shall also check in Sec. V B and Fig. 13 below that this also applies to clusters of galaxies at low redshifts, which are not screened by the nonlinearities of the scalar-field Lagrangian, in spite of their large mass. This would not be the case for a coupling $\beta \gg 0.1$, but this would violate some Solar System and cosmological constraints and we do not consider such models here.

Nevertheless, the nonlinearities of the kinetic function $K(\tilde{\chi})$ come into play at high redshift and are taken into account in our computations, using the explicit nonlinear examples (71) and (74). This ensures in particular that the dark-energy density becomes subdominant at high z and that we recover the Einstein-de Sitter cosmology in the early matter era [7]. Moreover, the background solution can be shown to be stable and is a tracker solution [7]. The nonlinearities on the far negative semiaxis, $-\tilde{\chi} \gg 1$, also play a critical role to ensure that Solar System tests of gravity are satisfied by the K-mouflage model, but we do not consider this regime in this paper.

Although K-mouflage theories involve high-order derivative interactions, they do not suffer from quantum-mechanical problems such unitarity violation in their interaction with matter [17, 18], as explained in the appendix C.

C. K-mouflage coupling function

The coupling function $A(\varphi)$ has the low-φ expansion

$$A(\varphi) = 1 + \frac{\beta\varphi}{\tilde{M}_{\rm Pl}} + ..., \tag{8}$$

where the dots stand for higher-order terms. The normalization of the first term does not entail any loss of generality and only corresponds to a normalization of coordinates. At early times, $\tilde{t} \to 0$, we have $\bar{\varphi} \to 0$ and $g_{\mu\nu} \to \tilde{g}_{\mu\nu}$. More generally, we define the coupling β as

$$\beta(\varphi) = \tilde{M}_{\rm Pl}\frac{\mathrm{d}\ln A}{\mathrm{d}\varphi}. \tag{9}$$

It is constant for exponential coupling functions, $A(\varphi) = \exp[\beta\varphi/\tilde{M}_{\rm Pl}]$. Without loss of generality, we take $\beta > 0$ (which simply defines the sign of the scalar field φ).

Cosmological and Solar System constraints imply $\beta \lesssim 0.1$, see Ref. [12]. Moreover, we have the scaling $|\beta\bar{\varphi}/\tilde{M}_{\rm Pl}| \sim \beta^2 \ll 1$, see Ref.[7], as we shall check in Fig. 4 below (see also Ref. [9]). Therefore, in realistic models, we have $|\bar{A} - 1| \lesssim 0.1$ and the higher-order terms in the expansion (8) only have a small quantitative impact. We shall also check in Fig. 13 below that the fluctuations of the scalar field are small, $|\varphi - \bar{\varphi}| \ll |\bar{\varphi}|$, so that the coupling function $A(\varphi)$ remains dominated by the low-order terms of the expansion (8) in clusters of galaxies (and at smaller scales). This can be readily understood from the fact that realistic models should have a fifth force that is not greater than the standard Newtonian force. This typically implies $|\delta A/A| \lesssim |\Psi_{\rm N}|$, where $\Psi_{\rm N}$ is the Newtonian potential, whence $|\beta\delta\varphi/\tilde{M}_{\rm Pl}| \lesssim 10^{-5}$.

D. Equations of motion in the Einstein frame

Observable effects, such as lensing or two point correlations that can be measured, are independent of the choice of frame, so that we can work in either the Einstein or the Jordan frame. As explained in the introduction, for our purposes the Jordan frame is more convenient and more transparent. Indeed, in this frame both the matter and radiation components obey their usual equations of motion, e.g. the matter energy-momentum tensor satisfies $\nabla_\mu T^\mu_\nu = 0$ so that the matter density obeys the usual conservation equation. Moreover, particle masses and atomic emission or absorption lines do not evolve with the cosmic time (whereas they do in the Einstein

frame). Then, the only effect of the scalar field is to change the gravitational sector, that is, the Friedmann equations that determine the background cosmological expansion rate and the relation between the metric gravitational potentials and the matter density fluctuations (i.e., it leads to modified Poisson equations that can be interpreted as a fifth force).

Therefore, in this article we work in the Jordan frame and compute observable effects, in particular the properties of clusters of galaxies, in this frame. However, to simplify the derivation of the equations of motion, it is convenient to first derive the Friedmann equations and the equations that govern the growth of cosmological large-scale structures in the Einstein frame, where gravity takes the standard form. In a second step, we will use these results to obtain the equations of motion in the Jordan frame through a change of variables, in Sec. III. Afterwards, all our computations will remain in the Jordan frame.

Thus, we describe in the appendix A the derivation of the equations of motion of the scalar field and of the matter component in the Einstein frame, for a cosmological fluid with a nonzero pressure. In this section we only give the main results, which will be needed to obtain the equations of motion in the Jordan frame in Sec. III.

We consider three components of the energy density of the Universe, a matter fluid with nonzero pressure, radiation, and the scalar field. The Einstein-frame and Jordan-frame matter energy-momentum tensors are given by

$$\tilde{T}_{\mu\nu} = \frac{-2}{\sqrt{-\tilde{g}}}\frac{\delta S_{\rm m}}{\delta \tilde{g}^{\mu\nu}}, \quad T_{\mu\nu} = \frac{-2}{\sqrt{-g}}\frac{\delta S_{\rm m}}{\delta g^{\mu\nu}}, \tag{10}$$

where we dropped the subscript "m". The conformal transformation (2) gives

$$T_{\mu\nu} = A^{-2}\tilde{T}_{\mu\nu}, \quad T^{\mu}_{\nu} = A^{-4}\tilde{T}^{\mu}_{\nu}, \quad T^{\mu\nu} = A^{-6}\tilde{T}^{\mu\nu}, \tag{11}$$

where we use $g^{\mu\nu}$ ($\tilde{g}^{\mu\nu}$) to raise indices in T ($\tilde{T}$), and the relation $g^{\mu\nu} = A^{-2}\tilde{g}^{\mu\nu}$. In particular, the Einstein-frame and Jordan-frame densities and pressures are related by

$$\tilde{\rho} = A^4\rho, \quad \tilde{p} = A^4 p. \tag{12}$$

We work in the non-relativistic limit, $v^2 \ll 1$ where v is the mean fluid peculiar velocity, and in the weak field regime, $\tilde{\Psi}_{\rm N} \ll 1$, where $\tilde{\Psi}_{\rm N}$ is the Newtonian gravitational potential. Moreover, assuming the usual Cold Dark Matter (CDM) scenario for the dark matter, the matter pressure $\tilde{p}$ is negligible on cosmological scales and it arises from the small-scale nonlinear processes, such as the collapse of gas clouds which generate shocks, or the virialization of of dark matter halos (which generate an effective pressure through the velocity dispersion of the matter particles). Then, $\tilde{p} \sim \tilde{\rho}c_s^2$, where c_s is the speed of sound or the velocity dispersion, and $c_s^2 \sim \tilde{\Psi}_{\rm N}$ because it is generated by the gravitational collapse (as in hydrostatic equilibrium where pressure gradients balance the gravitational force). In addition, we consider the small-scale (sub-horizon) limit, $k/\tilde{a}\tilde{H} \gg 1$, where spatial gradients dominate over time derivatives and quasi-static approximations apply. Thus, we focus on the regime defined by

$$v^2 \ll 1, \ \ \tilde{\Psi}_{\rm N} \ll 1, \ \ \frac{\tilde{p}}{\tilde{\rho}} \sim c_s^2 \sim \tilde{\Psi}_{\rm N} \ll 1, \quad \frac{k}{\tilde{a}\tilde{H}} \gg 1. \tag{13}$$

As the background level, the matter background pressure is zero, $\bar{\tilde{p}} = 0$, and the Einstein-frame Friedmann equations read as

$$3\tilde{M}_{\rm Pl}^2\tilde{H}^2 = \bar{\tilde{\rho}} + \bar{\tilde{\rho}}_{\rm (r)} + \bar{\tilde{\rho}}_{\varphi}, \tag{14}$$

$$-2\tilde{M}_{\rm Pl}^2\frac{{\rm d}\tilde{H}}{{\rm d}\tilde{t}} = \bar{\tilde{\rho}} + \bar{\tilde{\rho}}_{\rm (r)} + \bar{\tilde{p}}_{\rm (r)} + \bar{\tilde{\rho}}_{\varphi} + \bar{\tilde{p}}_{\varphi}, \tag{15}$$

where $\bar{\tilde{\rho}}$, $\bar{\tilde{\rho}}_{\rm (r)}$ and $\bar{\tilde{p}}_{\rm (r)} = \bar{\tilde{\rho}}_{\rm (r)}/3$ are the background matter and radiation densities and pressure, which evolve as

$$\frac{{\rm d}\bar{\tilde{\rho}}}{{\rm d}\tilde{t}} = -3\tilde{H}\bar{\tilde{\rho}} + \bar{\tilde{\rho}}\frac{{\rm d}\ln\bar{A}}{{\rm d}\tilde{t}}, \quad \frac{{\rm d}\bar{\tilde{\rho}}_{\rm (r)}}{{\rm d}\tilde{t}} = -4\tilde{H}\bar{\tilde{\rho}}_{\rm (r)}, \tag{16}$$

while $\bar{\tilde{\rho}}_{\varphi}$ and $\bar{\tilde{p}}_{\varphi}$ are the background scalar-field density and pressure, given by

$$\bar{\tilde{\rho}}_{\varphi} = \mathcal{M}^4(2\bar{\tilde{\chi}}\bar{K}' - \bar{K}), \quad \bar{\tilde{p}}_{\varphi} = \mathcal{M}^4\bar{K}, \tag{17}$$

with

$$\bar{\tilde{\chi}} = \frac{1}{2\mathcal{M}^4}\left(\frac{{\rm d}\bar{\varphi}}{{\rm d}\tilde{t}}\right)^2. \tag{18}$$

(Throughout this paper, we consider a flat universe with zero background curvature.) The background scalar field obeys the Klein-Gordon equation

$$\frac{\rm d}{{\rm d}\tilde{t}}\left[\tilde{a}^3\frac{{\rm d}\bar{\varphi}}{{\rm d}\tilde{t}}\bar{K}'\right] = -\tilde{a}^3\bar{\tilde{\rho}}\frac{{\rm d}\ln\bar{A}}{{\rm d}\bar{\varphi}}. \tag{19}$$

For the matter perturbations, the continuity and Euler equations write as

$$\frac{\partial\tilde{\rho}}{\partial\tau} + \nabla\cdot(\tilde{\rho}\mathbf{v}) + 3\tilde{\mathcal{H}}\tilde{\rho} = \tilde{\rho}\frac{{\rm d}\ln\bar{A}}{{\rm d}\tau}, \tag{20}$$

$$\frac{\partial\mathbf{v}}{\partial\tau} + (\mathbf{v}\cdot\nabla)\mathbf{v} + \left(\tilde{\mathcal{H}} + \frac{{\rm d}\ln\bar{A}}{{\rm d}\tau}\right)\mathbf{v} = -\nabla(\tilde{\Psi}_{\rm N} + \ln A) - \frac{\nabla\tilde{p}}{\tilde{\rho}}, \tag{21}$$

where the Einstein-frame Newtonian potential is given by the Poisson equation

$$\frac{1}{\tilde{a}^2}\nabla^2\tilde{\Psi}_{\rm N} = \frac{1}{2\tilde{M}_{\rm Pl}^2}\delta\tilde{\rho}. \tag{22}$$

In the small-scale (quasi-static) limit, the Klein-Gordon equation for the scalar field becomes

$$\frac{1}{\tilde{a}^2}\nabla\cdot(\nabla\varphi\ \bar{K}') = \frac{{\rm d}\ln\bar{A}}{{\rm d}\bar{\varphi}}\delta\tilde{\rho}. \tag{23}$$

Here we also used the fact that the fluctuations of φ can be neglected in the factor K', so that the Klein-Gordon equation can actually be linearized in the scalar field, while keeping the matter density fluctuations nonlinear. See Ref. [8] for a detailed discussion and an explicit computation of the matter power spectrum, up to one-loop order, that includes up to the cubic term in φ in Eq.(23), which is checked to make no quantitative difference for cosmological large-scale structures of cluster sizes and beyond. This corresponds to the fact that clusters are not screened by the nonlinear K-mouflage mechanism, which comes into play at much smaller scales and higher densities, as in the Solar System.

III. EQUATIONS OF MOTION IN THE JORDAN FRAME

We now derive the equations of motion of the scalar field and of the matter component in the Jordan frame. To do so, we use the results obtained in Sec. II D in the Einstein frame, and express these equations in terms of Jordan-frame variables.

A. Background dynamics

The Jordan-frame metric $g_{\mu\nu}$ is related to the Einstein-frame metric $\tilde{g}_{\mu\nu}$ by the conformal transformation (2). As seen in Eqs.(3)-(5), this leads to a rescaling of the scale factor and of physical time and distance, while the conformal coordinates are unchanged. The Hubble expansion rates, $H = \mathrm{d}\ln a/\mathrm{d}t$ and $\tilde{H} = \mathrm{d}\ln\tilde{a}/\mathrm{d}\tilde{t}$, are also different and related by

$$H = \frac{\tilde{H}(1+\tilde{\epsilon}_2)}{\bar{A}} = \frac{\tilde{H}}{\bar{A}(1-\epsilon_2)}, \tag{24}$$

where $\tilde{\epsilon}_2(t)$ was defined in Eq.(A45) and verifies $\mathrm{d}\ln\bar{A}/\mathrm{d}\tilde{t} = \tilde{\epsilon}_2\tilde{H}$, and we introduced its Jordan-frame counterpart,

$$\epsilon_2(t) = \frac{\mathrm{d}\ln\bar{A}}{\mathrm{d}\ln a}, \quad \epsilon_2 = \frac{\tilde{\epsilon}_2}{1+\tilde{\epsilon}_2}, \quad \tilde{\epsilon}_2 = \frac{\epsilon_2}{1-\epsilon_2}. \tag{25}$$

The Einstein-frame and Jordan-frame densities and pressures are related as in Eq.(12), so that the Friedman equation (14) gives

$$3M_{\rm Pl}^2H^2 = (1-\epsilon_2)^{-2}\left(\bar{\rho}+\bar{\rho}_{(\rm r)}+\bar{\rho}_\varphi\right), \tag{26}$$

where we introduced the Jordan-frame reduced Planck mass,

$$M_{\rm Pl}^2(t) = \tilde{M}_{\rm Pl}^2/\bar{A}(t)^2. \tag{27}$$

Thus, in the Jordan frame, Newton's constant, $\mathcal{G} = 1/8\pi M_{\rm Pl}^2$, varies with time, as $\mathcal{G}(t) = \tilde{\mathcal{G}}\bar{A}^2 \propto \bar{A}^2$. Equation (26) shows how the Friedmann equation is modified in the Jordan frame, as compared with the usual General Relativity result, because the gravitational Einstein-Hilbert action is defined in terms of the auxiliary metric $\tilde{g}_{\mu\nu}$. Substituting for $g_{\mu\nu}$ this effectively corresponds to a change of the Einstein-Hilbert action. At the background level, this simply introduces the time-dependent functions $\bar{A}(t)$ and $\epsilon_2(t)$ in Eq.(26).

We can also write Eq.(26) in the standard form (albeit with a time-dependent reduced Planck mass), as

$$3M_{\rm Pl}^2H^2 = \bar{\rho}+\bar{\rho}_{(\rm r)}+\bar{\rho}_{\rm de}, \tag{28}$$

by defining the dark-energy component as the energy density that is "missing" in the Friedmann equation to match the Hubble rate, after we sum over the other matter and radiation components. This yields

$$\bar{\rho}_{\rm de} \equiv \bar{\rho}_\varphi + \frac{2\epsilon_2-\epsilon_2^2}{(1-\epsilon_2)^2}\left(\bar{\rho}+\bar{\rho}_{(\rm r)}+\bar{\rho}_\varphi\right). \tag{29}$$

This interpretation corresponds to the case where measurements of the Hubble rate and of the matter and radiation densities are performed in the Jordan frame and the remaining part, which explains the accelerated expansion, is ascribed to the dark-energy component, [as in the usual Λ-CDM case, where the background dark energy is also measured from the missing energy density that is required to account for $H(z)$]. This is a natural configuration, as $a(t)$ and $H(t)$ are obtained from redshift measurements of standard candles, which assumes that atomic absorption and emission lines are the same at distant redshifts as in the laboratory. By definition, this is the case in the Jordan frame but not in the Einstein frame (where particle masses are actually time dependent). On the other hand, these standard candles must not depend on the local gravity, because in the Jordan frame Newton's constant becomes time dependent, so that these candles are no longer standard (i.e., similar to those at $z = 0$). This rules out supernovae (which involve both local gravity and electrodynamics, within the star) but allows one to use geometric candles such as baryon acoustic oscillations [19, 20] or the Alcock-Paczynski test [21].

Using Eq.(16), the matter and radiation densities now evolve as

$$\frac{\mathrm{d}\bar{\rho}}{\mathrm{d}t} = -3H\bar{\rho}, \quad \frac{\mathrm{d}\bar{\rho}_{(\rm r)}}{\mathrm{d}t} = -4H\bar{\rho}_{(\rm r)}. \tag{30}$$

Thus, we recover the usual conservation equations for matter and radiation in the Jordan frame, whence

$$\bar{\rho}(t) = \frac{\bar{\rho}_0}{a^3}, \quad \bar{\rho}_{(\rm r)}(t) = \frac{\bar{\rho}_{(\rm r)0}}{a^4}, \quad \text{with} \quad a_0 = 1, \tag{31}$$

where $\bar{\rho}_0$ are the mean Jordan-frame energy densities today, at $z = 0$, and we normalized the Jordan-frame scale factor by $a_0 = 1$.

From Eq.(A11), with $\bar{\tilde{p}} = 0$, and Eq.(29), the Jordan-frame dark-energy density evolves as

$$\frac{\mathrm{d}\bar{\rho}_{\rm de}}{\mathrm{d}t} = -3H\left(\bar{\rho}_{\rm de}+\bar{p}_{\rm de}\right), \tag{32}$$

where we defined the Jordan-frame dark-energy pressure as

$$\bar{p}_{\rm de} = \bar{p}_\varphi + \frac{\epsilon_2}{1-\epsilon_2}(\bar{p}_{(\rm r)}+\bar{p}_\varphi) + \left(\epsilon_2 - \frac{2}{1-\epsilon_2}\frac{{\rm d}\epsilon_2}{{\rm d}\ln a}\right) \times \frac{\bar{\rho}+\bar{\rho}_{(\rm r)}+\bar{\rho}_\varphi}{3(1-\epsilon_2)^2}. \quad (33)$$

On the other hand, from Eq.(19) the Klein-Gordon equation reads as

$$\frac{\rm d}{{\rm d}t}\left[\bar{A}^{-2}a^3\frac{{\rm d}\bar{\varphi}}{{\rm d}t}\bar{K}'\right] = -a^3\bar{\rho}\frac{{\rm d}\ln\bar{A}}{{\rm d}\bar{\varphi}}. \quad (34)$$

This can be integrated as

$$\frac{{\rm d}\bar{\varphi}}{{\rm d}t}\bar{K}' = -\bar{A}^2a^{-3}\int_0^t {\rm d}t'\,\frac{\bar{\rho}_0\beta(t')}{\tilde{M}_{\rm Pl}}, \quad (35)$$

because the integration constant must vanish to recover a realistic early-time cosmology [7].

Finally, we define the Jordan-frame cosmological parameters as

$$\Omega_{\rm m} = \frac{\bar{\rho}}{\rho_{\rm crit}}, \quad \Omega_{(\rm r)} = \frac{\bar{\rho}_{(\rm r)}}{\rho_{\rm crit}}, \quad \Omega_{\rm de} = \frac{\bar{\rho}_{\rm de}}{\rho_{\rm crit}}, \quad (36)$$

where $\rho_{\rm crit} = 3M_{\rm Pl}^2H^2 = \bar{A}^{-4}(1-\epsilon_2)^{-2}\tilde{\rho}_{\rm crit}$ is the Jordan-frame critical density. This gives

$$\Omega_{\rm m} = (1-\epsilon_2)^2\tilde{\Omega}_{\rm m}, \quad \Omega_{(\rm r)} = (1-\epsilon_2)^2\tilde{\Omega}_{(\rm r)}, \quad (37)$$

and

$$\Omega_{\rm de} = \tilde{\Omega}_\varphi + (2\epsilon_2-\epsilon_2^2)(\tilde{\Omega}_{\rm m}+\tilde{\Omega}_{(\rm r)}). \quad (38)$$

We can check that $\Omega_{\rm m}+\Omega_{(\rm r)}+\Omega_{\rm de} = \tilde{\Omega}_{\rm m}+\tilde{\Omega}_{(\rm r)}+\tilde{\Omega}_\varphi = 1$. The effective dark-energy equation of state in the Jordan frame is simply defined as

$$w_{\rm de} = \bar{p}_{\rm de}/\bar{\rho}_{\rm de}. \quad (39)$$

B. Perturbations

The dynamics of large-scale perturbations in the Jordan frame are also obtained from the equations derived in the Einstein frame in Sec. II D.

In the Einstein frame, the Newtonian gauge metric (A16) reads as ${\rm d}\tilde{s}^2 = \tilde{a}^2[-(1+2\tilde{\Psi}_{\rm N}){\rm d}\tau^2+(1-2\tilde{\Psi}_{\rm N}){\rm d}\mathbf{x}^2]$, where we used Eq.(A31). In the Jordan frame, we write

$${\rm d}s^2 = a^2[-(1+2\Phi){\rm d}\tau^2+(1-2\Psi){\rm d}\mathbf{x}^2]. \quad (40)$$

Then, using ${\rm d}s^2 = A^2{\rm d}\tilde{s}^2$ and $a = \bar{A}\tilde{a}$, we obtain, up to first order in $\delta A = A-\bar{A}$,

$$\Phi = \Psi_{\rm N}+\frac{\delta A}{\bar{A}}, \quad \Psi = \Psi_{\rm N}-\frac{\delta A}{\bar{A}}, \quad (41)$$

where we introduced the Jordan-frame Newtonian potential, given by

$$\frac{1}{a^2}\nabla^2\Psi_{\rm N} = \frac{1}{2M_{\rm Pl}^2}\delta\rho, \quad \text{whence} \quad \Psi_{\rm N} = \tilde{\Psi}_{\rm N}. \quad (42)$$

The last equality follows from Eqs.(22) and (27). Therefore, in the Jordan frame the two metric potentials are no longer equal, but their sum remains equal to $2\Psi_{\rm N}$. This is related to the fact that photons do not feel the effect of the fifth force, see also Eq.(A7). Therefore, weak lensing statistics show the same dependence on the matter density fluctuations as in GR and the impact of the modified gravity only arises through the different evolution of the density field and the time-dependent Newton constant, see also Sec.V H below.

The Klein-Gordon equation (23) reads as

$$\frac{1}{a^2}\nabla^2\varphi = \frac{\beta\bar{A}}{\bar{K}'M_{\rm Pl}}\delta\rho, \quad (43)$$

and, up to first order over $\delta\varphi$, we obtain

$$\frac{\delta A}{\bar{A}} = \frac{\beta}{M_{\rm Pl}\bar{A}}\delta\varphi, \quad \frac{1}{a^2}\nabla^2\frac{\delta A}{\bar{A}} = \frac{\beta^2}{M_{\rm Pl}^2\bar{K}'}\delta\rho. \quad (44)$$

This also gives

$$\frac{1}{a^2}\nabla^2\Phi = \frac{1+\epsilon_1(t)}{2M_{\rm Pl}^2(t)}\delta\rho \quad \text{and} \quad \Phi = (1+\epsilon_1)\Psi_{\rm N}, \quad (45)$$

where ϵ_1 is defined by

$$\epsilon_1(t) = \frac{2\beta^2}{\bar{K}'}, \quad (46)$$

and we recover the same factor as in the first relation (A45).

The continuity equation (20) and the Euler equation (21) become

$$\frac{\partial\rho}{\partial\tau}+\nabla\cdot(\rho\mathbf{v})+3\mathcal{H}\rho = 0 \quad (47)$$

and

$$\frac{\partial\mathbf{v}}{\partial\tau}+(\mathbf{v}\cdot\nabla)\mathbf{v}+\mathcal{H}\mathbf{v} = -\nabla\Phi-\frac{\nabla p}{\rho}. \quad (48)$$

Therefore, in contrast with the Einstein frame, in the Jordan frame the continuity and Euler equations take the same form as in Λ-CDM, and the coupling to the scalar field φ only gives rise to the modified Poisson equation (45), in terms of the formation of large-scale structures. There is no longer a non-conservation term in the continuity equation nor an additional friction term in the Euler equation. However, in contrast with the Einstein frame and the Λ-CDM cosmology, the two gravitational potentials Φ and Ψ that enter the Newtonian gauge metric are now different.

C. Formation of large-scale structures

Introducing the Jordan-frame matter density contrast,

$$\delta = \delta\rho/\bar{\rho}, \tag{49}$$

the continuity equation (47) also writes as

$$\frac{\partial\delta}{\partial\tau} + \nabla\cdot[(1+\delta)\mathbf{v}] = 0. \tag{50}$$

This is the same equation as (A40) and we have

$$\delta = \hat{\delta} = \tilde{\delta}. \tag{51}$$

Indeed the matter density contrasts in the Einstein frame, whether we consider the density $\tilde{\rho}$ or the "conserved" density $\hat{\rho}$ of Eq.(A13) (in case of zero pressure), and in the Jordan frame, are equal within the approximations described in the previous sections.

On perturbative scales, we again set the pressure term to zero and we introduce the two-component vector

$$\psi \equiv \begin{pmatrix} \psi_1 \\ \psi_2 \end{pmatrix} \equiv \begin{pmatrix} \delta \\ -(\nabla\cdot\mathbf{v})/(\mathrm{d}a/\mathrm{d}t) \end{pmatrix}. \tag{52}$$

Equations (A42) and (A43) become

$$\frac{\partial\psi_1}{\partial\ln a} - \psi_2 = \int \mathrm{d}\mathbf{k}_1\mathrm{d}\mathbf{k}_2\ \delta_D(\mathbf{k}_1+\mathbf{k}_2-\mathbf{k})\hat{\alpha}(\mathbf{k}_1,\mathbf{k}_2) \times \psi_2(\mathbf{k}_1)\psi_1(\mathbf{k}_2), \tag{53}$$

$$\frac{\partial\psi_2}{\partial\ln a} - \frac{3}{2}\Omega_\mathrm{m}(1+\epsilon_1)\psi_1 + \left(2+\frac{1}{H^2}\frac{\mathrm{d}H}{\mathrm{d}t}\right)\psi_2 = \int\mathrm{d}\mathbf{k}_1\mathrm{d}\mathbf{k}_2\ \delta_D(\mathbf{k}_1+\mathbf{k}_2-\mathbf{k})\hat{\beta}(\mathbf{k}_1,\mathbf{k}_2)\psi_2(\mathbf{k}_1)\psi_2(\mathbf{k}_2). \tag{54}$$

We recover the same form as for the Λ-CDM cosmology, except for the factor ϵ_1 that corresponds to a time-dependent amplification of Newton's gravity, from the modified Poisson equation (45).

On large scales or at early times, we can again linearize the equations of motion and the evolution equation (A46) for the linear modes becomes

$$\frac{\mathrm{d}^2 D}{\mathrm{d}(\ln a)^2} + \left(2+\frac{1}{H^2}\frac{\mathrm{d}H}{\mathrm{d}t}\right)\frac{\mathrm{d}D}{\mathrm{d}\ln a} - \frac{3}{2}\Omega_\mathrm{m}(1+\epsilon_1)D = 0. \tag{55}$$

Again, as compared with the Einstein-frame Eq.(A46) we find that the coefficient ϵ_2 has disappeared and the only difference from the Λ-CDM case is the time-dependent amplification of the gravitational term by $(1+\epsilon_1)$.

As in Galileon models, but in contrast with $f(R)$, Dilaton and Symmetron models, the linear growing modes remain scale independent as in the Λ-CDM cosmology. This is because we did not include a potential $V(\varphi)$ in the scalar-field Lagrangian (6) and the field is massless. Thus, the amplification of gravity extends up to the Hubble scale and is only damped on galactic and smaller scales by the nonlinear K-mouflage mechanism. See Sec. VI for a discussion and comparison with other modified-gravity theories.

D. Spherical collapse dynamics

As can be derived from Eq.(48), on large scales where the pressure is negligible, the particle trajectories $\mathbf{r}(t)$ read as

$$\frac{\mathrm{d}^2\mathbf{r}}{\mathrm{d}t^2} - \frac{1}{a}\frac{\mathrm{d}^2 a}{\mathrm{d}t^2}\mathbf{r} = -\nabla_\mathbf{r}\Phi, \tag{56}$$

where $\mathbf{r} = a\mathbf{x}$ is the physical coordinate and $\nabla_\mathbf{r} = \nabla/a$ the gradient operator in physical coordinates. To study the spherical collapse before shell crossing, it is convenient to label each shell by its Lagrangian radius q or enclosed mass M, and to introduce its normalized radius $y(t)$ by

$$y(t) = \frac{r(t)}{a(t)q} \quad\text{with}\quad q = \left(\frac{3M}{4\pi\bar{\rho}_0}\right)^{1/3}, \quad y(t=0) = 1. \tag{57}$$

In particular, the matter density contrast within radius $r(t)$ reads as

$$1 + \delta(<r) = y(t)^{-3}. \tag{58}$$

Since the Poisson equation (46) is only modified by the time-dependent prefactor $1+\epsilon_1(t)$ and the time dependence of Newton's constant, for a spherical system the gravitational force is still set by the total mass within radius r,

$$\frac{\mathrm{d}\Phi}{\mathrm{d}r} = (1+\epsilon_1)\frac{\mathcal{G}\delta M}{r^2}, \tag{59}$$

where $\delta M = 4\pi\delta(<r)\bar{\rho}r^3/3$. Then, Eq.(56) gives for the evolution of the normalized radius y, or density contrast $\delta(<r) = y^{-3}-1$,

$$\frac{\mathrm{d}^2 y}{\mathrm{d}(\ln a)^2} + \left(2+\frac{1}{H^2}\frac{\mathrm{d}H}{\mathrm{d}t}\right)\frac{\mathrm{d}y}{\mathrm{d}\ln a} + \frac{\Omega_\mathrm{m}}{2}(1+\epsilon_1)(y^{-3}-1)y = 0. \tag{60}$$

Again, as in the Λ-CDM cosmology but in contrast with $f(R)$, Dilaton and Symmetron models, the spherical collapse is scale invariant so that the dynamics of different mass shells decouple. This applies to the unscreened regime, from clusters of galaxies up to the Hubble radius.

E. Halo mass function

As usual, we can write the halo mass function $n(M)\mathrm{d}M/M$ as

$$n(M)\frac{\mathrm{d}M}{M} = \frac{\bar{\rho}_0}{M}f(\nu)\frac{\mathrm{d}\nu}{\nu}, \quad\text{with}\quad \nu = \frac{\delta_L}{\sigma(M)}, \tag{61}$$

where we used the fact that the linear growing modes are scale independent [so that $\delta_L/\sigma(M) = \delta_{L\mathrm{i}}/\sigma_\mathrm{i}(M)$, where the subscript "i" refers to the high redshift z_i where the Gaussian initial conditions are defined, far before the dark-energy era]. Here $\sigma(M)$ is the root mean square of

the linear density contrast at scale M and δ_L is the linear density contrast associated with the nonlinear density threshold $\Delta_{\rm m}$ that defines the virialized halos. The mapping $\delta_L \to \delta$ is obtained by solving the spherical collapse dynamics (60), with the initial condition $y_{\rm i} = 1-\delta_{L\rm i}/3$ at a very high redshift $z_{\rm i}$. Inverting this relation gives the linear density threshold δ_L that is associated with a given nonlinear density threshold $\delta = \Delta_{\rm m}$, where the subscript "m" denotes that $\delta = y^{-3}-1$ is the density contrast with respect to the mean density of the Universe.

The scaling variable ν directly measures the probability of density fluctuations in the Gaussian initial conditions. Then, we take for the scaling function $f(\nu)$ the fit to Λ-CDM simulations obtained in [22], which obeys the exponential tail $f(\nu) \sim e^{-\nu^2/2}$ at large ν. This means that the mass function (61) shows the correct large-mass tail, which is set by the Gaussian initial conditions.

F. Planck masses

It is interesting to note that, depending on the physical process that is considered, one can define several effective Planck masses. In other words, if we assume General Relativity and measure the reduced Planck mass or Newton's constant from different sets of observations, we would obtain different values. This could be used as a signature of the modified-gravity theory.

From Eq.(26), the effective Planck mass that would be read from the Friedmann equation, at the background level, is

$$M^2_{\rm Pl(Friedmann)}(t) = \frac{\tilde{M}^2_{\rm Pl}(1-\epsilon_2(t))^2}{\bar{A}^2(t)}. \qquad (62)$$

On the other hand, with respect to large-scale density fluctuations in the cosmological unscreened regime, where the Klein-Gordon equation can be linearized over the scalar field, the effective Planck mass that would be read from the modified Poisson equation (45) is

$$M^2_{\rm Pl(unscreened)}(t) = \frac{\tilde{M}^2_{\rm Pl}}{\bar{A}^2(t)(1+\epsilon_1(t))} \qquad (63)$$

On small astrophysical scales, within the highly nonlinear screened regime, the effective Planck mass is instead the one defined in Eq.(27),

$$M^2_{\rm Pl(screened)}(t) = \frac{\tilde{M}^2_{\rm Pl}}{\bar{A}(t)^2}. \qquad (64)$$

The difference between these various definitions is a signature of the modification of gravity associated with the scalar-field models (1), as seen from the Jordan frame.

G. Symmetry of large-scale gravitational clustering

On large scales, where we neglect shell crossing and pressure, the dynamics of gravitational clustering is given by Eqs.(50), (48) (with $\tilde{p}=0$), and (45). It is convenient to define the rescaled velocity and metric potential by

$$\mathbf{v} = \frac{{\rm d}a}{{\rm d}t} f\,\mathbf{u}, \quad \Phi = \left(\frac{{\rm d}a}{{\rm d}t} f\right)^2 \phi, \qquad (65)$$

where we introduced the linear growth rate

$$f = \frac{{\rm d}\ln D_+}{{\rm d}\ln a}, \qquad (66)$$

and to change the time variable from t to $\ln D_+$. Then, the equations of motion write as

$$\frac{\partial\delta}{\partial \ln D_+} + \nabla\cdot[(1+\delta)\mathbf{u}] = 0, \qquad (67)$$

$$\frac{\partial\mathbf{u}}{\partial \ln D_+} + (\mathbf{u}\cdot\nabla)\mathbf{u} + (\kappa-1)\mathbf{u} = -\nabla\phi, \qquad (68)$$

$$\nabla^2\phi = \kappa\,\delta, \qquad (69)$$

where we introduced the time-dependent factor $\kappa(t)$, defined by

$$\kappa(t) = \frac{4\pi\mathcal{G}\bar{\rho}(1+\epsilon_1)}{\left(\frac{{\rm d}\ln D_+}{{\rm d}t}\right)^2} = \frac{3\Omega_{\rm m}}{2f^2}(1+\epsilon_1). \qquad (70)$$

Therefore, after the change of time coordinate $t \to \ln D_+$ and the rescaling (65), the only dependence on cosmology that is left in large-scale gravitational clustering is encapsulated in the function $\kappa(t)$. This remains valid beyond shell crossing but it breaks down on small scales where baryonic effects become important and introduce new characteristic scales, which cannot be absorbed by the change of variables (65). Nevertheless, on large scales where gravity is the dominant process, this symmetry means that all cosmological scenarios with the same function $\kappa(D_+)$ show the same density and velocity fields $\{\delta, \mathbf{u}\}$. In particular, this means that quintessence models, where only the background dynamics is modified (i.e., the Hubble expansion rate $H(z)$), and modified-gravity models or dark-energy models (with dark-energy fluctuations) that only give rise to a modification of Poisson equation by a time-dependent Newton's constant, are equivalent with respect to gravitational clustering, if they show the same function $\kappa(D_+)$. In the context of Λ-CDM cosmology, this property has also been used to derive approximate consistency relations satisfied by the matter correlation functions [valid at the nonlinear level within the approximation where the dependence on cosmology of $\kappa(D_+)$ can be neglected] [23–25].

In the case of the K-mouflage scenarios, this symmetry only holds on large scales (down to cluster scales) where the Klein-Gordon equation can be linearized over φ, as in Eq.(43). On smaller scales (galactic scales and below), higher-order terms over φ become important and the nonlinear K-mouflage screening mechanism comes into play. Then, the modified Poisson equation no longer takes the linear form (45) and the symmetry (70) breaks

down. On even smaller scales we actually recover General Relativity as $\Phi \simeq \Psi_{\rm N}$, because the fifth force is screened. In hierarchical scenarios, where smaller scales collapse first, larger scales are not very sensitive to the details of the clustering on smaller scales, while small collapsed scales are sensitive to the clustering up to the largest scale that has turned nonlinear. Therefore, we expect the symmetry (70) to apply to scales that are greater than the transition to the K-mouflage screening regime, and not to smaller scales (even though we recover General Relativity far inside the nonlinear screening regime). Besides, on such small scales non-gravitational baryonic effects come into play (such as AGN feedback) and the symmetry no longer holds.

For our purposes in this paper, the formulation (67)-(70) explicitly shows that, from cluster scales up to the Hubble scale, K-mouflage cosmologies belong to the same family as the Λ-CDM and quintessence scenarios, with respect to matter clustering. The equations that govern the gravitational dynamics in these rescaled variables take the same form, except for a time-dependent function $\kappa(D_+)$. However, the shape of this function is similar for realistic scenarios (we shall see in Fig. 5 that ϵ_1 is about 2%). Therefore, we can expect that gravitational clustering shows the same qualitative properties in these cosmologies and only small quantitative deviations. In particular, semianalytical methods should work equally well for all these cosmologies, and phenomenological observations, such as the fact that virialized halos are well described by Navarro-Frenk-White (NFW) profiles [26] in Λ-CDM cosmology, should remain valid in other cases. This justifies our modelization of clusters, described in Sec. V below, where we treat Λ-CDM and K-mouflage cosmologies in the same manner.

IV. NUMERICAL RESULTS FOR LARGE-SCALE STRUCTURES

In this paper we consider two simple models for $K(\tilde\chi)$. The first one, which we call the "arctan model" in the following, is defined by:

$$K_{\rm arctan}(\tilde\chi) = -1 + \tilde\chi + K_*[\tilde\chi - \chi_* \arctan(\tilde\chi/\chi_*)], \quad (71)$$

with the low-$\tilde\chi$ expansion

$$\tilde\chi \to 0 : \quad K_{\rm arctan}(\tilde\chi) = -1+\tilde\chi+\frac{K_*}{3}\frac{\tilde\chi^3}{\chi_*^2}-\frac{K_*}{5}\frac{\tilde\chi^5}{\chi_*^4}+... \quad (72)$$

and the choice of parameters

$$K_* = 10^3, \quad \chi_* = 10^2. \quad (73)$$

This gives a K-mouflage model that is consistent with both Solar System and cosmological constraints (with $\beta = 0.1$). For comparison we also consider the model used in [7, 8], which we call the "cubic model" in the following, in which $K(\tilde\chi)$ is a low-order polynomial:

$$K_{\rm cubic}(\tilde\chi) = -1 + \tilde\chi + K_0\tilde\chi^m, \quad (74)$$

and the choice of the parameters

$$m = 3, \quad K_0 = 1. \quad (75)$$

Here Eq.(74) should not be understood as a perturbative expansion around $\tilde\chi = 0$. It is rather a simple model that interpolates between the low-$\tilde\chi$ behavior (7) and a large-$\tilde\chi$ power-law behavior $\propto \tilde\chi^m$. The cubic model is consistent with cosmological constraints but its form at large negative χ, $-\chi \gg 1$, is not consistent with Solar System constraints. Therefore, this is an effective model that applies to the semiaxis $\chi \geq -1$ while the large-negative domain is left unspecified. This is sufficient for our purposes, since the cosmological background and large-scale perturbations correspond to $\chi > 0$ and clusters correspond to $\chi > -1$ (more precisely, $|\chi| \ll 1$).

For both models we choose an exponential form for the coupling function,

$$A(\varphi) = e^{\beta\varphi/\tilde M_{\rm Pl}}, \quad \text{with} \quad \beta = 0.1 \quad (76)$$

We also consider a reference Λ-CDM model for comparison.

All the cosmological scenarios are normalized to the same background cosmological parameters today, $\{\Omega_{\rm m0}, \Omega_{\rm (r)0}, \Omega_{\rm de0}, H_0\}$. In addition, we normalize the Planck mass (27) to the same value $M^2_{\rm Pl0}$ today, as measured by Solar System experiments. This means that we renormalize the Einstein-frame Planck mass by a factor $\bar A_0^2$, where $\bar A_0 = \bar A(z = 0)$,

$$M^2_{\rm Pl}(t) = M^2_{\rm Pl0}\frac{\bar A_0^2}{\bar A(t)^2}, \quad \text{whence} \quad \tilde M^2_{\rm Pl} = M^2_{\rm Pl0}\bar A_0^2. \quad (77)$$

On the other hand, the matter density power spectrum $P(k)$ is normalized to the same value at high redshift, when dark energy is subdominant and both cosmologies almost coincide. However, these different scenarios do not exactly converge in terms of the background expansion rate at a given matter density, because of the different high-redshift reduced Planck masses. Therefore, the normalization to the same power spectrum for the matter density contrast at high z is somewhat arbitrary, since the K-mouflage and Λ-CDM models do not coincide. Nevertheless, for our purposes this is a convenient choice as it illustrates how the difference in the gravitational clustering dynamics that appear at low z, because of the fifth force mediated by the scalar field, affect the late-time density field. [For other normalization choices, it would be difficult to distinguish the effects due to the different normalizations at high z, before the dark-energy era and when the fifth force was negligible, and to the late-time dynamics characterized by different growth rates.] This normalization also corresponds to the case where we can measure the density contrast field, i.e. the patterns of large-scale structures (e.g., the scale associated with the nonlinear transition $\sigma^2 = 1$) at high z, independently of accurate measures of the background density and expansion rate. In practice, this normalization ambiguity

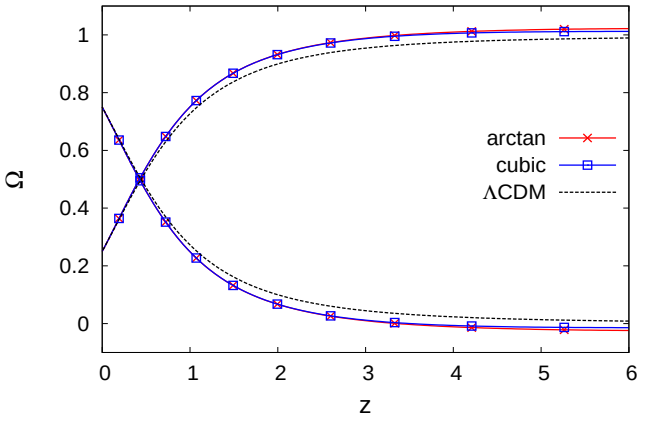

FIG. 1: Evolution with redshift of the matter and dark-energy cosmological parameters $\Omega_{\rm m}(z)$ and $\Omega_{\rm de}(z)$. We display the two K-mouflage models of Eq.(71) (arctan model, red crosses) and Eq.(74) (cubic model, blue squares), and the reference Λ-CDM universe (black dashed lines). The two scalar-field models almost coincide in this figure.

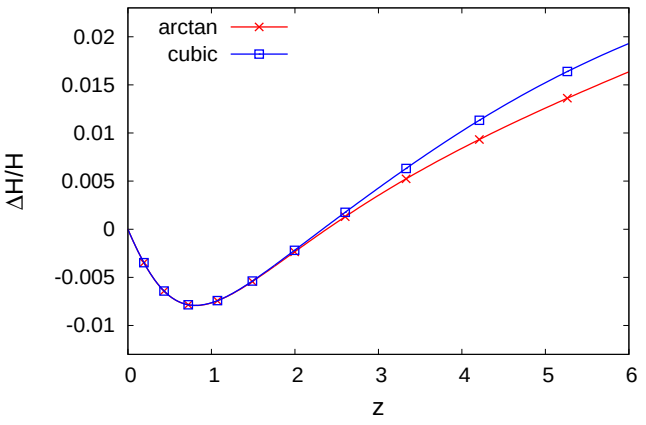

FIG. 2: Relative deviation of the Hubble expansion rate with respect to the Λ-CDM reference, $\Delta H/H = H/H_{\Lambda-{\rm CDM}} - 1$, for the same K-mouflage models as in Fig. 1.

does not appear because one compares each cosmological scenario with the data, rather than comparing with a theoretical reference cosmology (in particular, the best fits associated with different theories will typically have slightly different cosmological parameters and expansion rates at both $z = 0$ and $z \to \infty$).

In the following, we present our results for the choice of cosmological parameters today given by $\Omega_{\rm m0} = 0.25$, $\Omega_{\rm de0} = 0.75$, $h = 0.70$ and $\sigma_8 = 0.7$.

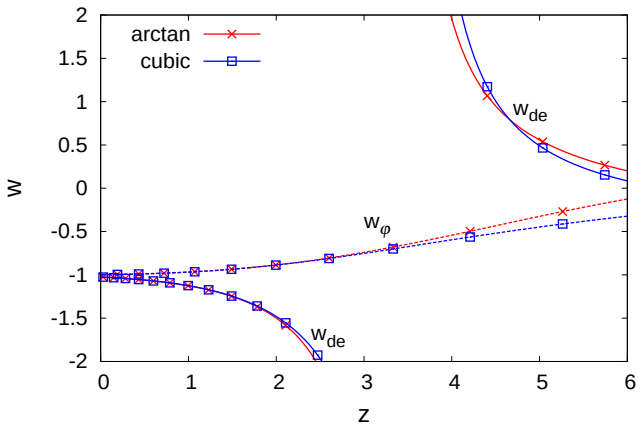

FIG. 3: Effective equation of state parameters $w_{\rm de}(z)$ (solid lines with a divergence and change of sign at $z \simeq 3$) and $w_\varphi(z)$ (dashed lines with a smooth behavior), for the same K-mouflage models as in Fig. 1.

A. Background dynamics

We consider the density parameters $\Omega_{\rm m}(z)$ and $\Omega_{\rm de}(z)$ in Fig. 1 for the two K-mouflage models defined in equations (71) and (74) and for the reference Λ-CDM universe. Since we normalize the density and dark-energy parameters to be equal to the ones observed today, all models coincide at $z = 0$ in terms of background quantities. The deviations from the Λ-CDM scenario are slightly greater for the arctan model (71) than for the cubic model (74), in agreement with [12]. This is due to the fact that $K'(\tilde{\chi})$ is slightly smaller in the former case over the range of redshifts of interest, $z \lesssim 6$, and that deviations from the Λ-CDM scenario typically scale as β^2/K', see for instance Eq.(46) and Ref.[7].

As for studies performed in the Einstein frame [7] (where the cosmological parameters are normalized by their Einstein-frame values today), we find that the dark-energy density becomes negative (and subdominant) at high redshift. This gives $\Omega_{\rm m} > 1$ at high z for the two K-mouflage models (71) and (74) (but as in the Λ-CDM case $\Omega_{\rm m} \to 1$ at high redshift).

In Fig. 2 we consider the relative deviation, $H(z)/H_{\Lambda-{\rm CDM}}(z) - 1$, of the Hubble rate with respect to the Λ-CDM reference. The deviation is slightly larger for the cubic model (74) at $z \sim 6$, but this is only a transient effect because at $z > 12$ the deviation is slightly greater for the arctan model (71), as expected. At moderate redshifts the Hubble expansion rates differ by less than 2% between the three cosmologies that we consider here. This amplitude is mostly set by our choice of coupling constant $\beta = 0.1$, because as recalled above deviations from the Λ-CDM scenario scale as $\beta^2/\bar{K}'$ and at low z we have $\bar{K}' \simeq 1$. Therefore $\beta = 0.1$ typically leads to percent deviations from the Λ-CDM scenario. This value of β (or lower values) is required to satisfy observational

constraints on cosmological and Solar System scales [12], in particular from the expansion rate at the time of Big Bang Nucleosynthesis and from the bounds on the current time derivative of the gravitational coupling $\mathcal{G}$ provided by the Lunar Ranging experiment.

The deviation from the Λ-CDM reference does not vanish at high redshift because the reduced Planck masses are different, see Eq.(77). Indeed, in the K-mouflage models $M_{\rm Pl}^2(t)$ becomes time dependent and we choose to normalize all scenarios by their Planck mass today (when Solar System measurements and laboratory experiments are performed). Note that in studies performed in the Einstein frame [7], where the reduced Planck mass is constant, one can recover the Λ-CDM expansion rate at both $z = 0$ and at high redshift. However, this requires normalizing the matter density today by the conserved density $\hat{\rho}$ of Eq.(A13) instead of the Einstein-frame density $\tilde{\rho}$.

In Fig. 3 we display the effective equation of state parameter for the dark energy, $w_{\rm de} = \bar{p}_{\rm de}/\bar{\rho}_{\rm de}$, evaluated using Eqs.(29) and (33) for $\bar{\rho}_{\rm de}$ and $\bar{p}_{\rm de}$. For both models $w_{\rm de} \to -1$ at late times, mimicking the presence of a cosmological constant. As in studies performed in the Einstein frame, the effective equation of state parameter is beyond -1 at low z and changes sign at a moderate redshift while going through $\pm\infty$ (this does not correspond to a singularity in terms of the Hubble rate or dark-energy density but to the vanishing and change of sign of $\bar{\rho}_{\rm de}$). We also show in Fig. 3 the equation of state parameter w_φ defined as

$$w_\varphi = \frac{\bar{p}_\varphi}{\bar{\rho}_\varphi} = \frac{\bar{K}}{2\bar{\tilde{\chi}}\bar{K}' - \bar{K}}, \tag{78}$$

where we used Eq.(17). In contrast to $w_{\rm de}$, w_φ remains negative over $z \leq 6$ and shows no divergence. The difference between the behaviors of $w_{\rm de}$ and w_φ shows the impact of the coupling between the matter and scalar-field components. This makes the dark-energy density and pressure significantly different from the bare scalar-field ones, see Eqs.(29) and (33), and can even make $\bar{\rho}_{\rm de}$ and $\bar{\rho}_\varphi$ have different signs.

B. Background scalar field

We show in Fig. 4 the background values $\bar{\varphi}$ and $\bar{\tilde{\chi}}$ of the scalar field and of its kinetic term. The scalar field $\bar{\varphi}$ is negative and its amplitude grows with redshift (we chose the normalization $\bar{\varphi} = 0$ at high redshift, $z \to \infty$). We can see that $|\beta\bar{\varphi}/\tilde{M}_{\rm Pl}| \ll 1$ until $z = 0$. Thus, the coupling function $A(\varphi)$ is dominated by its low-order terms in the expansion (8) and choosing for instance $A(\varphi) = (1 + \beta\varphi/n\tilde{M}_{\rm Pl})^n$, with $n > 0$, would give similar results to the exponential choice (76).

The kinetic term $\bar{\tilde{\chi}}$ decreases with time. It goes to infinity at high redshift, $z \to \infty$, and we can check that at low z it is significantly smaller than unity. Then, the kinetic function $K(\tilde{\chi})$ is dominated by its low-order terms in the expansion (7). This explains why the two K-mouflage models converge at low z in the lower panel of Fig. 4.

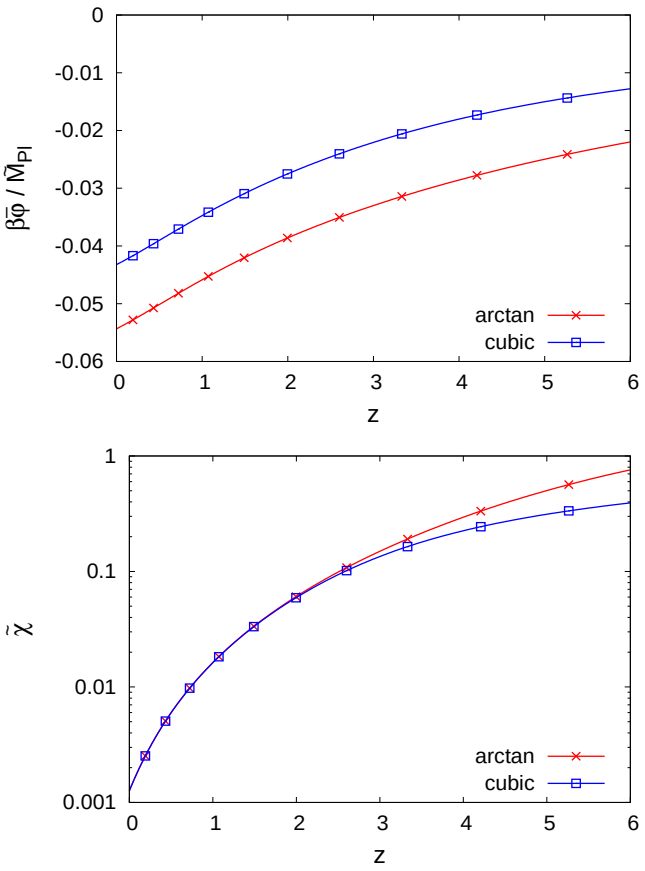

FIG. 4: *Upper panel:* background scalar field $\bar{\varphi}$ as a function of redshift. *Lower panel:* background kinetic term $\bar{\tilde{\chi}}$ as a function of redshift.

C. Modified gravitational potentials, gravitational slip and effective Newton's constant

As seen in Sec. III, both for the background quantities and the large-scale perturbative structures, the deviations from the Λ-CDM universe can be measured by the two coefficients $\epsilon_1(t)$ and $\epsilon_2(t)$, defined in Eqs.(46) and (25). In particular, from Eqs.(41) and (44) the two gravitational potentials Φ and Ψ of the Jordan-frame metric (40) read for large-scale unscreened structures as

$$\Phi = (1 + \epsilon_1)\Psi_{\rm N}, \quad \Psi = (1 - \epsilon_1)\Psi_{\rm N}, \tag{79}$$

and the normalized gravitational slip writes as

$$\eta \equiv \frac{\Psi - \Phi}{\Psi + \Phi} = -\epsilon_1. \tag{80}$$

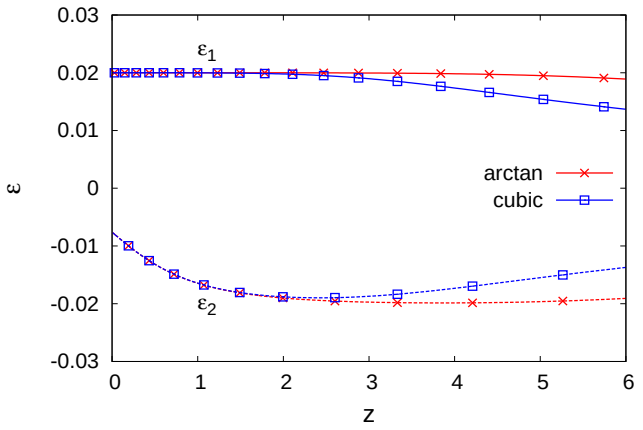

FIG. 5: Coefficients ϵ_1 and ϵ_2, defined in Eqs.(46) and (25) for the K-mouflage models, as functions of redshift.

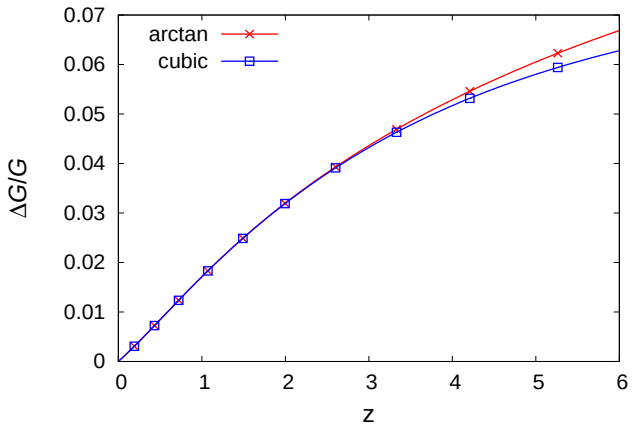

FIG. 6: Relative drift with redshift of the effective Newton constant for the K-mouflage models.

We show both coefficients $\epsilon_1(t)$ and $\epsilon_2(t)$ in Fig. 5. We can see that they are of order 2% at low z. Again, as can be seen from Eq.(46), this amplitude is set by our choice $\beta = 0.1$ (to satisfy observational constraints) as $\bar{K}' \simeq 1$ at low z and deviations from the Λ-CDM reference then scale as β^2. This also sets the amplitude of the gravitational slip η. At high z the coefficients $\epsilon_i(t)$ go to zero, as $\bar{K}'$ goes to infinity and we enter a cosmological nonlinear screening regime that also ensures that the dark-energy component becomes subdominant at early times. This decrease of ϵ_i appears faster for the cubic model, because of its stronger growth of $K'(\chi)$ at large positive χ. As noticed above, this means that departures from the Λ-CDM scenario are greater for the arctan model than for the cubic model (with our choice of parameters).

The Jordan-frame coefficient ϵ_1 is always positive and the gravitational slip η defined in Eq.(80) is negative. From Eq.(25) the coefficient ϵ_2 also reads as

$$\epsilon_2(t) = \frac{\beta(t)}{\tilde{M}_{\rm Pl}} \frac{\mathrm{d}\bar{\varphi}}{\mathrm{d}\ln a} = \frac{\beta(t)}{\tilde{M}_{\rm Pl} H(t)} \frac{\mathrm{d}\bar{\varphi}}{\mathrm{d}t}, \tag{81}$$

which is negative from Eq.(35) and of order $\beta^2/\bar{K}'$.

In Fig. 6 we show the evolution with redshift of the effective Newton constant, defined from Eq.(77) as

$$\mathcal{G}(t) = \mathcal{G}_0 \frac{\bar{A}^2(t)}{\bar{A}_0^2}. \tag{82}$$

Because of the dependence of the effective Newton coupling strength on the background value of the scalar field, $\mathcal{G}$ is a few percent higher at $z \sim 6$ than today.

D. Linear theory

In Fig. 7 we show the relative deviation, $D_+/D_{+\Lambda-\rm CDM} - 1$, of the linear growing mode, obtained by solving equation (55), from the Λ-CDM

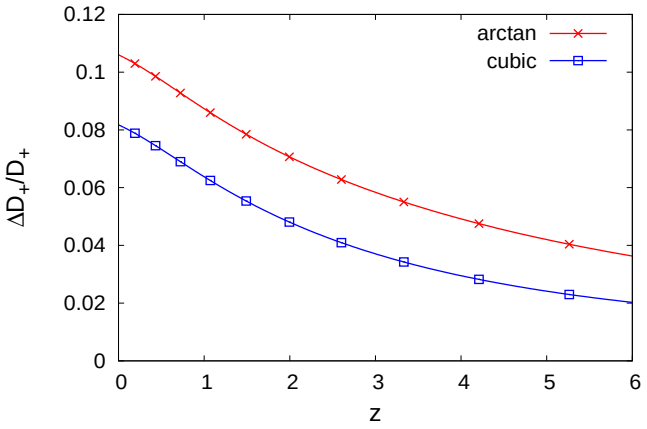

FIG. 7: Relative deviation, $D_+/D_{+\Lambda-\rm CDM} - 1$, of the linear growing mode D_+ from the Λ-CDM reference.

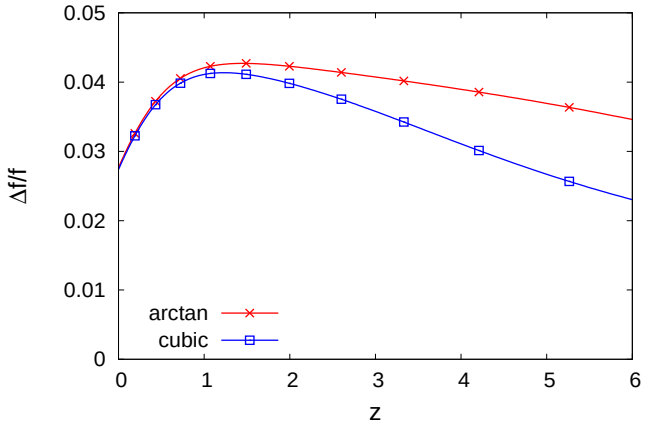

FIG. 8: Relative deviation, $f/f_{\Lambda\rm CDM} - 1$, of the linear growth rate, $f(z) = \mathrm{d}\ln D_+/\mathrm{d}\ln a$, from the Λ-CDM reference.

reference case, and the linear growth rates $f(z)$. Again, the relative deviation of the growing mode is greater for the arctan model (71) than for the cubic model (74), because of the lower value of $\bar{K}'$ over relevant redshifts, see Eq.(46) for the coefficient ϵ_1 that modifies the linear growing mode equation (55). All linear growing modes converge at high redshift, despite the slightly different Planck masses and Hubble expansion rates. Indeed, far in the early matter-dominated era we recover an Einstein-de Sitter cosmology and the Hubble term in the parenthesis in Eq.(55) converges to $H^{-2}\mathrm{d}H/\mathrm{d}t \to -3/2$. Moreover, the factor ϵ_1 goes to zero because of the nonlinear K-mouflage screening mechanism, see Eq.(46), as at high redshift $\bar{\chi}$ and $\bar{K}'$ become large. This large-K' behavior is also required to ensure that the background dark-energy density becomes subdominant.

We show the relative deviation of the linear growth rates $f(z)$ in Fig. 8. Overall, $f(z)$ is greater for the K-mouflage scenarios, in agreement with the higher value of the linear growing mode shown in Fig. 7. The deviation is again of the order of a few percent. The deviation for the linear modes D_+ shown in Fig. 7 could reach 10% at $z = 0$ because of the cumulative effect due to the integration over time. The growth rates $f(z)$ converge to unity at high redshift but we can see that there remains a noticeable difference between the K-mouflage models and the Λ-CDM reference up to $z \sim 6$.

This rather slow decrease of the deviations from the Λ-CDM reference at higher redshift is a characteristic signature of K-mouflage models, as many other modified-gravity models, such as $f(R)$ theories, lead to a faster convergence to the Λ-CDM scenario at $z \gtrsim 2$. This is related to the fact that in the linear sub-horizon regime the K-mouflage effects are scale independent, as the factors $\epsilon_1(t)$ and $\epsilon_2(t)$ only depend on time. In contrast, in $f(R)$ theories or Dilaton models, the factor $\epsilon(k,t)$ that appears in the modified Euler or Poisson equations, or in the evolution equation for the linear density modes, takes the form $\epsilon(k,t) \propto \beta^2 k^2/(a^2m^2+k^2)$, with a characteristic physical scale $2\pi/m$ beyond which the theory converges to General Relativity. At high redshift this scale typically goes to zero, so that at a fixed physical (or also comoving) scale, deviations from the Λ-CDM scenario vanish because the coupling β decreases or one enters the unmodified regime beyond $2\pi/m$. In the K-mouflage models that we consider in this paper, because there is no such characteristic scale the convergence to General Relativity is only due to the vanishing of the effective coupling strength β^2/K', with β being constant (in our case) and K' increasing at high z because of the nonlinear K-mouflage mechanism itself. However, this decrease of β^2/K' at high z is rather slow for generic kinetic functions $K(\chi)$, as seen from the curve obtained for $\epsilon_1(t)$ in Fig. 5 for the simple cubic model.

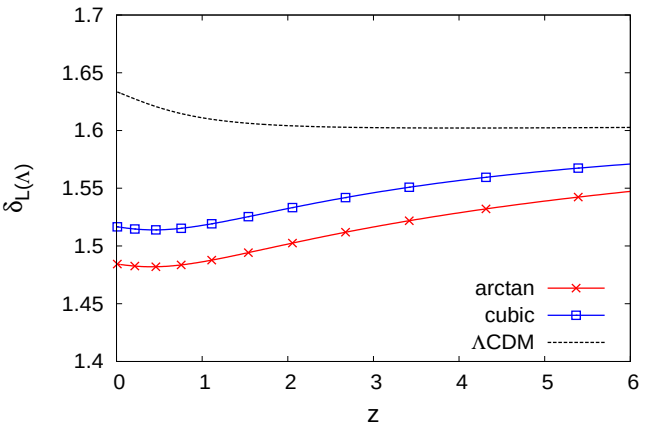

FIG. 9: Linear density contrast threshold $\delta_{L(\Lambda)}$ associated with the nonlinear density contrast $\Delta_c = 200$ with respect to the critical density $\rho_{\rm crit}$, for the K-mouflage models and the Λ-CDM reference.

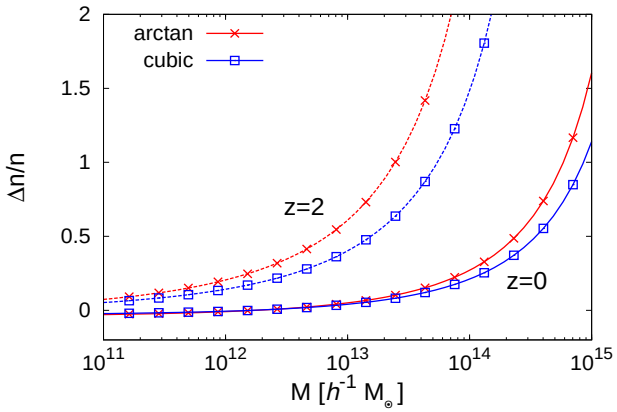

FIG. 10: Relative deviation, $n(M)/n_{\Lambda-\rm CDM}(M) - 1$, of the halo mass function of the K-mouflage models from the Λ-CDM reference, at $z = 0$ (solid lines) and $z = 2$ (dashed lines). Halos are defined by the density contrast $\Delta_c = 200$ with respect to the critical density.

E. Halo mass function

Solving the spherical collapse equation (60), we can compute the linear density contrast threshold $\delta_L(z)$ that corresponds to a nonlinear density contrast of $\delta[\delta_L] = \Delta_{\rm m}$, where $\Delta_{\rm m}$ is the nonlinear threshold that we choose to define halos. As discussed in [8], we are not interested in $\delta_L(z)$ at the observation redshift, because it is not an observable quantity. Instead, we wish to evaluate the linear threshold $\delta_{L_{\rm i}}$, at a given high redshift $z_{\rm i}$, that is required to produce at later time z a nonlinear density contrast $\Delta_{\rm m}$. In other words, we want to estimate the initial density fluctuation associated with a given nonlinear density contrast at the observed redshift. To avoid

the introduction of an arbitrary high redshift $z_{\rm i}$, following what it is done in [8] and usual practice, we translate all the initial thresholds $\delta_{L_{\rm i}}$ to redshift z by multiplying them by $D_{+\Lambda-{\rm CDM}}(z)/D_{+\Lambda-{\rm CDM}}(z_{\rm i})$ [instead of using $D_+(z)/D_+(z_{\rm i})$, i.e. the linear growing mode associated with each K-mouflage scenario], and we denote this quantity the linear density contrast threshold $\delta_{L(\Lambda)}$. This common multiplicative factor enables a meaningful comparison between the different scenarios.

In Fig.9 we display $\delta_{L(\Lambda)}$ when we define halos by a constant density contrast threshold $\Delta_c = 200$ with respect to the critical density $\rho_{\rm crit}$. This corresponds to a density contrast with respect to the mean density $\bar{\rho}$ of $\Delta_{\rm m} = \Delta_c/\Omega_{\rm m}(z)$. We choose a constant Δ_c rather than $\Delta_{\rm m}$ because observational cluster surveys usually define cluster halos by a constant overdensity with respect to the critical density $\rho_{\rm crit}$. At high redshift both definitions coincide, as $\Omega_{\rm m} \to 1$, while at low redshift or far in the dark-energy dominated era one can argue that Δ_c makes more physical sense. Indeed, during an exponential acceleration phase the growth of large-scale structures freezes out and one obtains isolated halos among increasingly large voids. Then, the mean universe density $\bar{\rho}$ decreases as a^{-3}, following the dilution due to the expansion, and it does not correspond to the typical density of halos (nor voids). In contrast, we can assume that the isolated halos keep a roughly constant physical radius and density, like the critical density $\rho_{\rm crit}$ (in an exponential phase where the Hubble rate is constant), so that it is more meaningful to express halo densities in terms of $\rho_{\rm crit}$.

Both K-mouflage models accelerate the growth of large-scale structures as compared with the Λ-CDM reference, as seen from the linear growing modes of Fig. 7. Therefore, we find in Fig.9 that a smaller linear density contrast is required to reach the same nonlinear overdensity of 200 (with respect to the critical density). Again, the deviation from the Λ-CDM prediction is greater for the arctan model (71).

From the linear threshold displayed in Fig.9 we obtain the halo mass function as in Eq.(61) (note that $\nu = \delta_L/\sigma = \delta_{L(\Lambda)}/\sigma_{(\Lambda)} = \delta_{L{\rm i}}/\sigma_{\rm i}$). In Fig.10 we show the relative deviation $n(M)/n_{\Lambda-{\rm CDM}}(M) - 1$ of the halo mass function from the Λ-CDM reference case, at $z = 0$ and $z = 2$. As for the case of $\delta_{L(\Lambda)}$, since the scalar field enhances gravitational clustering we find that the mass functions for the two K-mouflage models are higher than the Λ-CDM reference in the high-mass tail, with the greater deviation obtained for the arctan model (71). As usual, the deviation increases at high mass because the exponential falloff amplifies the sensitivity to slight departures of the growth of structures. (The deviation becomes slightly negative at low mass because all mass functions obey the same normalization to unity: there cannot be more matter in halos than the matter content of the universe.)

At fixed mass, $M \sim 10^{14} h^{-1} M_\odot$, the deviation from the Λ-CDM reference is greater at $z = 2$ than at $z = 0$, despite the difference in linear density thresholds being lower, as seen in Fig. 9. This is because at fixed mass we are further into the rare high-mass tail, which amplifies the dependence on the linear density threshold and more than compensates the slow convergence between the K-mouflage and Λ-CDM thresholds.

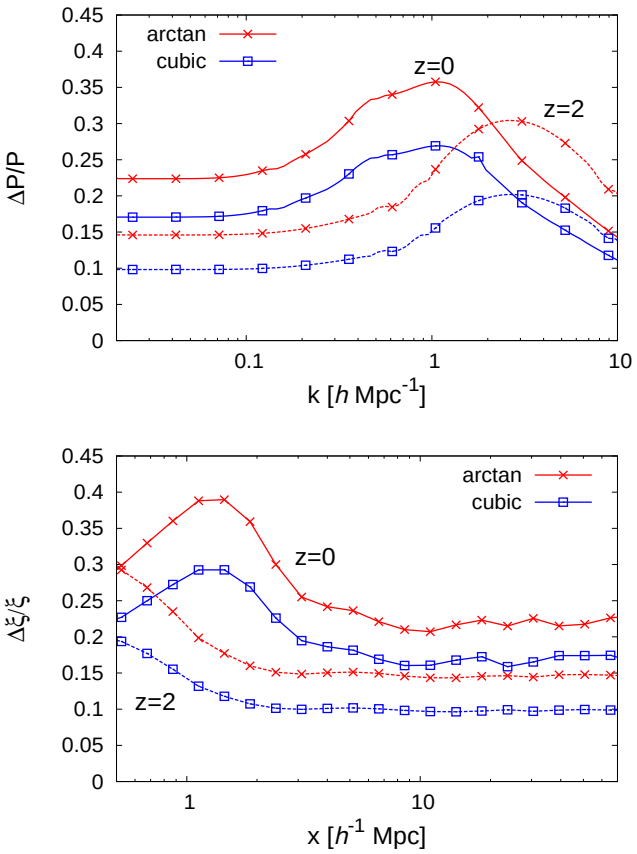

FIG. 11: *Upper panel:* relative deviation of the matter density power spectrum from the Λ-CDM reference, at $z = 0$ (solid lines) and $z = 2$ (dashed lines), for the K-mouflage models. *Lower panel:* relative deviation of the matter density correlation function from the Λ-CDM reference.

F. Matter density power spectrum and correlation function

We show in Fig. 11 the matter density power spectra and correlation functions at $z = 0$ and $z = 2$. The computation of this power spectrum $P(k)$ combines perturbation theory up to one-loop order with a halo model, as described in [8] in the case of Einstein-frame studies and following the approach introduced in [27]. The two-point correlation function $\xi(x)$ is obtained from the Fourier transform of the power spectrum. On large scales we obtain the same constant relative deviation for the power spectra and the correlation functions, as the linear growing modes $D_+(t)$ are scale independent in both

K-mouflage and Λ-CDM cosmologies (much below the horizon). This deviation of 20% is consistent with the deviation of 10% obtained for the linear growing modes in Fig. 7. The deviation from the Λ-CDM reference grows on mildly nonlinear scales, as nonlinearities amplify the effects of the fifth force. This is related to the increase of the large-mass tail of the halo mass function shown in Fig. 10, because on these scales the power spectrum and the correlation function probe the formation of massive halos, as can be clearly seen in a halo model approach. The deviation decreases on smaller scales because the power spectrum now probes the inner regions of halos and we assume similar NFW profiles [26] for all cosmologies (but this regime shows a greater theoretical inaccuracy and numerical simulations would be need to measure the impact of the modified gravity on small highly nonlinear scales and halo profiles). However, in the nonlinear range shown in Fig. 11, the impact of changes to the mass function is greater than that of halo profiles, see also Ref. [28] for a detailed study of these various contributions.

The deviation from the Λ-CDM reference slowly decreases at high z, as the fifth force mediated by the scalar field becomes negligible (as seen from the vanishing of the key factor $\beta^2/\bar{K}'$ as $\bar{K}' \to \infty$). This decrease of the deviations of large-scale clustering from the Λ-CDM reference is slower than what is found in many other modified-gravity scenarios, such as the $f(R)$ theories, and is characteristic of these K-mouflage models.

V. CLUSTERS OF GALAXIES

To go beyond background quantities and the large-scale perturbative regime, we investigate in this section the impact of K-mouflage scenarios on the largest collapsed structures that we observe, that is, clusters of galaxies. This provides another probe of modified-gravity models, which is complementary with background and perturbative studies, as it corresponds to the nonlinear regime of the matter density field and to the well-defined objects measured in actual surveys.

For our purposes, clusters present two advantages as compared with galaxies. First, they are unscreened objects [8], so that the impact of the modification to gravity is very simple and corresponds to a time-dependent effective Newton constant (we shall check that this holds down to the cluster cores in Sec. V B below). Therefore, one does not expect dramatic qualitative changes from the Λ-CDM case, and the same semi-quantitative models can be applied to both K-mouflage and Λ-CDM cosmologies. This is also illustrated by the symmetry described in Sec. III G, which shows that in this unscreened regime, from the point of view of nonlinear gravitational clustering, the Λ-CDM cosmology, quintessence models, and K-mouflage scenarios, belong to the same class. They obey the same equations of motion (67)-(68), with only slightly different time-dependent functions $\kappa(t)$ from Eq.(70). Second, at first order clusters can be described by simple physical laws, such as hydrostatic equilibrium for the gas profile and Bremsstrahlung emission for the X-ray luminosity, giving rise to the so-called cluster "scaling laws" [29]. This is especially true for the most massive clusters that we focus on.

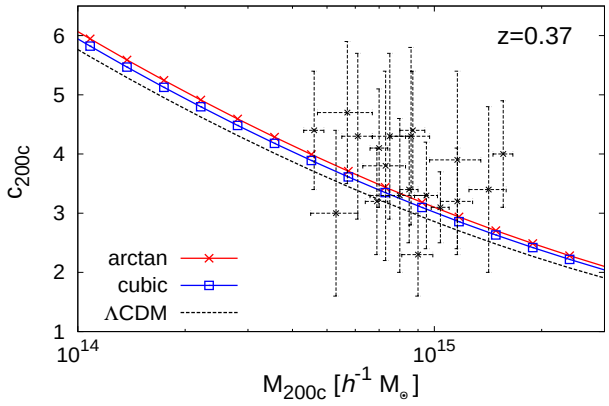

FIG. 12: Mass-concentration relation for NFW halos, for the K-mouflage models and the Λ-CDM reference, at $z = 0.37$. The black points (with their error bars) are observational measures taken from [30].

In contrast, galaxies probe the transition from the unscreened to screened regimes and also involve many complex astrophysical phenomena, such as cooling processes, star formation, supernovae and AGN winds and feedback. Therefore, although they would be very interesting probes they are much more difficult to model, both for the modified-gravity sector and for the usual galaxy formation processes that also appear in the Λ-CDM cosmology.

In this paper, our goal is to estimate the magnitude of the impact of K-mouflage models on clusters of galaxies rather than building a very accurate description of clusters. Therefore, we consider the simplest possible modelling of clusters with only few physical parameters. This may not provide the highest-accuracy cluster model, but we can expect that it captures the main physical processes and provides a robust estimate of the impact of modifications to gravity. Moreover, we check that our predictions show a reasonable agreement with observations.

A. Halo density profiles

To study the effects of K-mouflage scenarios on clusters of galaxies we need their dark matter profile. Because in the unscreened regime gravitational clustering proceeds in the same fashion in K-mouflage and Λ-CDM cosmologies, as described in Sec. III G, we assume in all cases

NFW profiles [26],

$$\rho_{\rm DM}(r) = \frac{\rho_s}{(r/r_s)(1+r/r_s)^2}. \tag{83}$$

This profile is characterized by a scaling radius and density, respectively r_s and ρ_s, which can be expressed in terms of the concentration parameter $c = R_{\Delta_c}/r_s$. Here R_{Δ_c} is the radius such that the mean density within R_{Δ_c} is Δ_c times the critical density, $\rho(< R_{\Delta_c}) = \Delta_c \rho_{\rm crit}$, as we again define the extension of the halos by an overdensity threshold with respect to the critical density. From the definition of c, is possible to express ρ_s as

$$\rho_s = \rho_{\rm crit} \frac{\Delta_c}{3} \frac{c^3}{\ln(1+c) - c/(1+c)}, \tag{84}$$

which can be inverted to give c as a function of ρ_s.

To consider the effects of the presence of the scalar field on the shape of the dark matter profile we consider a simple model for the halo concentration. We assume that halos of mass M typically form at a redshift $z_{\rm f}(M)$ determined by

$$\sigma(q, z_{\rm f}) = \sigma_{\rm f}, \tag{85}$$

where $q = (3M/4\pi\bar{\rho}_0)^{1/3}$ is the halo Lagrangian radius and $\sigma_{\rm f}$ is a free parameter, and that the density of the newly-formed halo is proportional to $\rho_{\rm crit}(z_{\rm f})$,

$$\rho_s(M) = \Delta_{\rm f}\, \rho_{\rm crit}(z_{\rm f}), \tag{86}$$

with $\Delta_{\rm f}$ a second free parameter. Equation (85) means that halos of a given mass typically form when density fluctuations at this mass scale reach the nonlinear regime, while equation (86) assumes that the core of the cluster keeps a roughly constant density after its formation, which is set by the critical density at the formation time. As discussed in Sec. IV E, we choose to rescale ρ_s in terms of the critical density rather than the mean density at redshift $z_{\rm f}$ because the former is more physical at late times (whereas they coincide at high redshift) and it also corresponds to our definition of halos. Next, using equation (84), we compute $c(M)$ and we define the dark matter density profile using (83).

In Fig. 12 we display the mass-concentration relation obtained with the choice of parameters $\sigma_{\rm f} = 0.2$ and $\Delta_{\rm f} = 500$ (halos are again defined by $\Delta_c = 200$). As is well known [31], the concentration c (and the scaling density ρ_s) is larger for smaller mass, because in hierarchical scenarios smaller mass scales turned nonlinear at higher redshift when the critical (and the mean) density of the Universe was greater. This is of course consistent with our model (85)-(86). We compare these results with the mass-concentration relation obtained by [30], from the analysis of 19 X-ray selected galaxy clusters from the Cluster Lensing and Supernova Survey with Hubble (CLASH), with a mean redshift $z \simeq 0.37$. We can see that reasonable choices of the parameters $\sigma_{\rm f}$ and $\Delta_{\rm f}$ (we naturally expect $\sigma_{\rm f} \lesssim 1$ and $\Delta_{\rm f} \gtrsim 200$) allow us to obtain a reasonable match to observations. This suggests that this simple modelling captures the main features of the gravitational formation of halos. Therefore, we do not consider here more sophisticated models, which involve the past accretion history and merging trees of virialized halos. These could provide more accurate modelling, at the price of additional complexity (and often additional parameters), but it is not clear if their estimate of the dependence on the underlying gravity theory would be much more accurate. Such studies are left for future works, where N-body simulations would be needed to check detailed models.

As expected, we find a small increase of the concentration $c(M)$ in the K-mouflage models, as compared with the Λ-CDM reference. This is due to the faster growth of gravitational clustering, which implies a slightly greater scaling density $\rho_s(M)$. However, we can see that the effect is rather modest.

B. Clusters are not screened

As noticed in [7, 8], clusters are unscreened, and the Klein-Gordon equation (23) can be kept at the linear level over the fluctuations of the scalar field, as in Eq.(43). In this section we check that this property extends far inside the cluster profile.

In the small-scale static limit, which corresponds for instance to high-density astrophysical objects, the Klein-Gordon equation (A3) becomes

$$\nabla_{\mathbf{r}} \cdot (\nabla_{\mathbf{r}} \varphi\, K') = \frac{\beta \bar{A}}{c^2 M_{\rm Pl}} \rho, \tag{87}$$

where $\mathbf{r}$ is the Jordan-frame physical coordinate and we assumed $\delta\rho \simeq \rho$ (i.e., $\delta \gg 1$). As compared with Eq.(43), here we do not make the approximation $K' \simeq \bar{K}'$. Instead we consider the small-scale regime where $\tilde{\chi} \simeq \delta\tilde{\chi} < 0$. For a spherically symmetric halo, using the Stokes theorem this gives

$$\frac{{\rm d}\varphi}{{\rm d}r} K' = \frac{\beta \bar{A} M(r)}{c^2 M_{\rm Pl} 4\pi r^2}. \tag{88}$$

As in [7, 8, 12] (but in Jordan-frame coordinates), defining the "K-mouflage screening radius" R_K by

$$R_K(M) = \left(\frac{\beta \bar{A}^2 M}{4\pi c M_{\rm Pl} \mathcal{M}^2} \right)^{1/2}, \tag{89}$$

where $M = M(R)$ is the total mass of the object of radius R, and introducing the rescaled dimensionless variables $x = r/R_K$, $m(x) = M(< r)/M$, $\phi(x) = \varphi(r)/\varphi_K$, with $\varphi_K = \mathcal{M}^2 R_K/c\bar{A}$, the integrated Klein-Gordon equation (88) reads as

$$\frac{{\rm d}\phi}{{\rm d}x} K' = \frac{m(x)}{x^2}, \quad \text{with} \quad \tilde{\chi} = -\frac{1}{2}\left(\frac{{\rm d}\phi}{{\rm d}x}\right)^2. \tag{90}$$

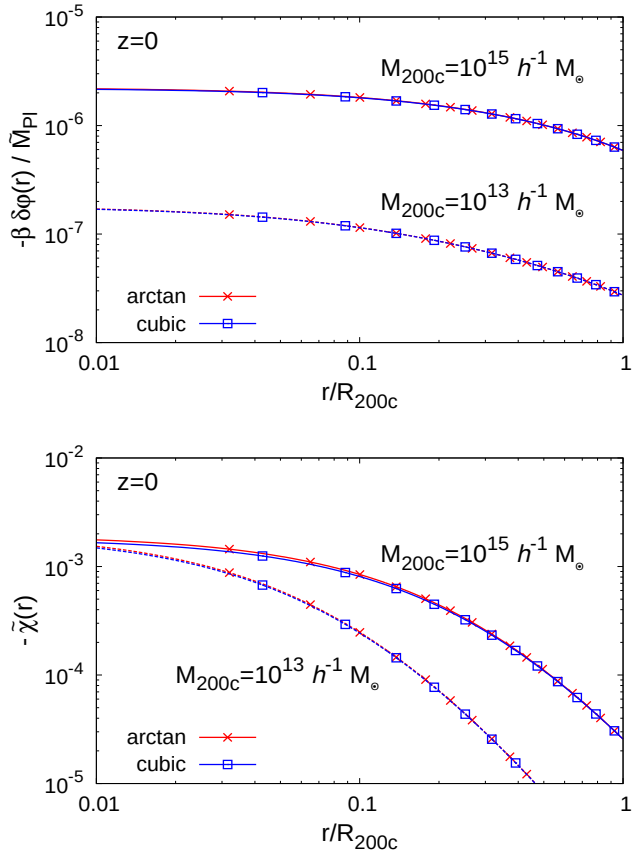

FIG. 13: *Upper panel:* scalar-field radial profile, $\delta\varphi(r) = \varphi(r) - \bar{\varphi}$, for halos of mass $10^{15}h^{-1}M_\odot$ (upper solid lines) and $10^{13}h^{-1}M_\odot$ (lower dashed lines). The scalar-field fluctuation is negative as the scalar field φ is minimum at the center of the halo. *Lower panel:* radial profile of the "kinetic energy" $-\tilde{\chi}(r)$ of the scalar field, for halos of mass $10^{15}h^{-1}M_\odot$ (upper solid lines) and $10^{13}h^{-1}M_\odot$ (lower dashed lines). Here $\tilde{\chi} < 0$ because we consider the static limit, which is dominated by spatial gradients. The arctan and cubic K-mouflage models give almost identical results in this figure.

As pointed out in [7], in the small-scale static regime we have $\tilde{\chi} < 0$ whereas the cosmological background value satisfies $\bar{\tilde{\chi}} > 0$. Using that $\mathcal{M}^4 \sim \bar{\rho}_{\rm de0}$ is roughly the dark-energy density today and that $\bar{A} \sim 1$, we obtain

$$R_K(M) \simeq \sqrt{\frac{\beta M}{1M_\odot}} 3470\,{\rm a.u.} \simeq \sqrt{\frac{\beta M}{10^{14}M_\odot}} 0.12\,h^{-1}{\rm Mpc}. \tag{91}$$

The first equality shows that the Solar System is screened by the Sun, which allows these K-mouflage scenarios to satisfy Solar System constraints [12]. On the other hand, for $\beta = 0.1$ the K-mouflage screening radius of a cluster of mass $10^{14}M_\odot$ is $R_K \simeq 0.04h^{-1}$Mpc. This is much smaller than the radius of the cluster, which means that most of the cluster is unscreened. Moreover, as we move inside the halo the enclosed mass $M(< r)$ decreases, which further delays the onset of K-mouflage screening. When $|\tilde{\chi}| \ll 1$ we have $K' \simeq 1$ and we obtain

$$|\tilde{\chi}| \ll 1 : \quad \tilde{\chi}(r) \simeq -\frac{m(x)^2}{2x^4}, \tag{92}$$

which gives inside the halo

$$|\tilde{\chi}| \ll 1, \quad r < R : \quad \tilde{\chi}(r) \simeq -\frac{\rho_{\rm crit}}{6\mathcal{M}^4}\left(\beta\bar{A}^2\Delta_c(<r)\frac{Hr}{c}\right)^2. \tag{93}$$

We show the radial profiles of $-\tilde{\chi}(r)$ in the lower panel in Fig. 13, for $M = 10^{15}h^{-1}M_\odot$ and $10^{13}h^{-1}M_\odot$. In both cases we can check that $|\tilde{\chi}| \ll 1$ over the full halo profile [as seen from Eq.(92), $\tilde{\chi}(r)$ goes to a finite value at $r \to 0$ for NFW density profiles, because $\rho \propto 1/r$ and $m \propto x^2$ in the core]. This means that clusters are not screened and that we can use the background value $\bar{K}'$ for the kinetic function. In fact, at low z we also have $\bar{\tilde{\chi}} \ll 1$ and $\bar{K}' \simeq 1$, so that the kinetic function is dominated by the low-order terms in the expansion (7) and the results are not very sensitive to the precise nonlinear form of $K(\tilde{\chi})$. Then, the Klein-Gordon equation can be linearized in the scalar field as in Eq.(43) and the gravitational potential Φ that governs the dynamics of matter is again given by Eq.(45).

From the kinetic factor $\tilde{\chi}(r)$ we can obtain the radial profile of the scalar field, $\varphi(r)$, by integrating ${\rm d}\phi/{\rm d}x = \sqrt{-2\tilde{\chi}}$ and using $\varphi = \varphi_K\phi$. The boundary condition is $\varphi \to \bar{\varphi}$ at infinity. We show the radial profile of the fluctuation $\delta\varphi = \varphi - \bar{\varphi}$ in the lower panel in Fig. 13. We can check from the comparison with Fig. 4 that $|\delta\varphi| \ll |\bar{\varphi}|$, in agreement with the scaling $\delta\varphi/\bar{\varphi} \sim (aH/ck)^2\delta\rho/\bar{\rho}$ obtained from Eq.(A35) and $\bar{\varphi}/\tilde{M}_{\rm Pl} \sim \beta/\bar{K}'$. In particular, this explicitly shows that the coupling function $A(\varphi)$ remains dominated by its low-order terms in the expansion (8), both for the background and for large-scale structures such as clusters of galaxies.

The magnitude of $\delta\varphi$ can also be read from the modified Poisson equations (41). In realistic models the fifth force should not have a magnitude greater than the Newtonian force, which implies $|\delta A/\bar{A}| \simeq |\beta\delta\varphi/\tilde{M}_{\rm Pl}| \lesssim |\Psi_{\rm N}|$, whence $|\beta\delta\varphi/\tilde{M}_{\rm Pl}| \lesssim 10^{-5}$.

C. Impact of nonlinear substructures

The Klein-Gordon equation (87) that determines the scalar field φ is nonlinear, because of the factor $K'(\tilde{\chi})$. This means that substructures could have a strong impact on the solution $\varphi(\mathbf{r})$ as there is no longer a linear superposition property and the solution obtained for the averaged halo profile is not identical to the average of the exact solutions obtained by taking into account substructures. In this section, we check that this nonlinearity does not play a significant role and does not invalidate our approach described in Sec. V B.

First, we note that for an object that is exactly spherically symmetric, the integrated Klein-Gordon equation

(88) holds and the scalar-field profile only depends on the integrated mass $M(r)$ within radius r. This smoothes out radial substructures. However, in practice clusters are not exactly spherically symmetric, and individual cluster galaxies also break any overall spherical symmetry. We have seen in Sec. V B that clusters are unscreened as the kinetic factor, $\tilde{\chi}_{\rm clus}(r)$, associated with the mean cluster density profile (83), is much smaller than unity. Then, if galactic halos only form a small fraction of the total cluster volume, throughout most of the cluster volume we can linearize Eq.(87), as in Eq.(43), which gives

$$\text{unscreened region:} \quad \nabla^2_{\mathbf{r}}\varphi = \frac{\beta \bar{A}}{\bar{K}' c^2 M_{\rm Pl}}\rho, \qquad (94)$$

where $\bar{K}'$ is the background value, with $\bar{K}' \simeq 1$ at low z. This equation breaks down around each cluster galaxy, where the high matter density, which is much greater than the NFW mean density $\rho_{\rm DM}(r)$ of Eq.(83) at that radius, makes the scalar field enter the nonlinear screening regime. Thus, around each galaxy "i", $i = 1, .., N_{\rm gal}$, we must cut a patch V_{Ki} where the equation (94) must be replaced by the fully nonlinear equation (87). By definition, the volume V_{Ki} is given by the K-mouflage radius R_{Ki} of the galaxy. In practice, if $R_{Ki} \ll R_{\rm clus}$, we can build an approximate solution by patching the solutions within each galaxy volume V_{Ki} with the global solution (94) that holds in between galaxies. Around each galaxy, using an approximate spherical symmetry around the galaxy center, we obtain the local profile by solving Eq.(88), where M is replaced by the galaxy mass $m_{\rm gal}(r)$, and the boundary condition at R_{Ki} is approximated as a constant obtained from the global solution (94).

This scenario holds provided the regions V_{Ki} do not extend far beyond the galaxy volumes V_i (defined for instance by their stellar content or by the region where matter is gravitationally bound to the galaxy) and do not cover most of the cluster volume. From Eq.(89) we have $R_K(m_{\rm gal}) \propto m_{\rm gal}^{1/2}$. Defining the mass function $n(m)\mathrm{d}m$ of the cluster galaxies, the total volume built by the nonlinear regions V_{Ki} reads as

$$V_{K\rm gal} = \int_0^\infty \mathrm{d}m \, \frac{\mathrm{d}n}{\mathrm{d}m} V_K(m) \propto \int_0^\infty \mathrm{d}m \, \frac{\mathrm{d}n}{\mathrm{d}m} m^{3/2}. \quad (95)$$

The mass function of the cluster galaxies or of dark matter subhalos is typically a power law at law mass with an exponential cutoff at high mass [32]. In any case, the integral $\int \mathrm{d}m(\mathrm{d}n/\mathrm{d}m)m = M_{\rm gal}$ is necessarily finite and equal to the total mass associated with the galaxies, which is smaller than the total cluster mass. Therefore, the integral (95) converges at low mass and is dominated by the galaxies around the knee of the galaxy multiplicity function, which typically corresponds to $M \sim 10^{12} M_\odot$ From Eq.(91) we have $R_K(10^{12} M_\odot) \simeq 4h^{-1}$kpc, with $\beta = 0.1$, which gives a volume fraction of the order of $(0.004)^3 \sim 5 \times 10^{-8}$. Even if we have ~ 20 such galaxies in the cluster, this only makes a fraction of order 10^{-6} of the cluster volume.

Moreover, we can see that R_{Ki} is typically smaller than the actual radius R_i of the galaxy (by a factor of a few). In the Λ-CDM cosmology itself, the analysis of the hot gas that makes most of the intracluster medium and gives rise to the cluster X-ray luminosity (based on hydrostatic equilibrium and scaling laws) only applies outside of the cluster galaxies, where cooling and star formation processes play a major role. Therefore, the nonlinearities of the Klein-Gordon equation (87) do not bring further restrictions as compared with the standard Λ-CDM case, as they are "hidden" within the galaxies, and the impact of the fifth force on the intracluster medium can be obtained from the linearized equation (94) associated with the unscreened regime. They do not modify global properties either, such as the cluster correlation function, as the dynamics and formation of the clusters remain governed by the linearized Klein-Gordon equation (94).

D. Hydrostatic equilibrium

From equation (48), the equation of hydrostatic equilibrium for the gas density ρ_g and pressure p_g reads as

$$\nabla\Phi = \nabla\left(\Psi_{\rm N} + \frac{\beta c^2 \varphi}{\tilde{M}_{\rm Pl}}\right) = -\frac{\nabla p_g}{\rho_g}, \qquad (96)$$

where we used Eqs.(41) and (44). This explicitly shows how the pressure gradient is amplified, at fixed density profile, by the fifth force. Assuming spherical symmetry this leads to

$$\frac{\mathrm{d}p_g}{\mathrm{d}r} = -\rho_g(1+\epsilon_1)\frac{\mathrm{d}\Psi_{\rm N}}{\mathrm{d}r}, \qquad (97)$$

where we used the fact that clusters are unscreened, so that $K' \simeq \bar{K}'$ and the Klein-Gordon equation can again be linearized as in Eq.(94). In the Λ-CDM cosmology we simply have $\epsilon_1 = 0$. To obtain the gas profile from Eq.(97) we also need an equation of state that gives the pressure as a function of the gas density or temperature. We consider an isothermal gas with $p_g = \rho_g k_B \bar{T}_g/(\mu m_p)$, where k_B is Boltzmann's constant and μm_p is the mean molecular weight of the gas. This yields the gas density profile

$$\rho_g(r) \propto e^{-(1+\epsilon_1)\mu m_p \Psi_{\rm N}(r)/k_B \bar{T}_g}, \qquad (98)$$

where the Newtonian potential $\Psi_{\rm N}$ is fixed by the dark matter profile.

To evaluate $\bar{T}_g$ we assume that the gas temperature is proportional to the mean value of the dark matter "temperature", $T_{\rm DM}(r)$, which we define from the velocity dispersion $\sigma^2_{\rm D}(r)$ as

$$k_B T_{\rm DM}(r) = \mu m_p \sigma^2_{\rm DM}(r). \qquad (99)$$

The dark matter being collisionless it is not described by a thermodynamical temperature. However, we can expect the virialization processes associated with the formation of the halo to scale in the same fashion for the

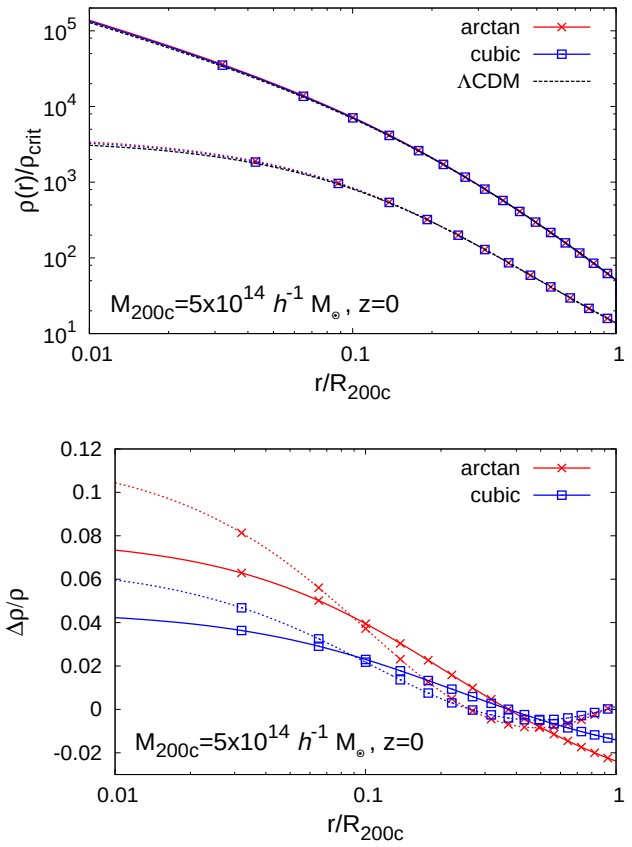

FIG. 14: *Upper panel:* density profiles for a cluster of mass $M_{200c} = 5 \times 10^{14} h^{-1} M_\odot$. The upper solid lines refer to the dark matter density profiles and the lower dotted lines to the gas density profiles. The K-mouflage models and the Λ-CDM reference cannot be distinguished in this figure. *Lower panel:* relative deviation from the Λ-CDM reference of the dark matter (solid lines) and gas (dotted lines) density profiles.

dark matter, as measured by its velocity dispersion, and for the gas, as measured by its temperature. In particular, the dark matter velocity dispersion obeys the Jeans equation, which can be written at equilibrium as [33]

$$\frac{1}{\rho_{\rm DM}} \frac{{\rm d}[\rho_{\rm DM}\sigma^2_{\rm DM}]}{{\rm d}r} = -\frac{{\rm d}\Phi}{{\rm d}r} = -(1+\epsilon_1)\frac{{\rm d}\Psi_{\rm N}}{{\rm d}r}. \qquad (100)$$

For a given dark matter halo profile, set by the NFW profile (83) and concentration parameter $c(M)$, the Jeans equation (100) determines the velocity dispersion profile $\sigma^2_{\rm DM}(r)$, whence the effective dark matter temperature $T_{\rm DM}(r)$ defined in Eq.(99). Then, we set the gas temperature $\bar{T}_g$ as

$$\bar{T}_g = \frac{1}{\beta_g}\bar{T}_{\rm DM} = \frac{1}{\beta_g}\frac{\int {\rm d}r\, 4\pi r^2 \rho_{\rm DM}(r) T_{\rm DM}(r)}{\int {\rm d}r\, 4\pi r^2 \rho_{\rm DM}(r)}, \qquad (101)$$

where β_g is a free parameter that we fix to be equal to 0.6, which is of the same order as the values used in studies of clusters of galaxies [34]. In other words, we assume that the kinetic and thermal energies of the dark matter and the gas are proportional, because they are generated by the same process, the formation and virialization of the halo.

Finally, to fully specify the gas density profile (98) we normalize it as

$$M_g = \int_0^{R_{\Delta_c}} {\rm d}r\, 4\pi r^2 \rho_g(r) = \frac{\Omega_b}{\Omega_{\rm DM}} M_{\rm DM}. \qquad (102)$$

Thus, we consider that the baryon and dark matter mass fractions in clusters are given by the cosmological abundance. This assumes that there is no significant redistribution and segregation of matter on scales greater than cluster radii, which should be a reasonable approximation for massive clusters.

Therefore, in terms of the intracluster medium, the differences between the K-mouflage and Λ-CDM scenarios only arise through three effects, in our framework. First, the dark matter profiles (83) are slightly different because of the small change of the halo concentration shown in Fig. 12, which comes from the different growth rates of large-scale structures. Second, the equation of hydrostatic equilibrium (96) is modified by the factor $\epsilon_1(t)$, which corresponds to the amplification of gravity by the fifth force in the unscreened regime. This implies slightly greater pressure gradients for the gas. Third, the gas (and dark matter) temperature itself is also amplified by the same factor $(1+\epsilon_1)$, at a fixed dark matter profile, because it also arises from the gravitational collapse, see Eqs.(100) and (101). The second and third effects compensate in terms of the gas density profile, as the greater potential depth is balanced by the greater gas temperature, so that we can expect rather modest deviations between the different cosmological scenarios.

In Fig. 14, we show the dark matter and gas density profiles for a cluster of mass $M = 5 \times 10^{14} h^{-1} M_\odot$ at $z = 0$, for the K-mouflage models and the Λ-CDM reference. The presence of the scalar field makes the density profiles more compact, in agreement with Fig. 12. As expected, the deviations from the Λ-CDM reference are of the order of a few percent.

E. Scaling laws

From the gas density profile $\rho_g(r)$ and temperature $\bar{T}_g$, we obtain the X-ray cluster luminosity within radius R as [35]

$$L_X(<R) = 4\pi \epsilon_X(\bar{T}_g) \int_0^R n_g^2(r) r^2 {\rm d}r, \qquad (103)$$

where $n_g(r) = \rho_g(r)/\mu m_p$ is the cluster gas density and $\epsilon_X(T)$ is the X-ray emissivity, which can be expressed in

terms of the temperature as [32]

$$\epsilon_X(T) = 4.836\times10^{-24}\frac{4-2Y}{(4-Y)^2}\left(\frac{T}{1\mathrm{keV}}\right)^{1/2}\ \mathrm{erg.s^{-1}.cm^3} \tag{104}$$

Here Y is the Helium mass fraction, and $\mu = 2/(4-Y)$, $n_e/n_g = (2-Y)/(4-Y)$, $(n_H + 4n_{He})/n_g = 2/(4-Y)$, where we assume complete ionization. This applies to high temperatures of order 1 keV and above, where the X-ray emissivity is dominated by Bremsstrahlung. Equation (103), with the emissivity (104), gives the total bolometric luminosity. In practice, one measures the radiation from X-ray clusters within finite frequency bands. Therefore, we also define the luminosity within frequency bands, denoted for instance as bands "$A = [\nu_1^A, \nu_2^A]$", "$B = [\nu_1^B, \nu_2^B]$", .., by

$$L_{XA}(< R) = L_X(< R)\left(e^{-h\nu_1^A/k_B\bar{T}_g} - e^{-h\nu_2^A/k_B\bar{T}_g}\right). \tag{105}$$

Observational studies often measure the X-ray properties of galaxy clusters within a radius R_X that is smaller than R_{200c}, because the luminosity scales as the squared density [see Eq.(103)] so that inner high-density regions are easier to measure. A popular choice is the radius set by the density threshold $\Delta_c = 500$ with respect to the critical density. In the following, keeping our definition of halos by the threshold $\Delta_c = 200$ as in Figs. 10 and 12 - 14, we use the density profile obtained from Eq.(98) and displayed in Fig. 14 to compute X-ray properties within R_X defined by $\Delta_c = 500$ (hence $R_X < R_{\rm halo}$).

To avoid the complications due to the internal structures of the clusters (presence of massive galaxies in the center, importance of dissipative processes, cooling cores,...) and also to follow the observational procedures, we define a core radius $R_{\rm core}$ outside of which we evaluate the quantities of interest. As in many observational analyses, we simply define $R_{\rm core}$ as a fixed fraction of the cluster radius R_X (as defined by the threshold $\Delta_c = 500$ with respect to the critical density), with $R_{\rm core} = f_{\rm core}R_X$ and typically $f_{\rm core} \sim 0.15$. Then, we obtain for instance the luminosity in the outer cluster shells, between $R_{\rm core} < r < R_X$, as

$$L_{XA\ \mathrm{no-core}} = L_{XA}(< R_X) - L_{XA}(< R_{\rm core}). \tag{106}$$

In Figs. 15 and 16, we show, respectively, the $M_{500c} - T_{500c-nocore}$ and $T_{500c-nocore} - L_{XA-500c-nocore}$ relations compared to observations of clusters of galaxies in the X-ray, with the choice of parameter $f_{\rm core} = 0.15$ and the frequency "A band" [0.1 - 2.4] keV. For the $M-T$ relation we obtain a good agreement with observations while our prediction for the slope of the $T - L$ relation is too shallow. This is a well-known problem associated with a noticeable breakdown of the naive "scaling laws" for the X-ray luminosity, especially for small clusters [35]. This is usually explained by a decrease of the gas fraction and a greater importance of nonthermal effects, or departures from hydrostatic equilibrium, in small clusters. However, because our goal is only to estimate the magnitude of the effects due to modifications of gravity, we do not try to build a more accurate and more complex model in this paper. Moreover, our simple model is sufficient to recover the typical X-ray luminosity in the range $4 < T < 15$ keV, which corresponds to massive bright clusters.

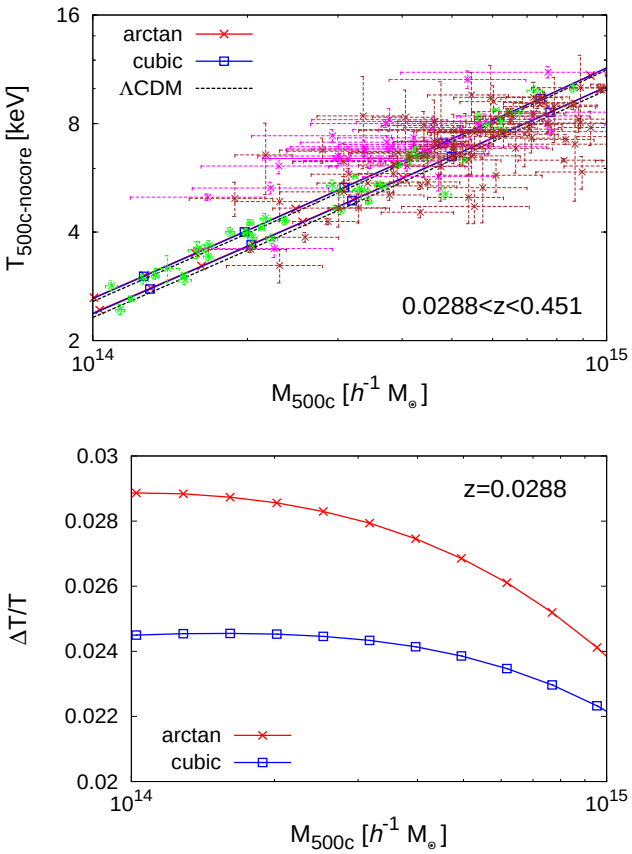

FIG. 15: *Upper panel:* mass-temperature relation for the K-mouflage models and the Λ-CDM reference, at $z = 0.0288$ (lower curves) and $z = 0.451$ (upper curves). The data points are taken from observations made by [36] (in green), [37] (in magenta) and [38] (in brown), with clusters in the redshift range $0.0288 \leq z \leq 0.451$. *Lower panel:* relative deviation of the cluster mass-temperature relation from the Λ-CDM reference, at $z = 0.0288$.

At fixed mass, the temperature in the K-mouflage scenarios is greater than in the Λ-CDM reference by about 2%. This is mostly set by the factor ϵ_1, which is about 2% as seen in Fig. 5. Indeed, from Eq.(100) we can see that at a fixed dark matter density profile the fifth-force enhancement of gravity by the factor $(1+\epsilon_1)$ yields an increase of the dark matter velocity dispersion and of the gas temperature by the same factor. The small deviations from this 2% value, which depend on mass, that appear in Fig. 15 correspond to the small changes of the dark matter profile through the modification of the concentration parameter shown in Fig. 12.

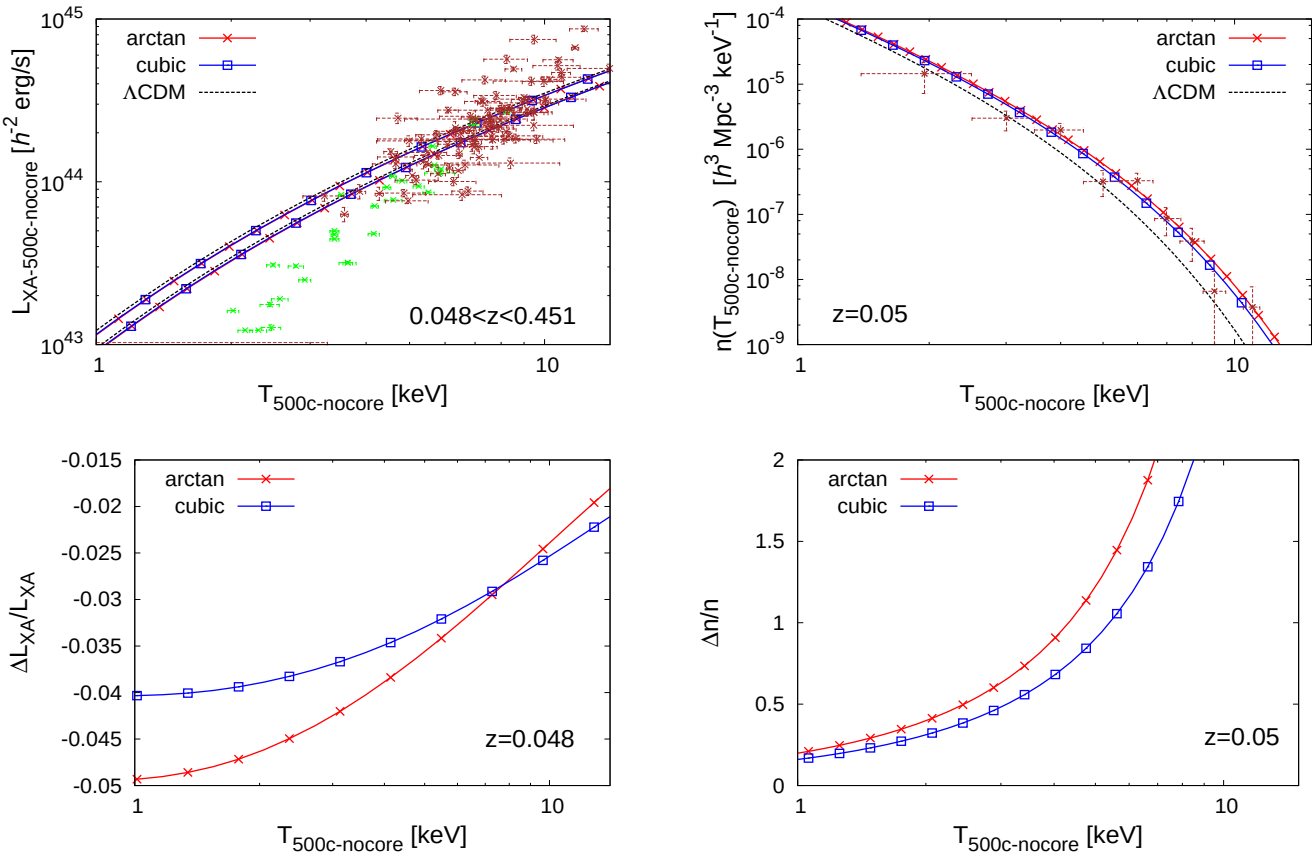

FIG. 16: *Upper panel:* temperature-luminosity relation for the K-mouflage models and the Λ-CDM reference, at $z = 0.048$ (lower curves) and $z = 0.451$ (upper curves). The data points are taken from observations made by [39] (in green) and [38] (in brown), with clusters in the redshift range $0.048 \leq z \leq 0.451$. *Lower panel:* relative deviation of the cluster temperature-luminosity relation from the Λ-CDM reference, at $z = 0.048$.

FIG. 17: *Upper panel:* cluster temperature function for the K-mouflage models and the Λ-CDM reference, at $z = 0.05$. The data points are taken from observations made by [40] from a sample of clusters with $z \simeq 0.05$. *Lower panel:* relative deviation of the cluster temperature function from the Λ-CDM reference at $z = 0.05$

At fixed temperature, the K-mouflage models give a slightly lower X-ray luminosity. This is because at fixed mass K-mouflage models give a higher temperature, as seen in Fig. 15. Therefore they give a lower mass at fixed temperature. Since the X-ray luminosity scales as $L_X \sim \rho_s M\sqrt{T}$, a lower mass implies a lower luminosity (disregarding the impact on ρ_s). As expected, we find percent deviations as for the $M - T$ scaling law.

Thus, as for the quantities studied in previous sections, we obtain percent deviations from the Λ-CDM scaling laws. Unfortunately, this is probably too small to be used as a meaningful constraint on these modified-gravity scenarios, in view of the observational and theoretical uncertainties. Therefore, it is unlikely that cluster scaling laws can provide competitive constraints on such modified-gravity models, that must also pass very tight Solar-System bounds and satisfy larger-scale cosmological constraints associated with the growth of large-scale structures or the evolution of the Hubble expansion rate (e.g., constraints from BBN).

F. Cluster Temperature function

Neglecting the scatter of the mass-temperature relation, by combining the halo mass function described in Sec. IV E with the mass-temperature relation obtained in Sec. V D and Fig. 15, we obtain the X-ray cluster temperature function

$$n(T) = n(M)\frac{\mathrm{d}\ln M}{\mathrm{d}\ln T}. \tag{107}$$

In Fig. 17 we show the temperature functions computed for the K-mouflage models together with the Λ-CDM case, evaluated at $z = 0.05$ to compare them with the observations obtained by [40].

We obtain a reasonable agreement with observations. As is well known, this also means that the cluster tem-

perature is a rather robust quantity (as compared for instance with the X-ray luminosity) and that it is not necessary to build very sophisticated models to recover the right order of magnitude. As shown in the lower panel, we now obtain deviations for the cluster number counts that are of order unity: the K-mouflage models can predict twice or three times more high-T clusters than the Λ-CDM reference. As we have seen, this difference is not due to deviations in the cluster scaling laws, that is, in the intracluster medium, which are quite small, but to the amplification of the high-mass tail of the halo mass function already shown in Fig. 10. Therefore, this result should be rather robust as it is directly related to the faster growth of large-scale structures in the K-mouflage scenarios.

G. Sunyaev-Zel'dovich effect

An indirect method to infer the properties of the clusters is to use the Sunyaev-Zel'dovich effect (hereafter SZE) [13]. It occurs when photons from the CMB inverse Thompson scatter in the intracluster medium. The measured CMB temperature is then distorted with an amplitude proportional to the so-called Compton parameter (see e.g. [41]),

$$y = \int n_e \sigma_T \frac{k_B T_g}{m_e c^2} \mathrm{d}l, \tag{108}$$

where n_e is the electron number density, T_g is the gas temperature, m_e is the electron mass, $\sigma_T = 6.65 \times 10^{-25}$ cm^2 is the Thompson cross-section and dl denotes the integration along the line of sight. Following a common observational practice, by integrating over the angular area of the cluster, defined for instance by the radius R_{500c} associated with the density contrast of 500 with respect to the critical density, we define the integral Compton parameter

$$Y_{500c} \equiv \int y \mathrm{d}\Omega = r_d^{-2}(z) \int_0^{R_{500c}} 4\pi r^2 n_e(r) \sigma_T \frac{k_B T_g}{m_e c^2} \mathrm{d}r, \tag{109}$$

where $r_d(z)$ is the angular distance of the cluster located at redshift z.

In Fig.18 we show the relations $M_{g500c} - Y_{500c} r_d^2(z)$ and $T_{500c-nocore} - Y_{500c} r_d^2(z)$ for the K-mouflage models and the Λ-CDM reference, and we compare them to the observations made by [41]. Again, we obtain a reasonable agreement with observations and a small deviation between the different scenarios. The agreement is better for the $M_g - Y$ relation than for the $T - Y$ relation, but the latter shows a very large scatter and is probably contaminated by large observational errors.

In any case, as in Sec. V E, it appears that deviations of cluster scaling laws associated with modified-gravity scenarios are too small as compared with observational error bars and theoretical uncertainties to be competitive. However, number counts, whether in terms of the cluster temperature or SZ parameter Y, could provide useful constraints.

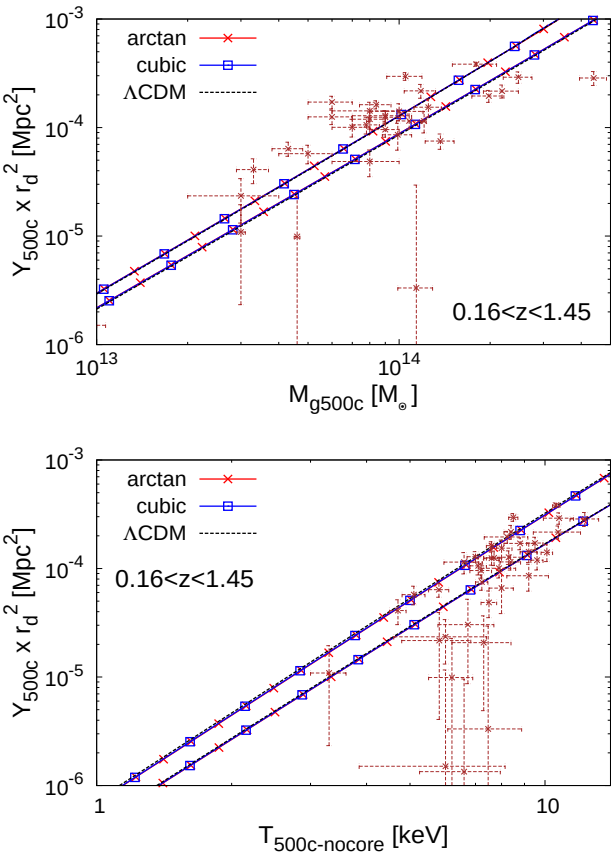

FIG. 18: Integrated Comptonization within R_{500c} as a function of the gas mass (upper panel) and gas temperature (lower panel) for the K-mouflage models and the Λ-CDM reference. These different models cannot be distinguished in these figures. We show our results for $z = 0.16$ (lower curves in the upper panel and upper curves in the lower panel) and $z = 1.45$ (upper curves in the upper panel and lower curves in the lower panel). The data points are measures from a sample of clusters in the range $0.16 \leq z \leq 1.45$ [41].

H. Dynamical and weak lensing masses

Finally, we briefly comment on the dynamical and weak lensing masses of clusters and massive halos. In the unscreened regime, which applies to clusters and larger scales, the dynamics of matter particles (dark matter and the gas) is governed by the metric potential Φ, as in Eqs.(48) and (56). This gravitational potential is related to the matter density through the modified Poisson equation (45) and it is equal to the standard Newtonian potential (but with a time-dependent Newton constant) multiplied by the factor $1 + \epsilon_1$. From observations of the dynamics in clusters one would then measure the dynam-

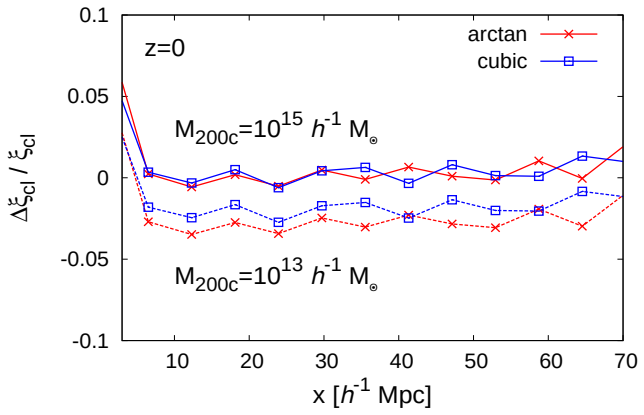

FIG. 19: Relative deviation of the cluster correlation function from the Λ-CDM reference for the K-mouflage models. We consider halos of mass $10^{15}h^{-1}M_\odot$ (upper solid lines) and $10^{13}h^{-1}M_\odot$ (lower dashed lines).

ical mass

$$M_{\rm dyn} \equiv [1+\epsilon_1(t)]\frac{\mathcal{G}(t)}{\mathcal{G}_0}M, \tag{110}$$

assuming General Relativity (GR) gravity with today's Newton's constant. On the other hand, the weak lensing potential $\Phi_{\rm wl}$ that governs the deflection of light rays by the perturbations of the metric is

$$\Phi_{\rm wl} = \frac{\Phi+\Psi}{2} = \Psi_{\rm N}, \tag{111}$$

where we used Eq.(41). Therefore, weak lensing observations of clusters would give the weak lensing mass

$$M_{\rm lens} \equiv \frac{\mathcal{G}(t)}{\mathcal{G}_0}M, \tag{112}$$

and the ratio between the dynamical and weak lensing masses reads as

$$\frac{M_{\rm dyn}}{M_{\rm lens}} = 1+\epsilon_1(t). \tag{113}$$

We have shown the factor ϵ_1 in Fig. 5. Thus, we find that the dynamical mass is greater than the lensing mass by about 2%. As explained above, this is set by the value of $2\beta^2$, which is constrained to be of order 2% or below because of cosmological and Solar System constraints [12] (BBN constraint and bound on the time dependence of $\mathcal{G}$). Therefore, this result on the ratio $M_{\rm dyn}/M_{\rm lens}$ gives an upper bound for its deviation from GR for all realistic K-mouflage models.

I. Cluster correlation function

In the previous sections we considered the internal and integrated properties of clusters, as well as their abundance. Another probe of cosmology is provided by the cluster correlation function. Following [42, 43], we write the halo bias as

$$b(M) = 1 + \frac{\nu^2-1}{\delta_L}. \tag{114}$$

More accurate fitting formulas have been proposed for Λ-CDM cosmologies [44], but they involve free parameters that might vary for different modified-gravity scenarios. Moreover, numerical simulations find that the spherical collapse model (114) provides reasonably good predictions that can fare better than more sophisticated models for rare and massive halos [45], which we focus on here. Therefore, Eq.(114) should be sufficient for our purposes and provide a simple estimate of the impact of K-mouflage models. Note that because clusters are not screened, the reasoning that leads to Eq.(114) in the Λ-CDM cosmology remains valid for K-mouflage scenarios, as the only change is the time-dependent effective Newton's constant as it would be defined from Eq.(63). This enters the bias (114) through the different values of $\nu(M)$ and δ_L, that we compute from the spherical collapse described in Secs. III D and IV E.

Combining the halo bias (114) with the matter correlation function $\xi(x)$ shown in Fig. 11, we obtain the cluster correlation function $\xi_{\rm cl}(x)$ displayed in Fig. 19. The comparison with Fig. 11 shows that the cluster correlation function is much less affected by K-mouflage than the matter correlation and it can actually be slightly lower than in the reference Λ-CDM cosmology. This is because the amplification of gravity, associated with the greater effective Newton's constant $(1+\epsilon_1(t))\mathcal{G}(t)/\mathcal{G}_0$, merely accelerates the growth of large-scale structures. This amplifies the matter density power spectrum and correlation function, as well as the large-mass tail of the halo mass function, as seen in Figs. 11 and 10. However, this same phenomenon also implies that, at a fixed mass M, massive halos are less rare and have a smaller bias $b(M)$ [in particular, $\nu(M)$ becomes smaller in Eq.(114)]. This effect almost cancels the increase of the underlying matter density correlation function. Therefore, it appears that the matter correlation function, measured for instance from weak lensing observations or galaxy surveys (using typical halos with a bias of order unity that is not significantly changed by K-mouflage), is a better probe of such modified-gravity scenarios than the cluster correlation function (or more generally, the correlation of rare objects).

VI. COMPARISON WITH OTHER MODIFIED-GRAVITY MODELS

A. Some other modified-gravity theories

Before we conclude this study of K-mouflage models, it is interesting to compare our results with other modified-gravity models that have been investigated in the literature. The main scenarios that have led to detailed analyt-

ical and numerical studies are the $f(R)$ theories, scalar-field models such as Dilaton and Symmetron models, and Galileon models [46–48].

The $f(R)$ models [4, 49–53], can be recast as scalar-field models with an Einstein-frame action of the form (1), with a standard kinetic term, an exponential coupling function $A(\varphi)$, and a scalar-field potential $V(\varphi)$ [54]. The Dilaton [55–57] and Symmetron [58, 59] models are also scalar-tensor theories of this form, but with different coupling functions $A(\varphi)$ and potentials $V(\varphi)$ (and standard kinetic terms). Finally, Galileon models [60–63] also involve a scalar field, with a non-standard kinetic term (the scalar-field Lagrangian contains higher-order terms in $\nabla\varphi$ and $\nabla^2\varphi$), but there is no coupling function $A(\varphi)$ (i.e., $g_{\mu\nu} = \tilde{g}_{\mu\nu}$). (Of course, it is possible to build more complex models that combine these various ingredients.)

These different scenarios show different nonlinear screening mechanisms that ensure convergence to GR in the Solar System, Chameleon [3] (for $f(R)$ models), Damour-Polyakov [5] (for Dilaton and Symmetron models) and Vainshtein [6] (for Galileon models) mechanisms. The theories that are closest to K-mouflage scenarios are the Galileon models, as their screening mechanism also relies on the nonlinear derivative terms of the scalar-field Lagrangian; but they also involve $\nabla^2\varphi$ instead of $\nabla\varphi$ only, which gives rise to different scaling exponents, for instance for the Vainshtein and K-mouflage screening radii as a function of the mass M of compact objects.

B. Einstein and Jordan frames

A first important difference between the K-mouflage scenario and these other modified-gravity models is the distinction between the Einstein and Jordan frames. As recalled above, this distinction does not apply to the (simplest) Galileon models, but the $f(R)$, Dilaton and Symmetron models also naturally give rise to distinct Einstein and Jordan frames. However, it turns out that in these scenarios the coupling function is constrained to remain very close to unity. Thus, $|A-1| \lesssim 10^{-4}$ for $f(R)$ models, because the "mass" of the scalar field must be sufficiently large, $m \gtrsim 10^3 H/c$, to ensure an efficient screening of the fifth force by a Chameleon mechanism in the Solar System. For Dilaton and Symmetron models we have $|A-1| \lesssim 10^{-6}$ as the coupling strength β must vanish sufficiently fast in high-density regions to screen the fifth force through a Damour-Polyakov mechanism. This means that, in terms of background quantities (e.g., the Hubble expansion rate and the scale factor) one can identify the Einstein and Jordan frames, which also become almost identical to the Λ-CDM reference. However, at the level of the metric perturbations Φ and Ψ, this is no longer the case and the Einstein and Jordan gravitational potentials differ by terms set by δA, and the dynamics of perturbations deviate from the Λ-CDM reference because of the fifth force.

In the K-mouflage case, this identification already breaks down at the background level. Indeed, $|A-1|$ can reach values of the order of a few percents (see Fig. 6) while being consistent with Solar System and cosmological constraints [12]. For the same reason, the background dynamics (in both Einstein and Jordan frames) show percent deviations from the Λ-CDM reference. Therefore, we must pay attention to the distinction between Einstein and Jordan frames already at the background level. In particular, in this paper, as we study clusters of galaxies that involve atomic or radiative processes (both for the definition of their redshift, from atomic lines, and for their properties such as X-ray emission), the Jordan frame is the one that is more directly connected to observations and we work in this frame. Another advantage of the Jordan frame is that the equations of motion take their usual form, in particular matter is conserved, which permits a clear and simple physical interpretation, and only gravity is modified. In contrast, in the Einstein frame gravity takes a standard form but the equations of motion are modified and the matter density is usually not conserved.

C. Scale dependence and screening regime

A second important difference between the K-mouflage scenario and some other modified-gravity models is that the deviations from the Λ-CDM reference are scale independent on perturbative scales (from cluster scales to the horizon). This is most easily seen from the fact that the factor $\epsilon_1(t)$ that enters the evolution equation (55) of the linear growing mode only depends on time, so that the linear growing mode $D_+(t)$ remains scale independent as in the Λ-CDM cosmology. This is due to the fact that in the scalar-field Lagrangian (6) we focused on the non-standard kinetic term and neglected a possible potential term $V(\varphi)$. Of course, in the highly nonlinear regime a new scale dependence appears, as the fluctuations of the scalar field themselves become nonlinear and give rise to the K-mouflage screening mechanism, which ensures the convergence to GR in the Solar System. However, it happens that the screening transition appears at galaxy scales, so that clusters remain unscreened and fully feel the effect of the fifth force.

The same behavior is obtained in the Galileon models, where linear scales below the horizon show scale-independent growing modes and the Vainshtein screening mechanism applies to cluster scales and below [64, 65]; but in the K-mouflage case the nonlinear screening only applies to galaxy scales and below, as clusters remain unscreened. In contrast, in $f(R)$ and Dilaton/Symmetron models, there is a characteristic scale dependence, as we recover GR both on very large scales $x \gg 1h^{-1}$Mpc (because of the finite mass of the scalar field) and on very small scales $x \ll 1h^{-1}$Mpc (because of nonlinear screening mechanisms, here Chameleon or Damour-Polyakov mechanisms [3, 5]). Then, the linear growing mode

$D_+(k,t)$ shows a clear scale dependence on quasilinear scales and nonlinear screening effects also add a further scale dependence around $x \sim 1h^{-1}$Mpc [66]. Thus, in these models clusters probe a scale-dependent regime and the transition between the unscreened and screened regimes.

Therefore, clusters of galaxies are especially well-suited probes of K-mouflage scenarios because they are unscreened (hence they feel the full amplitude of the fifth force). Moreover, the modification of gravity is still scale independent on these scales so that cluster properties should not be too difficult to model (the same modelizations should apply equally well to the Λ-CDM and K-mouflage cosmologies).

D. Clusters

1. *Cluster profiles*

The effect of the fifth force on the cluster matter and gas profiles within the context of modified-gravity scenarios with chameleon mechanisms [mostly for $f(R)$ models] has been investigated in [67–70].

As recalled above, the fifth force effect is somewhat different between $f(R)$, Dilaton and Symmetron models, and K-mouflage scenarios. In the former cases clusters are typically at the transition between the screened and unscreened regimes. Then, massive clusters are screened by the Chameleon or Damour-Polyakov mechanisms (the deviations from GR being most efficiently suppressed in the Symmetron models) while for low-mass clusters only a small core is efficiently screened. In particular, for $f(R)$ and Symmetron models the amplification of gravity is localized in the outskirts of massive clusters. This gives a distinct scale dependence of the modified-gravity effect in these theories [71, 72], but the efficient screening also decreases the overall deviation from GR. See for instance [66] for a detailed analysis and comparison of these different models and [71, 73–76] for numerical simulations of various models. In Galileon scenarios, depending on the model, clusters may be fully screened (and their profiles are similar to those of a quintessence model with no fifth force and the same expansion history) or only partly screened (which gives rise to complex effects) [65]. In the K-mouflage case, clusters still are in the unscreened regime. Therefore, there is no characteristic scale dependence that can be used to distinguish them from Λ-CDM cosmologies, but the amplitude of the smooth deviation is greater (as compared with screened scenarios).

There have been no specific simulations of K-mouflage models so far, but we can recall here some results from simulations of other modified-gravity models.

Ref. [76] develops hydrodynamic N-body simulations to investigate the impact on dark matter and gas profiles of $f(R)$ and Symmetron scenarios. In agreement with the discussion above, the authors find that the dark matter density is increased as compared with the Λ-CDM reference in the outskirts of massive halos. This is because the fifth force applies to outer radii, which are unscreened, and this also yields a greater velocity to the particles, which cannot cluster as strongly within inner radii. They also find a lower deviation from Λ-CDM for the gas density profile than for the dark matter density profile. They note that this may be due to delays in the collapse of the dark matter and the gas, with the screening of the halos taking place after dark matter collapse and before gas collapse. As explained above, for K-mouflage scenarios we do not expect such a localized enhancement in the matter densities and different behaviors for the dark matter and the gas, because clusters are unscreened and the dynamics remains similar to the Λ-CDM cosmology, as illustrated by the explicit symmetry described in Sec. III G. In fact, in Fig. 14 we find that within our very simple model the deviation from Λ-CDM is slightly greater for the gas than for the dark matter [because of the small change in the concentration parameter and the higher sensitivity for the gas that arises from the exponential equilibrium distribution (98)].

We can note that N-body simulations of $f(R)$ models also find that in the case $f_{R_0} = -10^{-4}$, where Chameleon screening is not efficient, deviations from Λ-CDM are smooth and the velocity dispersion σ_v^2 and gas temperature T_g are about 4/3 times the GR value [68, 74], due to the 4/3 increase of the effective Newton's constant. In our case, this corresponds to the $(1+\epsilon_1)$ enhancement in Eq.(100), but with $\epsilon_1 \simeq 2\%$ instead of 1/3. These simulations also find that dark matter halos remain well described by NFW profiles [77]. These results suggest that our approach for the density profiles and the gas temperature described in Secs. V A and V D should fare reasonably well.

For Chameleon scenarios, Ref. [67] considers the effect of the fifth force on the cluster gas profile, which becomes more compact for a given dark matter profile [in our case, we also include the effect on the dark matter profile, through the modification of the concentration parameter shown in Fig. 12, and we assume an isothermal gas (i.e., $\gamma = 1$) instead of a polytropic equation of state $p_g \propto \rho_g^\gamma$ with $\gamma \sim 1.2$]. However, they find that observational error bars are too large to give useful constraints on $f(R)$ models. We reach the same conclusion for the K-mouflage models studied in this paper.

Refs. [69, 70] combine X-ray observations (which probe the temperature and electron number density profiles) and weak lensing signals (which probe the total matter profile) to constrain deviations from General Relativity. Indeed, while the gas profile is sensitive to the fifth force the lensing deflection of light rays remains the same as in GR. This allows them to derive the upper bound $|f_{R_0}| \leq 6 \times 10^{-5}$. The same behavior applies to the K-mouflage scenario. In this paper we found a few percent deviations from GR, which should apply to all realistic K-mouflage models that satisfy cosmological and Solar System constraints [as this is due to the constraint on the coupling β, independently of the details of the kinetic

function $K(\chi)$]. We leave a more general MCMC analysis of K-mouflage scenarios, combining different probes, to future works.

2. Cluster scaling relations

The impact of $f(R)$ gravity on the cluster scaling relations has been studied in Ref.[68] with numerical simulations. Again, we find similar behaviors for the K-mouflage models as for the $f(R)$ model with $f_{R_0} = -10^{-4}$, where clusters are not screened. In particular, the dark matter velocity dispersion and gas temperature are increased, at fixed mass, and the X-ray luminosity is decreased, at fixed temperature, as compared with the Λ-CDM reference. However, whereas in $f(R)$ theories the deviations from Λ-CDM can reach a factor 1/3 in the unscreened regime, and deviations of order unity can also be expected in Dilaton or Symmetron models, realistic K-mouflage models can only deviate by a few percent at most. Indeed, the magnitude of these deviations is set by the factor ϵ_1, which itself is set by $2\beta^2$ (at $z = 0$) and the coupling strength must satisfy $\beta \leq 0.1$ because of cosmological and Solar System constraints [12].

3. Cluster lensing; Dynamical and lensing masses

In $f(R)$, Dilaton and Symmetron scenarios the weak lensing potential $\Phi_{\rm wl}$ that governs the deflection of light rays, given by $\Phi_{\rm wl} = (\Phi + \Psi)/2$, is equal to the Newtonian potential $\Psi_{\rm N}$ [using $|f_{R_0}| \ll 1$ in the case of $f(R)$ theories] [78]. Then, for weak lensing observations the only difference from the Λ-CDM scenario comes from the different evolution of the matter density fields. In contrast, the motions of matter particles or of small halos (e.g., satellite halos or small galaxies), which fall towards massive clusters, feel the fifth force. This gives rise to different lensing and dynamical masses. This has been investigated in semianalytical models and N-body simulations [74, 79] and used in [69, 70] in combination with X-ray observations, for $f(R)$ theories, and in [80], using the galaxy infall kinematics onto massive clusters, for $f(R)$ and Galileon models.

In the K-mouflage scenario, we again have $\Phi_{\rm wl} = \Psi_{\rm N}$, as the factor $\delta A/\bar{A}$ cancels from the sum over the two metric potentials, see Eq.(41). However, in contrast with the former theories the effective Newton constant [which enters the Newtonian potential (42)] now depends on time, as in Eq.(77). (This effect does not appear in the other scenarios because they have $\bar{A}$ very close to unity, within 10^{-4} or better.) On the other hand, this time-dependent prefactor cancels from the ratio between the dynamical and lensing potentials or masses, see Eq.(113). However, whereas in $f(R)$ theories this ratio can again deviate from unity by a factor 1/3 in the unscreened regime, and deviations of order unity can also be reached in Dilaton or Symmetron models, in realistic K-mouflage models this ratio can only deviate from unity by 2% at most because of observational constraint on the scalar-field coupling, $\beta \leq 0.1$. Therefore, K-mouflage models cannot significantly decrease the tension between measures of X-ray and lensing clusters masses.

4. Cluster number counts

In most modified-gravity scenarios the growth of large-scale perturbations differs from the GR evolution. This typically leads to a new scale dependence of the linear growth rates (e.g., in $f(R)$, Dilaton and Symmetron models), as one goes from the very large scales (beyond the Compton wavelength of the scalar field) where GR is recovered to the quasi-linear scales where the fifth force is unscreened and gives its maximum amplification of the gravitational interaction (at smaller scales nonlinear screening leads again to a convergence to GR). This amplification typically yields a faster growth of matter density perturbations on scales $1h^{-1}$Mpc to $10h^{-1}$Mpc, whence a greater abundance of massive halos and clusters as compared with the Λ-CDM cosmology, see Refs. [65, 73, 81–84] for numerical studies of various models. As explained above, a similar enhancement is found in the K-mouflage scenarios, with the important difference that all clusters are unscreened and that the modification of gravity extends up to the horizon (so that the linear modes grow faster than in Λ-CDM but remain scale independent). In Galileon scenarios, the screening mechanism has a strong impact and, depending on the models, the tail of the halo mass function can be either increased or decreased, as compared with a quintessence scenario with the same expansion history [65].

The abundance of massive clusters has been used within $f(R)$ theories to constrain f_{R_0} [85–87]. In combination with CMB, BAO and SNeIa observations, one can obtain an upper bound $|f_{R_0}| \lesssim 1.7 \times 10^{-5}$ [86, 87], but most of the constraint comes from the cluster data. We can expect that for K-mouflage models similar results should be obtained, especially since clusters are unscreened so that their abundance should provide useful constraints. In this paper we presented the physics of K-mouflage scenarios on cluster scales, highlighting the difference between the Einstein and Jordan frames (which can be neglected in most other scenarios) and investigating both the modified growth of structures and halo mass functions and the modified cluster scaling laws. We leave a detailed MCMC analysis of the K-mouflage parameter space to future works.

5. Cluster correlation function

In modified-gravity scenarios, the correlation function and the power spectrum of the matter density field are often increased as the growth of large-scale structures is amplified by the fifth force. This also enhances the

large-mass tail of the halo mass function and decreases the bias of massive halos as they become less rare. In the K-mouflage models that we considered in this paper, this decrease of the cluster bias mostly cancels the increase of the underlying matter density correlation, and the cluster correlation function is much closer to the Λ-CDM reference than the matter correlation itself. Therefore, the correlation of the matter density field, which can be measured from weak lensing observations for instance, is a better probe of modified cosmology than the clustering of massive halos. The same effects, with a similar compensation between the smaller bias and the higher matter correlation (but the compensation may only be partial, depending on the model) appear in other modified-gravity scenarios, see for instance Ref.[88] for $f(R)$ theories.

E. Other tests

On slightly larger scales than those probed by clusters of galaxies, modified-gravity models have also been tested from galaxy surveys, using redshift-space distortions of the galaxy power spectrum [89], the clustering of Luminous Red Galaxies [65], or the shape of the galaxy correlation function itself [90]. Similar studies could be performed for K-mouflage models, as they can lead to 20% deviations for the matter power spectrum and correlation function, as seen in Fig. 11. This will be investigated in future works.

In between the cluster and cosmological scales (e.g., the formation of large-scale structures and the background dynamics) and the Solar System scales (where we must recover GR up to a very high accuracy), modified-gravity theories have also been tested on intermediate galaxy scales. In particular, within Chameleon scenarios, low-mass galaxies should be unscreened so that the rotation curve of their diffuse gas component probes the fifth force, while their stars, being compact high-density objects, are screened and move as in GR [91]. This can provide constraints as tight as $|f_{R_0}| \leq 10^{-6}$ for $f(R)$ theories [92]. The same behaviors apply to K-mouflage models and we can expect that such tests could also provide useful constraints on these scenarios. We leave this task to future studies.

Numerical simulations have also been used to investigate the impact of $f(R)$ theories on Lyman-α forest observations (the transmitted flux fraction and the flux power spectrum) [93]. They find changes that are too small as compared with observational error bars and do not provide competitive constraints. Although this study does not distinguish the impact of screening effects, screening can be expected to be rather inefficient for such moderate density fluctuations. Therefore, it is likely that similar conclusions would be reached for K-mouflage models, but we leave a detailed study for future works.

VII. CONCLUSIONS

We have extended previous works on K-mouflage models by deriving the equations of motion in both the Einstein and Jordan frames for a fluid with pressure, and next focusing on the usual case where the pressure arises from small-scale nonlinear processes. In contrast with many modified-gravity scenarios, the Einstein and Jordan frames already differ by a few percent at the background level, for K-mouflage models that are consistent with cosmological and Solar System constraints. Therefore, one must take into account these deviations and use the correct quantities when comparing with observations.

We focused on the Jordan frame, which is better suited to cosmological probes that involve atomic processes, such as X-ray clusters. We show that even though K-mouflage models only differ from the Λ-CDM reference by a few percent at the background level, the linear growing modes can deviate by 10% and the matter density power spectrum and correlation function by 30%. The tail of the halo mass function is enhanced by factors of order unity for $M \gtrsim 10^{14}h^{-1}M_\odot$ at $z = 0$.

Galaxy clusters are not screened by the K-mouflage mechanism, contrary to what happens for chameleon models like $f(R)$ in the large curvature limit or Galileon models subject to the Vainshtein screening. For this reason, we investigate the effects of the K-mouflage modification of gravity on clusters. We take into account the impact of the fifth force mediated by the K-mouflage scalar field on both the dark matter and gas profiles, through the modifications to the growth of large-scale structures and to the hydrostatic equilibrium. We find that K-mouflage makes clusters slightly more compact. Similarly, the gas temperature and the X-ray luminosity differ from their Λ-CDM counterparts by a few percent, an order of magnitude which follows directly from the constraints on K-mouflage (especially on the coupling strength β) due to Solar System tests. The only deviation of noticeable order appears in the cluster temperature function, as the number of clusters is larger than in the Λ-CDM scenario for K-mouflage models, because of the faster growth of large-scale structures. This appears to be large enough that one can hope that this will be within the reach of the future large-scale surveys. On the other hand, the cluster correlation function only deviates by a few percent from the Λ-CDM case because the increase of the underlying matter density correlation function is compensated by the lower cluster bias, as massive halos become less rare at fixed mass, due to the enhanced structure formation.

In this paper we only considered two kinetic functions $K(\tilde{\chi})$ to illustrate the K-mouflage scenarios and to estimate the amplitude of the effects that can be reached by realistic models, which are consistent with cosmological and Solar System constraints. We leave to future works a more detailed MCMC analysis of K-mouflage scenarios, which would provide the parameter space of K-mouflage models that is allowed by cluster observations and com-

binations with other observational probes.

Acknowledgments

This work is supported in part by the French Agence Nationale de la Recherche under Grant ANR-12-BS05-0002. P.B. acknowledges partial support from the European Union FP7 ITN INVISIBLES (Marie Curie Actions, PITN- GA-2011- 289442) and from the Agence Nationale de la Recherche under contract ANR 2010 BLANC 0413 01.

Appendix A: Equations of motion in the Einstein frame

In this appendix we derive the equations of motion of the scalar field and of the matter component in the Einstein frame, for a cosmological fluid with a nonzero pressure. The derivation is similar to the one presented in previous papers [7, 8], where we studied the background cosmological dynamics and the formation of large-scale cosmological structures, but with the addition of the pressure terms.

1. Energy-momentum tensors and equations of motion

We consider three components of the energy density of the Universe, a matter fluid with nonzero pressure, radiation, and the scalar field. The Einstein-frame and Jordan-frame matter energy-momentum tensors are given by Eq.(10) and they satisfy the relations (11). Assuming a perfect fluid, the matter energy-momentum tensor writes as

$$\tilde{T}^{\mu}_{\nu} = (\tilde{\rho}+\tilde{p})\,\tilde{u}^{\mu}\tilde{u}_{\nu} + \tilde{p}\,\delta^{\mu}_{\nu}, \tag{A1}$$

where $\tilde{u}^{\mu}$ is the velocity 4-vector, normalized such that $\tilde{u}^{\mu}\tilde{u}_{\mu} = -1$, and $\tilde{\rho}$ and $\tilde{p}$ are the Einstein-frame density and pressure, which are related to their Jordan-frame counterparts by Eq.(12).

For the radiation component, we neglect perturbations and only consider the contribution to the background, with the mean density and pressure $\bar{\tilde{\rho}}_{(\mathrm{r})}$ and $\bar{\tilde{p}}_{(\mathrm{r})} = \bar{\tilde{\rho}}_{(\mathrm{r})}/3$. Their Jordan-frame counterparts are again given as in Eq.(12).

The Einstein-frame energy-momentum tensor of the scalar field reads as

$$\tilde{T}_{\mu\nu(\varphi)} = \frac{-2}{\sqrt{-\tilde{g}}}\frac{\delta S_{\varphi}}{\delta\tilde{g}^{\mu\nu}} = K'\tilde{\nabla}_{\mu}\varphi\tilde{\nabla}_{\nu}\varphi + \mathcal{M}^4 K\tilde{g}_{\mu\nu}. \tag{A2}$$

The Klein-Gordon equation that governs the dynamics of the scalar field φ is obtained from the variation of the action (1) with respect to φ. This yields

$$\tilde{\nabla}_{\mu}\left[\tilde{\nabla}^{\mu}\varphi\; K'\right] = (\tilde{\rho}-3\tilde{p})\frac{\mathrm{d}\ln A}{\mathrm{d}\varphi}. \tag{A3}$$

Here we used the fact that the trace of the matter energy-momentum tensor is $\tilde{T}^{\mu}_{\mu} = -\tilde{\rho}+3\tilde{p}$, from Eq.(A1), while it is zero for the radiation component as $\tilde{p}_{(\mathrm{r})} = \tilde{\rho}_{(\mathrm{r})}/3$. Combining with Eq.(A2), we find for the scalar field the "non-conservation" equation

$$\tilde{\nabla}_{\mu}\tilde{T}^{\mu}_{\nu(\varphi)} = (\tilde{\rho}-3\tilde{p})\,\tilde{\nabla}_{\nu}\ln A. \tag{A4}$$

The matter energy-momentum tensor is conserved in the Jordan frame,

$$\nabla_{\mu}T^{\mu}_{\nu} = 0, \tag{A5}$$

which gives in the Einstein frame the non-conservation equation

$$\tilde{\nabla}_{\mu}\tilde{T}^{\mu}_{\nu} = -(\tilde{\rho}-3\tilde{p})\,\tilde{\nabla}_{\nu}\ln A. \tag{A6}$$

On the other hand, the radiation energy-momentum tensor is conserved in both frames,

$$\nabla_{\mu}T^{\mu}_{\nu(\mathrm{r})} = 0, \quad \tilde{\nabla}_{\mu}\tilde{T}^{\mu}_{\nu(\mathrm{r})} = 0. \tag{A7}$$

The sum of all energy-momentum tensors is also conserved in both frames, and $\tilde{\nabla}_{\mu}[\tilde{T}^{\mu}_{\nu} + \tilde{T}^{\mu}_{\nu(\mathrm{r})} + \tilde{T}^{\mu}_{\nu(\varphi)}] = \nabla_{\mu}[T^{\mu}_{\nu} + T^{\mu}_{\nu(\mathrm{r})} + T^{\mu}_{\nu(\varphi)}] = 0$.

Finally, in the Einstein frame the Einstein equations take the usual form, $\tilde{M}^2_{\mathrm{Pl}}\tilde{G}^{\mu}_{\nu} = \tilde{T}^{\mu}_{\nu} + \tilde{T}^{\mu}_{\nu(\mathrm{r})} + \tilde{T}^{\mu}_{\nu(\varphi)}$.

2. Background dynamics

At the level of the cosmological background, the Friedmann equations take the usual form in the Einstein frame,

$$3\tilde{M}^2_{\mathrm{Pl}}\tilde{H}^2 = \bar{\tilde{\rho}} + \bar{\tilde{\rho}}_{(\mathrm{r})} + \bar{\tilde{\rho}}_{\varphi}, \tag{A8}$$

$$-2\tilde{M}^2_{\mathrm{Pl}}\frac{\mathrm{d}\tilde{H}}{\mathrm{d}\tilde{t}} = \bar{\tilde{\rho}} + \bar{\tilde{p}} + \bar{\tilde{\rho}}_{(\mathrm{r})} + \bar{\tilde{p}}_{(\mathrm{r})} + \bar{\tilde{\rho}}_{\varphi} + \bar{\tilde{p}}_{\varphi}, \tag{A9}$$

where $\bar{\tilde{\rho}}_{\varphi}$ and $\bar{\tilde{p}}_{\varphi}$ are the background scalar-field energy density and pressure (in the Einstein frame), given by Eq.(17).

The Klein-Gordon equation (A3) gives

$$\frac{\mathrm{d}}{\mathrm{d}\tilde{t}}\left[\tilde{a}^3\frac{\mathrm{d}\bar{\varphi}}{\mathrm{d}\tilde{t}}\bar{K}'\right] = -\tilde{a}^3(\bar{\tilde{\rho}}-3\bar{\tilde{p}})\frac{\mathrm{d}\ln\bar{A}}{\mathrm{d}\bar{\varphi}}, \tag{A10}$$

and the scalar-field energy density satisfies

$$\frac{\mathrm{d}\bar{\tilde{\rho}}_{\varphi}}{\mathrm{d}\tilde{t}} = -3\tilde{H}(\bar{\tilde{\rho}}_{\varphi}+\bar{\tilde{p}}_{\varphi}) - (\bar{\tilde{\rho}}-3\bar{\tilde{p}})\frac{\mathrm{d}\ln\bar{A}}{\mathrm{d}\tilde{t}}. \tag{A11}$$

The non-conservation equation (A6) gives for the matter density the evolution equation

$$\frac{\mathrm{d}\bar{\tilde{\rho}}}{\mathrm{d}\tilde{t}} = -3\tilde{H}(\bar{\tilde{\rho}}+\bar{\tilde{p}}) + (\bar{\tilde{\rho}}-3\bar{\tilde{p}})\frac{\mathrm{d}\ln\bar{A}}{\mathrm{d}\tilde{t}}. \tag{A12}$$

In particular, we have $\mathrm{d}(\bar{\tilde{\rho}}+\bar{\tilde{\rho}}_\varphi)/\mathrm{d}\tilde{t} = -3\tilde{H}(\bar{\tilde{\rho}}+\bar{\tilde{p}}+\bar{\tilde{\rho}}_\varphi+\bar{\tilde{p}}_\varphi)$. When the pressure is zero, we can define a conserved density $\hat{\rho}$ by

$$\hat{\rho} = \tilde{\rho}/A, \quad \hat{p} = \tilde{p}/A. \tag{A13}$$

Indeed, substituting into Eq.(A12) gives

$$\frac{\mathrm{d}\bar{\hat{\rho}}}{\mathrm{d}\tilde{t}} = -3\tilde{H}(\bar{\hat{\rho}}+\bar{\hat{p}}) - 3\bar{\hat{p}}\frac{\mathrm{d}\ln\bar{A}}{\mathrm{d}\tilde{t}}. \tag{A14}$$

Thus, if $\hat{p} = 0$ we obtain a conservation of the standard form in the Einstein frame, $\mathrm{d}\bar{\hat{\rho}}/\mathrm{d}\tilde{t} = -3\tilde{H}\bar{\hat{\rho}}$. However, if $\hat{p} \neq 0$ it is no longer possible to cancel the non-conservation term of Eq.(A12) by such a simple redefinition of the density.

The background radiation density obeys the usual conservation equation,

$$\frac{\mathrm{d}\bar{\tilde{\rho}}_{(\mathrm{r})}}{\mathrm{d}\tilde{t}} = -3\tilde{H}(\bar{\tilde{\rho}}_{(\mathrm{r})}+\bar{\tilde{p}}_{(\mathrm{r})}) = -4\tilde{H}\bar{\tilde{\rho}}_{(\mathrm{r})}, \tag{A15}$$

in agreement with the second Eq.(A7).

3. Perturbations

In the conformal Newtonian gauge the Einstein-frame metric can be written as

$$\mathrm{d}\tilde{s}^2 = \tilde{a}^2[-(1+2\tilde{\Phi})\mathrm{d}\tau^2 + (1-2\tilde{\Psi})\mathrm{d}\mathbf{x}^2], \tag{A16}$$

where $\tau = \int \mathrm{d}\tilde{t}/\tilde{a}$ is the conformal time, and $\tilde{\Phi}$ and $\tilde{\Psi}$ are the two metric gravitational potentials. Throughout this paper, we consider the non-relativistic and weak-gravitational-fields regime, with $\tilde{\Phi} \ll 1$, $\tilde{\Psi} \ll 1$, $v^2 \ll 1$ (where $\mathbf{v} = \mathrm{d}\mathbf{x}/\mathrm{d}\tau$ is the peculiar velocity of the particles), and we expand up to first order in $\{\tilde{\Phi}, \tilde{\Psi}, v^2\}$. Then, in the final equations, we only keep zeroth-order terms, $1+\tilde{\Psi} \simeq 1$ and $1+v^2 \simeq 1$, except when the potentials or the velocity arise with a gradient operator, as in Eqs.(A24) and (A27). In particular, we have for the matter velocity 4-vector,

$$\tilde{u}^\mu = \tilde{a}^{-1}(1-\tilde{\Phi}+v^2/2, v^i), \quad \tilde{u}_\mu = -\tilde{a}(1+\tilde{\Phi}+v^2/2, -v_i), \tag{A17}$$

where we denote

$$v_i = v^i = \frac{\mathrm{d}x^i}{\mathrm{d}\tau} \tag{A18}$$

the peculiar velocity.

The non-conservation equation (A6) gives

$$(\dot{\tilde{\rho}}+\dot{\tilde{p}})\tilde{u}_\nu + 3\tilde{h}(\tilde{\rho}+\tilde{p})\tilde{u}_\nu + (\tilde{\rho}+\tilde{p})\dot{\tilde{u}}_\nu + \tilde{\nabla}_\nu\tilde{p} = -(\tilde{\rho}-3\tilde{p})\tilde{\nabla}_\nu(\ln A), \tag{A19}$$

where we have introduced

$$\dot{\tilde{\rho}} \equiv \tilde{u}^\mu\tilde{\nabla}_\mu\tilde{\rho}, \quad \dot{\tilde{u}}_\nu \equiv \tilde{u}^\mu\tilde{\nabla}_\mu\tilde{u}_\nu, \quad 3\tilde{h} \equiv \tilde{\nabla}_\mu\tilde{u}^\mu. \tag{A20}$$

Contracting with $\tilde{u}^\nu$ and using $\tilde{u}^\nu\tilde{u}_\nu = -1$, we get

$$\dot{\tilde{\rho}} + 3\tilde{h}(\tilde{\rho}+\tilde{p}) = (\tilde{\rho}-3\tilde{p})\frac{\dot{A}}{A}. \tag{A21}$$

It is easy to see that $\dot{\tilde{\rho}} = \tilde{a}^{-1}[\partial_\tau\tilde{\rho} + (\mathbf{v}\cdot\nabla)\tilde{\rho}]$, where $\nabla \equiv \partial/\partial\mathbf{x}$ is the standard 3D spatial gradient, and $3\tilde{h} = \tilde{a}^{-1}[3\tilde{\mathcal{H}} + (\nabla\cdot\mathbf{v})]$, where $\tilde{\mathcal{H}} = \mathrm{d}\ln\tilde{a}/\mathrm{d}\tau$ is the conformal expansion rate in the Einstein frame. Therefore, this is explicitly

$$\frac{\partial\tilde{\rho}}{\partial\tau} + (\mathbf{v}\cdot\nabla)\tilde{\rho} + (3\tilde{\mathcal{H}}+\nabla\cdot\mathbf{v})(\tilde{\rho}+\tilde{p}) = (\tilde{\rho}-3\tilde{p})\left[\frac{\partial\ln A}{\partial\tau} + (\mathbf{v}\cdot\nabla)\ln A\right]. \tag{A22}$$

Next, the non-conservation equation (A19) can be simplified by subtracting Eq.(A21) multiplied by $\tilde{u}_\nu$. This leads to

$$\dot{\tilde{u}}_\nu = -\frac{\tilde{\nabla}_\nu\tilde{p}+\tilde{u}_\nu\dot{\tilde{p}}}{\tilde{\rho}+\tilde{p}} - \frac{\tilde{\rho}-3\tilde{p}}{\tilde{\rho}+\tilde{p}}\frac{\tilde{\nabla}_\nu A + \tilde{u}_\nu\dot{A}}{A}. \tag{A23}$$

This is the generalized geodesic equation. Specializing to $\mu = i$, we get the Euler equation of K-mouflage hydrodynamics,

$$\frac{\partial\mathbf{v}}{\partial\tau} + (\mathbf{v}\cdot\nabla)\mathbf{v} + \left(\tilde{\mathcal{H}} + \frac{1}{\tilde{\rho}+\tilde{p}}\frac{\partial\tilde{p}}{\partial\tau} + \frac{\tilde{\rho}-3\tilde{p}}{\tilde{\rho}+\tilde{p}}\frac{\partial\ln A}{\partial\tau}\right)\mathbf{v} = -\nabla\tilde{\Phi} - \frac{\nabla\tilde{p}}{\tilde{\rho}+\tilde{p}} - \frac{\tilde{\rho}-3\tilde{p}}{\tilde{\rho}+\tilde{p}}\nabla\ln A \tag{A24}$$

From Eq.(A24) we can see that $(\mathbf{v}\cdot\nabla)\ln A \sim \partial_\tau v^2 + v^2(\nabla\cdot\mathbf{v})$, hence this term can be neglected in the continuity equation (A22) in the non-relativistic limit $v^2 \ll 1$. This simplifies as

$$\frac{\partial\tilde{\rho}}{\partial\tau} + (\mathbf{v}\cdot\nabla)\tilde{\rho} + (3\tilde{\mathcal{H}}+\nabla\cdot\mathbf{v})(\tilde{\rho}+\tilde{p}) = (\tilde{\rho}-3\tilde{p})\frac{\partial\ln A}{\partial\tau}. \tag{A25}$$

The Klein-Gordon equation (A3) writes as

$$\frac{1}{\tilde{a}^3}\frac{\partial}{\partial\tilde{t}}\left(\tilde{a}^3\frac{\partial\varphi}{\partial\tilde{t}}\,K'\right) - \frac{1}{\tilde{a}^2}\nabla\cdot(\nabla\varphi\,K') = -(\tilde{\rho}-3\tilde{p})\frac{\mathrm{d}\ln A}{\mathrm{d}\varphi}. \tag{A26}$$

The $(0,0)$ component of Einstein equations, $\tilde{M}_{\mathrm{Pl}}^2\tilde{G}_0^0 = \tilde{T}_0^0 + \tilde{T}_{0(\varphi)}^0$, gives

$$\tilde{\Psi} = \tilde{\Psi}_{\mathrm{N}} \quad \text{with} \quad \frac{1}{\tilde{a}^2}\nabla^2\tilde{\Psi}_{\mathrm{N}} = \frac{1}{2\tilde{M}_{\mathrm{Pl}}^2}(\delta\tilde{\rho}+\delta\tilde{\rho}_\varphi), \tag{A27}$$

where $\delta\tilde{\rho} = \tilde{\rho} - \bar{\tilde{\rho}}$ and $\delta\tilde{\rho}_\varphi = \tilde{\rho}_\varphi - \bar{\tilde{\rho}}_\varphi$, with $\tilde{\rho}_\varphi = -\mathcal{M}^4K + K'(\partial\varphi/\partial\tilde{t})^2$. Here we denoted $\tilde{\Psi}_{\mathrm{N}}$ the usual Newtonian potential. The (i,j) components of the Einstein equations give (focusing on the part that is not proportional to δ_j^i),

$$\frac{\tilde{M}_{\mathrm{Pl}}^2}{\tilde{a}^2}\partial_i\partial_j(\tilde{\Psi}-\tilde{\Phi}) = (\tilde{\rho}+\tilde{p})v_iv_j + \frac{K'}{\tilde{a}^2}\partial_i\varphi\partial_j\varphi. \tag{A28}$$

From Eq.(A27) we can see that on the left-hand side in Eq.(A28) we have $\tilde{M}_{\rm Pl}^2\tilde{a}^{-2}\partial_i\partial_j\tilde{\Psi}\sim\delta\tilde{\rho}\sim\tilde{\rho}$. Therefore, the first term on the right-hand side, $(\tilde{\rho}+\tilde{p})v_iv_j$, is negligible as $v^2\ll 1$. Next, from the Klein-Gordon equation (A26) we obtain, on scales that are much smaller than the horizon,

$$k/\tilde{a}\tilde{H}\gg 1: \quad \delta\varphi\sim\frac{\beta}{\tilde{M}_{\rm Pl}}\frac{\tilde{a}^2}{k^2}\frac{\delta\tilde{\rho}-3\delta\tilde{p}}{K'} \tag{A29}$$

where k is the typical comoving wave number of interest. Then, the second term in the right-hand side in Eq.(A28) is of order

$$\frac{K'}{\tilde{a}^2}\partial_i\varphi\partial_j\varphi\sim\delta\tilde{\rho}\frac{\delta\tilde{\rho}}{\bar{\tilde{\rho}}}\frac{\beta^2}{K'}\frac{\tilde{a}^2\tilde{H}^2}{k^2}\ll\delta\tilde{\rho}, \tag{A30}$$

which is again negligible compared to $\tilde{M}_{\rm Pl}^2\tilde{a}^{-2}\partial_i\partial_j\tilde{\Psi}$. Therefore, the Einstein equations (A28) give

$$\tilde{\Phi}=\tilde{\Psi}=\tilde{\Psi}_{\rm N}, \tag{A31}$$

within the approximations that we use in this paper.

To close the system formed by the equations of motion obtained above, we must specify the pressure, for instance through an (effective) equation of state such as $\tilde{p}=w\tilde{\rho}$ with some parameter w.

4. Pressure due to small-scale nonlinear physics

In the previous sections, we derived the equations of motion for a cosmological fluid with a nonzero pressure, in the non-relativistic limit $v^2\ll 1$ for the mean fluid velocity and in the weak field regime $\tilde{\Psi}_{\rm N}\ll 1$. We made no approximation for the pressure and the equations of motion also apply to fluids with a pressure of the same order as the density, such as $\tilde{p}=w\tilde{\rho}$ where w is a parameter of order unity. However, in the usual CDM context, the pressure is negligible on cosmological scales and it is built on small scales by nonlinear processes, such as the collapse of gas clouds that generate shocks or the virialization of dark matter halos (which generate an effective pressure through the velocity dispersion of the particles). Then, the pressure is of the order $\tilde{p}\sim\tilde{\rho}c_s^2$, where c_s is the speed of sound or the velocity dispersion, and $c_s^2\sim\tilde{\Psi}_{\rm N}$ because it is generated by the gravitational collapse (for instance, if we have hydrostatic equilibrium we typically have $\nabla\tilde{\Psi}_{\rm N}\sim\nabla\tilde{p}/\tilde{\rho}$ as the pressure balances gravity).

Then, in the regime $\tilde{p}/\tilde{\rho}\sim\tilde{\Psi}_{\rm N}\sim v^2\ll 1$, the background pressure is zero, $\bar{\tilde{p}}=0$, and we recover the cosmological dynamics studied in [7] for a pressureless fluid. Thus, the Friedmann equations read as Eqs.(14)-(15) and the matter and radiation densities evolve as in Eq.(16). The Klein-Gordon equation becomes as in Eq.(19).

For the perturbations, the continuity and Euler equations (A25) and (A24) simplify as

$$\frac{\partial\tilde{\rho}}{\partial\tau}+\nabla\cdot(\tilde{\rho}\mathbf{v})+3\tilde{\mathcal{H}}\tilde{\rho}=\tilde{\rho}\frac{\partial\ln A}{\partial\tau}, \tag{A32}$$

and

$$\frac{\partial\mathbf{v}}{\partial\tau}+(\mathbf{v}\cdot\nabla)\mathbf{v}+\left(\tilde{\mathcal{H}}+\frac{\partial\ln A}{\partial\tau}\right)\mathbf{v}=-\nabla(\tilde{\Psi}_{\rm N}+\ln A)-\frac{\nabla\tilde{p}}{\tilde{\rho}}, \tag{A33}$$

while the Poisson equation remains identical to Eq.(A27) and the Klein-Gordon equation (A26) becomes

$$\frac{1}{\tilde{a}^3}\frac{\partial}{\partial\tilde{t}}\left(\tilde{a}^3\frac{\partial\varphi}{\partial\tilde{t}}\,K'\right)-\frac{1}{\tilde{a}^2}\nabla\cdot(\nabla\varphi\,K')=-\tilde{\rho}\frac{{\rm d}\ln A}{{\rm d}\varphi}. \tag{A34}$$

Therefore, in this regime the only effect of the pressure is to add the usual pressure term in the Euler equation, without mixed terms involving the coupling function $A(\varphi)$.

5. Sub-horizon regime

To simplify the Einstein equations (A28) we already used the small-scale limit, $k/\tilde{a}\tilde{H}\gg 1$, which corresponds to scales that are much below the Hubble scale $\tilde{r}_{\rm H}=1/\tilde{H}$. This is the regime that is relevant for the formation of cosmological large-scale structures, such as clusters of galaxies. Then, the continuity and Euler equations (A32)-(A33) and the Poisson equation (A27) can be further simplified. Indeed, as in Eq.(A29), we obtain the estimates

$$k/\tilde{a}\tilde{H}\gg 1\ :\ \frac{\delta\varphi}{\tilde{M}_{\rm Pl}}\sim\frac{\beta}{K'}\frac{\tilde{a}^2\tilde{H}^2}{k^2}\frac{\delta\tilde{\rho}}{\bar{\tilde{\rho}}}\ll\frac{\delta\tilde{\rho}}{\bar{\tilde{\rho}}}, \tag{A35}$$

$$\delta A\sim\frac{\beta\delta\varphi}{\tilde{M}_{\rm Pl}}\sim\frac{\beta^2}{K'}\frac{\tilde{a}^2\tilde{H}^2}{k^2}\frac{\delta\tilde{\rho}}{\bar{\tilde{\rho}}}\ll\frac{\delta\tilde{\rho}}{\bar{\tilde{\rho}}}, \tag{A36}$$

$$\delta\tilde{\chi}\simeq-\frac{(\nabla\delta\varphi)^2}{2\mathcal{M}^4\tilde{a}^2}\sim\frac{\beta^2}{K'^2}\frac{\tilde{a}^2\tilde{H}^2}{k^2}\frac{(\delta\tilde{\rho})^2}{\bar{\tilde{\rho}}^2}\ll\frac{(\delta\tilde{\rho})^2}{\bar{\tilde{\rho}}^2}, \tag{A37}$$

$$\frac{\delta\tilde{\rho}_\varphi}{\delta\tilde{\rho}}\sim\frac{\beta^2}{K'}\frac{\tilde{a}^2\tilde{H}^2}{k^2}\left(1+\frac{\delta\tilde{\rho}}{\bar{\tilde{\rho}}}\right)\ll 1. \tag{A38}$$

Then, in the continuity and Euler equations (A32)-(A33), we can write $\partial\ln A/\partial\tau\simeq{\rm d}\ln\bar{A}/{\rm d}\tau$, which leads to Eqs.(20) and (21). In the Poisson equation (A27), we can neglect $\delta\tilde{\rho}_\varphi$, which gives Eq.(22). In the Klein-Gordon equation (A34), we can neglect the fluctuations of A and only keep the spatial gradients. This leads to Eq.(23), which also corresponds to the quasi-static approximation.

6. Formation of large-scale structures

Introducing the Einstein-frame matter density contrast,

$$\tilde{\delta}=\delta\tilde{\rho}/\bar{\tilde{\rho}}, \tag{A39}$$

the continuity equation (20) also writes as

$$\frac{\partial\tilde{\delta}}{\partial\tau}+\nabla\cdot[(1+\tilde{\delta})\mathbf{v}]=0. \tag{A40}$$

Thus, in terms of the density contrast we recover the usual continuity equation, without any A-term left. This is related to the fact that $\tilde{\delta} = \hat{\delta}$, where $\hat{\delta} = \delta\hat{\rho}/\bar{\hat{\rho}}$ is the conserved matter density introduced in Eq.(A13), within our set of approximations ($\tilde{p} \ll \tilde{\rho}$ and $A \simeq \bar{A}$, so that the factor $\bar{A}$ cancels out in the ratio $\delta\hat{\rho}/\bar{\hat{\rho}}$).

On perturbative scales, we set the pressure term to zero, as in standard perturbation theory, because it is generated by non-perturbative effects such as shell crossing and virialization (shocks). Then, the formation of large-scale structures can be tackled through a perturbative approach, as in the usual Λ-CDM case. Introducing the two-component vector $\tilde{\psi}$,

$$\tilde{\psi} \equiv \begin{pmatrix} \tilde{\psi}_1 \\ \tilde{\psi}_2 \end{pmatrix} \equiv \begin{pmatrix} \tilde{\delta} \\ -(\nabla\cdot\mathbf{v})/(\mathrm{d}\tilde{a}/\mathrm{d}\tilde{t}) \end{pmatrix}, \qquad \text{(A41)}$$

equations (A40) and (21) read in Fourier space as

$$\frac{\partial\tilde{\psi}_1}{\partial\ln\tilde{a}} - \tilde{\psi}_2 = \int \mathrm{d}\mathbf{k}_1\mathrm{d}\mathbf{k}_2\ \delta_D(\mathbf{k}_1+\mathbf{k}_2-\mathbf{k})\hat{\alpha}(\mathbf{k}_1,\mathbf{k}_2) \times \tilde{\psi}_2(\mathbf{k}_1)\tilde{\psi}_1(\mathbf{k}_2), \qquad \text{(A42)}$$

$$\frac{\partial\tilde{\psi}_2}{\partial\ln\tilde{a}} - \frac{3}{2}\tilde{\Omega}_\mathrm{m}(1+\tilde{\epsilon}_1)\tilde{\psi}_1 + \left(2+\frac{1}{\tilde{H}^2}\frac{\mathrm{d}\tilde{H}}{\mathrm{d}\tilde{t}}+\tilde{\epsilon}_2\right)\tilde{\psi}_2 = \int \mathrm{d}\mathbf{k}_1\mathrm{d}\mathbf{k}_2\ \delta_D(\mathbf{k}_1+\mathbf{k}_2-\mathbf{k})\hat{\beta}(\mathbf{k}_1,\mathbf{k}_2)\tilde{\psi}_2(\mathbf{k}_1)\tilde{\psi}_2(\mathbf{k}_2), \qquad \text{(A43)}$$

with

$$\hat{\alpha}(\mathbf{k}_1,\mathbf{k}_2) = \frac{(\mathbf{k}_1+\mathbf{k}_2)\cdot\mathbf{k}_1}{k_1^2}, \hat{\beta}(\mathbf{k}_1,\mathbf{k}_2) = \frac{|\mathbf{k}_1+\mathbf{k}_2|^2(\mathbf{k}_1\cdot\mathbf{k}_2)}{2k_1^2k_2^2}. \qquad \text{(A44)}$$

The two differences from the equations of motion obtained in the Λ-CDM cosmology are the two time-dependent factors $\tilde{\epsilon}_i(t)$, defined by

$$\tilde{\epsilon}_1(\tilde{t}) \equiv \frac{2\beta^2}{\bar{K}'}, \quad \tilde{\epsilon}_2(\tilde{t}) \equiv \frac{\mathrm{d}\ln\bar{A}}{\mathrm{d}\ln\tilde{a}} = \frac{\beta}{\tilde{M}_\mathrm{Pl}}\frac{\mathrm{d}\bar{\varphi}}{\mathrm{d}\ln\tilde{a}}. \qquad \text{(A45)}$$

In Eq.(A43) the factor $\tilde{\Omega}_\mathrm{m}(1+\tilde{\epsilon}_1)$ can also be written as $\hat{\Omega}_\mathrm{m}(1+\hat{\epsilon}_1)$, where $\hat{\Omega}_\mathrm{m}$ is the cosmological parameter associated with the conserved density $\hat{\rho}$ defined in Eq.(A13), [$\hat{\Omega}_\mathrm{m} = \bar{\hat{\rho}}/\tilde{\rho}_\mathrm{crit} = \tilde{\Omega}_\mathrm{m}/\bar{A}$, with $\tilde{\rho}_\mathrm{crit} = 3\tilde{M}_\mathrm{Pl}^2\tilde{H}^2$ the Einstein-frame critical density], and $\hat{\epsilon}_1 = \bar{A}(1+\tilde{\epsilon}_1) - 1 = \bar{A} - 1 + 2\bar{A}\beta^2/\bar{K}'$.

On large scales or at early times, we can linearize the equations of motion (A42)-(A43). This gives for the linear growing and decaying modes $\tilde{D}_\pm(\tilde{t})$ the evolution equation

$$\frac{\mathrm{d}^2\tilde{D}}{\mathrm{d}(\ln\tilde{a})^2} + \left(2+\frac{1}{\tilde{H}^2}\frac{\mathrm{d}\tilde{H}}{\mathrm{d}\tilde{t}}+\tilde{\epsilon}_2\right)\frac{\mathrm{d}\tilde{D}}{\mathrm{d}\ln\tilde{a}} - \frac{3}{2}\tilde{\Omega}_\mathrm{m}(1+\tilde{\epsilon}_1)\tilde{D} = 0. \qquad \text{(A46)}$$

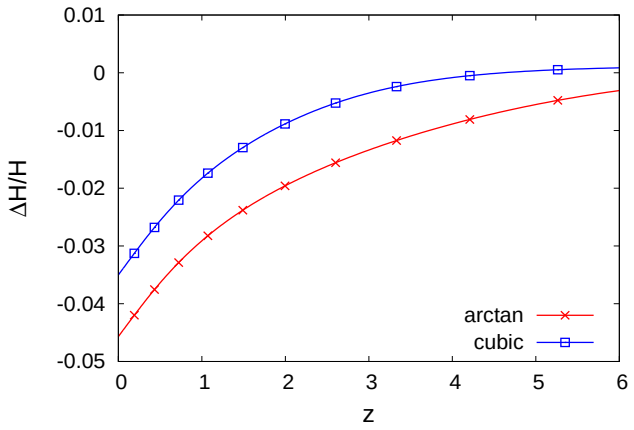

FIG. 20: Relative deviation, $\tilde{H}/H - 1$, of the Einstein-frame Hubble rate from the Jordan-frame Hubble rate, as a function of the Jordan-frame redshift.

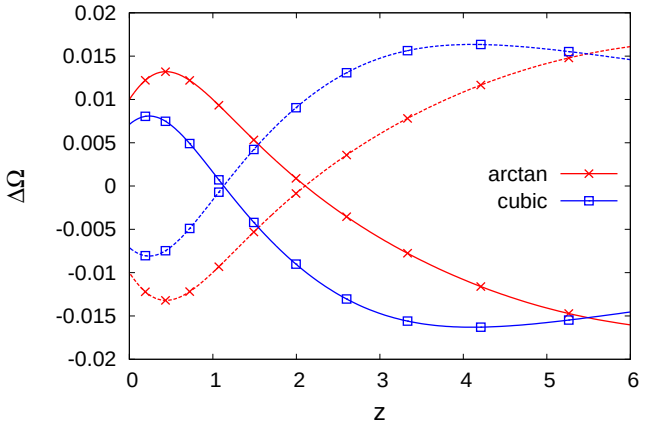

FIG. 21: Deviation of the Einstein-frame cosmological parameters from their Jordan-frame counterparts, $\hat{\Omega} - \Omega$, as a function of the Jordan-frame redshift. We show the matter density parameters (solid lines) and the dark-energy density parameters (dashed lines). In the Einstein frame we consider the effective matter and dark-energy densities as given by Eqs.(B2) and (B3).

Appendix B: Comparison of Einstein-frame and Jordan-frame backgrounds

In this appendix we compare the Einstein-frame background quantities with their Jordan-frame counterparts. We show in Fig. 20 the relative deviation of the Einstein-frame Hubble rate from the Jordan-frame Hubble rate. From Eq.(24) this is given by

$$\frac{\tilde{H}-H}{H} = \bar{A}(1-\epsilon_2) - 1. \qquad \text{(B1)}$$

We can see that at low redshift the Einstein-frame Hubble rate is typically lower than its Jordan-frame counterpart,

at a fixed Jordan-frame redshift. The comparison with Fig. 2 shows that at $z \lesssim 4$ the deviation between these two expansion rates is greater than the deviation between the Jordan-frame expansion and its Λ-CDM reference. As expected, this deviation is again of the order of a few percent, set by the value of β^2. This clearly shows that for the K-mouflage scenario one cannot treat both frames as approximately identical, contrary to what happens in many modified-gravity theories such as $f(R)$ models or dilaton models. At high z the relative difference between both Hubble rates vanishes, as can be seen from Eq.(24) as $\bar{A} \to 1$ and $\epsilon_2 \to 0$.

We show in Fig. 21 the deviation between the Einstein-frame and Jordan-frame density cosmological parameters. More precisely, for the Einstein frame we consider the cosmological "conserved" matter density $\hat{\rho}$ introduced in Eq.(A13). Using Eq.(37) this is given by

$$\hat{\Omega}_{\rm m} = \frac{\tilde{\Omega}_{\rm m}}{\bar{A}} = \frac{\Omega_{\rm m}}{\bar{A}(1-\epsilon_2)^2}. \tag{B2}$$

On the other hand, the radiation density parameter in the Einstein frame is $\tilde{\Omega}_{(r)} = \Omega_{(r)}/(1-\epsilon_2)^2$, from Eq.(37), and the Einstein-frame dark-energy density is then

$$\hat{\Omega}_{\rm de} \equiv 1 - \hat{\Omega}_{\rm m} - \tilde{\Omega}_{(r)} = \frac{\bar{A}-1}{\bar{A}}\tilde{\Omega}_{\rm m} + \tilde{\Omega}_{\varphi}. \tag{B3}$$

Again, we find in Fig. 21 that the differences between the Einstein-frame and Jordan-frame cosmological parameters are of the order of 1%.

Appendix C: Unitarity constraints

The K-mouflage models involve higher-order operators in the derivatives of φ and a coupling of the scalar field to matter β. This coupling induces a Yukawa interaction of the scalar field with fermions,

$$\mathcal{L}_I = \beta \frac{m_f}{M_{\rm Pl}} \bar{\psi}\psi\, \delta\varphi, \tag{C1}$$

where $\delta\varphi = \varphi - \bar{\varphi}$ are the fluctuations around a background $\bar{\varphi}$. Interaction terms in the scalar Lagrangian of the type $\mathcal{M}^4\tilde{\chi}^n$ in a background field configuration $\bar{\tilde{\chi}}$ imply the existence of the two-body scattering processes $f\bar{f} \to \varphi\varphi$ at tree level, with the exchange of one scalar field φ. In quantum mechanics, unitarity of the scattering matrix requires that the scattering amplitude $\mathcal{M}_{f\bar{f}\to\varphi\varphi}$ for this process should satisfy $\mathcal{M}_{f\bar{f}\to\varphi\varphi} \leq 16\pi$. In the clusters that we consider in the main body of the paper, the background value of $\bar{\tilde{\chi}} \lesssim 10^{-3}$ is small, and the background value of $\bar{K}' \simeq 1$ implies that clusters are unscreened. We focus on processes that can happen inside the hot gas of the clusters and consider the two-body scattering processes involving either electrons or nuclei. For temperatures of the gas less than $T_g \lesssim 10$ keV, the particles are non-relativistic. We only consider K-mouflage functions $K(\tilde{\chi})$ whose small $\tilde{\chi}$ expansion starts at the cubic order. In this case, the three-point self-interaction of the scalar field is of order

$$\mathcal{L}_3 \sim \mathcal{M}^4\bar{\tilde{\chi}}\frac{(\partial_{\mathbf{r}}\bar{\varphi})(\partial_{\mathbf{r}}\delta\varphi)}{\mathcal{M}^4}\frac{(\partial\delta\varphi)^2}{\mathcal{M}^4}, \tag{C2}$$

where we consider a quasi-static background configuration. The energies of the two outgoing scalars are $E_{1,2} \sim m_f$ whereas the spatial 3-momentum of the particles is $p_r \sim \sqrt{m_f T_g}$. The scalar propagator gives a factor of $1/m_f^2$ in the non-relativistic limit and finally we get that the scattering amplitude can be estimated as

$$\mathcal{M}_{f\bar{f}\to\varphi\varphi} \sim \beta\frac{m_f^2}{M_{\rm Pl}\mathcal{M}^2}\bar{\tilde{\chi}}^{3/2}\sqrt{m_f T_g}. \tag{C3}$$

For protons and neutrons at temperatures $T_g \lesssim 10$ keV for $\beta = 0.1$ and using $\bar{\tilde{\chi}} \lesssim 10^{-3}$, we find that $\mathcal{M}_{f\bar{f}\to\varphi\varphi} \lesssim 10^{-2}$, implying that unitarity is respected in the two-body processes.

Terms of higher order in $\tilde{\chi}$ can lead to processes such as $f\bar{f} \to n\varphi$ involving n scalars in the final state. The scattering cross section grows fast with the number of outgoing particles and can exceed the Froissart bound on the $\sigma_{\rm total} \lesssim \frac{1}{m_f^2}$. This violation is relaxed by classicalization [94, 95] in the same fashion as in Galileon models [18], where a classical lump sourced by the incoming energy of the two fermions in the center-of-mass frame is created. For K-mouflage models, this classical configuration has a typical size given by the K-mouflage radius R_K [11] and the scattering cross section becomes equal to the geometrical cross section proportional to R_K^2. This process is analogous to the creation of black holes in high-energy collisions.

K-mouflage models also satisfy a non-renormalization theorem analogous to the one for Galileons [96]. The quantum corrections going beyond the K-mouflage Lagrangian are negligible when $r \gtrsim \mathcal{M}_K^{-1}$, where $\mathcal{M}_K = \bar{K}'^{1/4}\mathcal{M}$. Inside galaxy clusters, this is a short scale around 1 mm and we can completely neglect quantum corrections on cluster scales.

[1] E. Babichev, C. Deffayet, and R. Ziour, Int.J.Mod.Phys. **D18**, 2147 (2009), 0905.2943.

[2] P. Brax, C. Burrage, and A.-C. Davis, JCAP **1301**, 020 (2013), 1209.1293.

[3] J. Khoury and A. Weltman, Phys.Rev.Lett. **93**, 171104 (2004), astro-ph/0309300.

[4] J. Khoury and A. Weltman, Phys. Rev. **D69**, 044026 (2004), astro-ph/0309411.
[5] T. Damour and A. M. Polyakov, Nucl. Phys. **B423**, 532 (1994), hep-th/9401069.
[6] A. Vainshtein, Phys.Lett. **B39**, 393 (1972).
[7] P. Brax and P. Valageas, Phys. Rev. D **90**, 023507 (2014), 1403.5420.
[8] P. Brax and P. Valageas, Phys. Rev. D **90**, 023508 (2014), 1403.5424.
[9] A. Barreira, P. Brax, S. Clesse, B. Li, and P. Valageas, ArXiv e-prints (2014), 1411.5965.
[10] I. Sawicki, I. D. Saltas, L. Amendola, and M. Kunz, JCAP **1**, 004 (2013), 1208.4855.
[11] P. Brax and P. Valageas, Phys. Rev. D **90**, 123521 (2014), 1408.0969.
[12] A. Barreira, P. Brax, S. Clesse, B. Li, and P. Valageas, ArXiv e-prints (2015), 1504.01493.
[13] R. A. Sunyaev and Y. B. Zeldovich, Comments on Astrophysics and Space Physics **4**, 173 (1972).
[14] R. R. Caldwell, R. Dave, and P. J. Steinhardt, Physical Review Letters **80**, 1582 (1998), astro-ph/9708069.
[15] P. J. Steinhardt, L. Wang, and I. Zlatev, Phys. Rev. D **59**, 123504 (1999), astro-ph/9812313.
[16] G. Esposito-Farèse and D. Polarski, Phys. Rev. D **63**, 063504 (2001), gr-qc/0009034.
[17] P. Brax and C. Burrage, Phys. Rev. D **90**, 104009 (2014), 1407.1861.
[18] P. Brax and C. Burrage, Phys. Rev. D **91**, 043515 (2015), 1407.2376.
[19] D. J. Eisenstein, W. Hu, and M. Tegmark, *Astrophys. J. Letter* **504**, L57+ (1998), arXiv:astro-ph/9805239.
[20] D. J. Eisenstein, I. Zehavi, D. W. Hogg, R. Scoccimarro, M. R. Blanton, R. C. Nichol, R. Scranton, H.-J. Seo, M. Tegmark, Z. Zheng, et al., Astrophys. J. **633**, 560 (2005), arXiv:astro-ph/0501171.
[21] A. C. and B. Paczynski, Nature **281**, 358 (1979).
[22] P. Valageas, *Astr. & Astrophys.* **508**, 93 (2009), 0905.2277.
[23] P. Valageas, Phys. Rev. D **89**, 123522 (2014).
[24] T. Nishimichi and P. Valageas, Phys. Rev. D **90**, 023546 (2014).
[25] A. Kehagias, H. Perrier, and A. Riotto, Modern Physics Letters A **29**, 1450152 (2014).
[26] J. F. Navarro, C. S. Frenk, and S. D. M. White, Astrophys. J. **462**, 563 (1996), astro-ph/9508025.
[27] P. Valageas, T. Nishimichi, and A. Taruya, ArXiv e-prints (2013), 1302.4533.
[28] P. Valageas, Phys. Rev. D **88**, 083524 (2013).
[29] N. Kaiser, Mont. Not. Roy. Astron. Soc. **222**, 323 (1986).
[30] J. Merten, M. Meneghetti, M. Postman, K. Umetsu, A. Zitrin, E. Medezinski, M. Nonino, A. Koekemoer, P. Melchior, D. Gruen, et al., ArXiv e-prints (2014), 1404.1376.
[31] J. F. Navarro, C. S. Frenk, and S. D. M. White, Astrophys. J. **490**, 493 (1997), arXiv:astro-ph/9611107.
[32] H. Mo, F. C. van den Bosch, and S. White, *Galaxy Formation and Evolution* (Cambridge University Press, 2010).
[33] J. Binney and S. Tremaine, *Galactic dynamics* (Princeton University Press, Princeton, NJ, USA, 1987).
[34] A. Cavaliere and R. Fusco-Femiano, *Astr. & Astrophys.* **49**, 137 (1976).
[35] M. Plionis, Lect. Notes Phys. **740** (2008).
[36] A. Vikhlinin, R. A. Burenin, H. Ebeling, W. R. Forman, A. Hornstrup, C. Jones, A. V. Kravtsov, S. S. Murray, D. Nagai, H. Quintana, et al., Astrophys. J. **692**, 1033 (2009), 0805.2207.
[37] Y.-Y. Zhang, A. Finoguenov, H. Böhringer, J.-P. Kneib, G. P. Smith, R. Kneissl, N. Okabe, H. Dahle, and T. H. Reiprich, in *The X-ray Universe 2008* (2008), p. 222.
[38] A. Mantz, S. W. Allen, H. Ebeling, D. Rapetti, and A. Drlica-Wagner, *Mon. Not. R. Astr. Soc.* **406**, 1773 (2010), 0909.3099.
[39] G. W. Pratt, J. H. Croston, M. Arnaud, and H. Böhringer, *Astr. & Astrophys.* **498**, 361 (2009), 0809.3784.
[40] Y. Ikebe, T. H. Reiprich, H. Böhringer, Y. Tanaka, and T. Kitayama, *Astr. & Astrophys.* **383**, 773 (2002), astro-ph/0112315.
[41] A. N. Bender, J. Kennedy, P. A. R. Ade, K. Basu, F. Bertoldi, S. Burkutean, J. Clarke, D. Dahlin, M. Dobbs, D. Ferrusca, et al., ArXiv e-prints (2014), 1404.7103.
[42] S. Cole and N. Kaiser, *Mon. Not. R. Astr. Soc.* **237**, 1127 (1989).
[43] H. J. Mo and S. D. M. White, *Mon. Not. R. Astr. Soc.* **282**, 347 (1996), arXiv:astro-ph/9512127.
[44] R. K. Sheth, H. J. Mo, and G. Tormen, *Mon. Not. R. Astr. Soc.* **323**, 1 (2001), arXiv:astro-ph/9907024.
[45] J. L. Tinker, B. E. Robertson, A. V. Kravtsov, A. Klypin, M. S. Warren, G. Yepes, and S. Gottlöber, Astrophys. J. **724**, 878 (2010), 1001.3162.
[46] P. Brax, A.-C. Davis, B. Li, and H. A. Winther, Phys. Rev. D **86**, 044015 (2012), 1203.4812.
[47] J. Khoury (2013), 1312.2006.
[48] P. Brax, Class.Quant.Grav. **30**, 214005 (2013).
[49] W. Hu and I. Sawicki, Phys. Rev. D **76**, 064004 (2007), 0705.1158.
[50] P. Brax, C. van de Bruck, A.-C. Davis, and D. J. Shaw, Phys.Rev. **D78**, 104021 (2008), 0806.3415.
[51] T. P. Sotiriou and V. Faraoni, Rev.Mod.Phys. **82**, 451 (2010), 0805.1726.
[52] A. de Felice and S. Tsujikawa, Living Re. Relativ. **13**, 3 (2010).
[53] R. Gannouji, M. Sami, and I. Thongkool (2012), 1206.3395.
[54] T. Chiba, Physics Letters B **575**, 1 (2003).
[55] M. Gasperini, F. Piazza, and G. Veneziano, Phys.Rev. **D65**, 023508 (2002), gr-qc/0108016.
[56] P. Brax, C. van de Bruck, A.-C. Davis, and D. Shaw, Phys. Rev. **D82**, 063519 (2010), 1005.3735.
[57] P. Brax, C. van de Bruck, A.-C. Davis, B. Li, and D. J. Shaw, Phys.Rev. **D83**, 104026 (2011), 1102.3692.
[58] K. Hinterbichler and J. Khoury, Phys. Rev. Lett. **104**, 231301 (2010), 1001.4525.
[59] P. Brax, A.-C. Davis, B. Li, H. A. Winther, and G.-B. Zhao, JCAP **10**, 002 (2012), 1206.3568.
[60] A. Nicolis, R. Rattazzi, and E. Trincherini, Phys.Rev. **D79**, 064036 (2009), 0811.2197.
[61] C. Deffayet, G. Esposito-Farèse, and V. A., Phys. Rev. D **79**, 084003 (2009).
[62] C. Deffayet, D. S., and G. Esposito-Farèse, Phys. Rev. D **80**, 064015 (2009).
[63] A. De Felice and S. Tsujikawa, Phys. Rev. Lett. **105**, 111301 (2010).
[64] A. De Felice and S. Tsujikawa, JCAP **3**, 025 (2012), 1112.1774.
[65] A. Barreira, B. Li, W. A. Hellwing, L. Lombriser, C. M.

Baugh, and S. Pascoli, JCAP **4**, 029 (2014), 1401.1497.
[66] P. Brax and P. Valageas, Phys. Rev. D **88**, 023527 (2013), 1305.5647.
[67] A. Terukina and K. Yamamoto, Phys. Rev. D **86**, 103503 (2012), 1203.6163.
[68] C. Arnold, E. Puchwein, and V. Springel, *Mon. Not. R. Astr. Soc.* **440**, 833 (2014), 1311.5560.
[69] A. Terukina, L. Lombriser, K. Yamamoto, D. Bacon, K. Koyama, and R. C. Nichol, JCAP **4**, 013 (2014), 1312.5083.
[70] H. Wilcox, D. Bacon, R. C. Nichol, P. J. Rooney, A. Terukina, A. K. Romer, K. Koyama, G.-B. Zhao, R. Hood, R. G. Mann, et al., ArXiv e-prints (2015), 1504.03937.
[71] L. Lombriser, F. Schmidt, T. Baldauf, R. Mandelbaum, U. Seljak, and R. E. Smith, Phys. Rev. D **85**, 102001 (2012), 1111.2020.
[72] J. Clampitt, B. Jain, and J. Khoury, JCAP **1**, 030 (2012), 1110.2177.
[73] F. Schmidt, M. Lima, H. Oyaizu, and W. Hu, Phys. Rev. D **79**, 083518 (2009), 0812.0545.
[74] C. C. Moran, R. Teyssier, and B. Li, *Mon. Not. R. Astr. Soc.* **448**, 307 (2015).
[75] M. Gronke, C. Llinares, D. F. Mota, and H. A. Winther, *Mon. Not. R. Astr. Soc.* **449**, 2837 (2015), 1412.0066.
[76] A. Hammami, C. Llinares, D. F. Mota, and H. A. Winther, *Mon. Not. R. Astr. Soc.* **449**, 3635 (2015), 1503.02004.
[77] L. Lombriser, K. Koyama, G.-B. Zhao, and B. Li, Phys. Rev. D **85**, 124054 (2012), 1203.5125.
[78] S. Tsujikawa and T. Tatekawa, Physics Letters B **665**, 325 (2008), 0804.4343.
[79] T. Y. Lam, F. Schmidt, T. Nishimichi, and M. Takada, Phys. Rev. D **88**, 023012 (2013), 1305.5548.
[80] Y. Zu, D. H. Weinberg, E. Jennings, B. Li, and M. Wyman, *Mon. Not. R. Astr. Soc.* **445**, 1885 (2014), 1310.6768.
[81] G.-B. Zhao, B. Li, and K. Koyama, Phys.Rev. **D83**, 044007 (2011), 1011.1257.
[82] S. Ferraro, F. Schmidt, and W. Hu, Phys. Rev. D **83**, 063503 (2011), 1011.0992.
[83] B. Li, G.-B. Zhao, and K. Koyama, *Mon. Not. R. Astr. Soc.* **421**, 3481 (2012), 1111.2602.
[84] L. Lombriser, B. Li, K. Koyama, and G.-B. Zhao, Phys. Rev. D **87**, 123511 (2013), 1304.6395.
[85] F. Schmidt, A. Vikhlinin, and W. Hu, Phys. Rev. D **80**, 083505 (2009).
[86] M. Cataneo, D. Rapetti, F. Schmidt, A. B. Mantz, S. W. Allen, D. E. Applegate, P. L. Kelly, A. von der Linden, and R. G. Morris, ArXiv e-prints (2014), 1412.0133.
[87] L. Boubekeur, E. Giusarma, O. Mena, and H. Ramírez, Phys. Rev. D **90**, 103512 (2014), 1407.6837.
[88] D. S. Y. Mak, E. Pierpaoli, F. Schmidt, and N. Macellari, Phys. Rev. D **85**, 123513 (2012), 1111.1004.
[89] H. Okada, T. Totani, and S. Tsujikawa, Phys. Rev. D **87**, 103002 (2013), 1208.4681.
[90] J. Bel, P. Brax, C. Marinoni, and P. Valageas, ArXiv e-prints (2014), 1406.3347.
[91] B. Jain and J. VanderPlas, JCAP **1110**, 032 (2011), 1106.0065.
[92] V. Vikram, J. Sakstein, C. Davis, and A. Neil, ArXiv e-prints (2014), 1407.6044.
[93] C. Arnold, E. Puchwein, and V. Springel, *Mon. Not. R. Astr. Soc.* **448**, 2275 (2015), 1411.2600.
[94] G. Dvali, G. F. Giudice, C. Gomez, and A. Kehagias, JHEP **08**, 108 (2011), 1010.1415.
[95] L. Keltner and A. J. Tolley (2015), 1502.05706.
[96] C. de Rham, Comptes Rendus Physique **13**, 666 (2012), 1204.5492.